QUADRATIC SPATIAL SOLITON INTERACTIONS

by

LADISLAV JANKOVIC
B.S. University of Zagreb, 1997
M.S. University of Central Florida, 2002

A dissertation submitted in partial fulfillment of the requirements
for the degree of Doctor of Philosophy
in the School of Optics
at the University of Central Florida
Orlando, Florida

Summer Term
2004

Major Professor: Dr. George I. Stegeman

ABSTRACT

Quadratic spatial soliton interactions were investigated in this Dissertation. The first part deals with characterizing the principal features of multi-soliton generation and soliton self-reflection. The second deals with two beam processes leading to soliton interactions and collisions. These subjects were investigated both theoretically and experimentally.

The experiments were performed by using potassium niobate ($KNBO_3$) and periodically poled potassium titanyl phosphate (KTP) crystals. These particular crystals were desirable for these experiments because of their large nonlinear coefficients and, more importantly, because the experiments could be performed under non-critical-phase-matching (NCPM) conditions. The single soliton generation measurements, performed on $KNBO_3$ by launching the fundamental component only, showed a broad angular acceptance bandwidth which was important for the soliton collisions performed later. Furthermore, at high input intensities multi-soliton generation was observed for the first time. The influence on the multi-soliton patterns generated of the input intensity and beam symmetry was investigated. The combined experimental and theoretical efforts indicated that spatial and temporal noise on the input laser beam induced multi-soliton patterns.

Another research direction pursued was intensity dependent soliton routing by using of a

specially engineered quadratically nonlinear interface within a periodically poled KTP sample. This was the first time demonstration of the self-reflection phenomenon in a system with a quadratic nonlinearity. The feature investigated is believed to have a great potential for soliton routing and manipulation by engineered structures.

A detailed investigation was conducted on two soliton interaction and collision processes. Birth of an additional soliton resulting from a two soliton collision was observed and characterized for the special case of a non-planar geometry. A small amount of spiraling, up to 30 degrees rotation, was measured in the experiments performed. The parameters relevant for characterizing soliton collision processes were also studied in detail. Measurements were performed for various collision angles (from 0.2 to 4 degrees), phase mismatch, relative phase between the solitons and the distance to the collision point within the sample (which affects soliton formation). Both the individual and combined effects of these collision variables were investigated.

Based on the research conducted, several all-optical switching scenarios were proposed.

To my parents

ACKNOWLEDGMENTS

In the first place I would like to thank my family and particularly my parents for the unconditional support they have given me in making of my decisions and for giving me freedom to build my way of thinking and understanding of the world.

In my work here at CREOL I consider myself very fortunate to work under supervision of Professor George Stegeman. Thanks to him, I learned not only how to manage difficulties of a scientific work but also how to accomplish great and challenging research tasks through collaborations with other scientists. Working under George's supervision I was provided with an exceptional opportunity to gain a first hand knowledge on ultrafast nonlinear phenomena. It was a precious experience to discuss research matters with Professor Demetrios Christodoulides, who strongly influenced my research directions and my understanding of the physics beyond it. Also I was very fortunate with my overseas collaborators Professor Lluis Torner, Dr. Mordechai Katz and Dr. Silvia Carrasco, who very positively influenced my scientific development and my research progress and I would like to thank them for this. A great deal of basic experimental and research skills I learned from Dr. Roman Malendevich, Dr. HongKi Kim and Dr. Sergey Polyakov, whom I would like to thank as well. My sincere thanks also go to Pierre Aboussouan and Marco Affolter, visiting students to Dr. Stegeman's group, who proved to be very

enthusiastic and skilled researchers and fast learners. I really appreciated working with my CREOL colleagues Arek, Sergei, Robert, Joachim, Clara, Bobi, George and Mahesh. I would like to thank to all School of Optics/CREOL & FPCE faculty, students and stuff for the friendly and inspiring environment.

Special thanks to my devoted friends Fang, Mirna, Bojan, Luis, Courtney, Marin and Natasa who were always here to give me a hand and advice.

TABLE OF CONTENTS

LIST OF FIGURES

LIST OF TABLES

CHAPTER ONE: INTRODUCTION

1.1   Motivation

Even though the work covered here is of fundamental research character the strong bonds with applications, or better to say potential applications, were in the background of the work. Optical solitons (Kerr [1, 2, 3, 4, 5], saturable Kerr [6, 7], photorefractive [8, 9, 10] and quadratic nonlinear systems [11, 12]) an interesting and intriguing consequence of nonlinear material properties, recently have attracted quite a lot of attention. Of great interest for the research field and the corresponding technology are Kerr and quadratic nonlinear systems. Ultrafast, "instant" material response makes these nonlinear systems unbeatable from the point of speed of "operation". Within this "ultrafast" concept a special place belongs to the spatial solitons. Having particle-like behavior in the interactions and collisions, optical solitons offer great potential for performing ultrafast all-optical switching or even computations [13].

Among all of effects that optical solitons offer, soliton collisions are considered to be very promising as basic blocks for performing switching and/or computing operations. The concept is illustrated in Figure 1.1. The basic process, a single collision event, as shown in

1

Figure 1.1a, relies on the fact that solitons change flavor (amount of red versus blue component, as shown on the schematic) in collisions. The solitons coming from the first stage of the interaction can be used in the next stage of the interactions as well. Eventually one could form a parallel sequential computational tool based on soliton collisions, as illustrated in Figure 1.1b. A number of solitons launched from the right side sequentially collide with the solitons coming from the left. Each previous stage of the interactions will influence the current one due to the changes in the solitons' flavor. Obviously everything relies on the properties of a single collision process. Therefore, this work naturally concentrated on investigating this most basic building block and most important step.
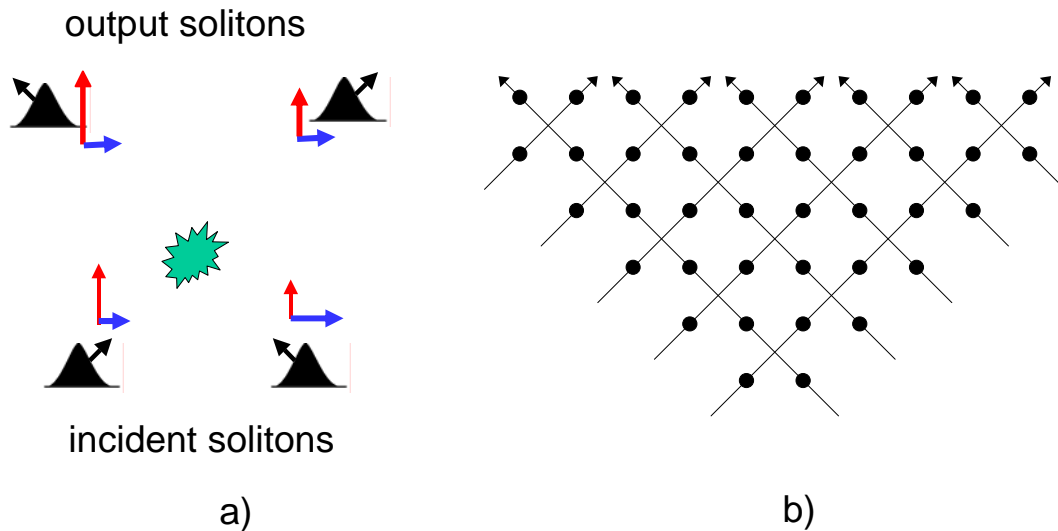
Figure 1.1: Ultrafast computing schematic is shown. a) The basic computational operation consists of a single soliton collision process. The collision outcome is recognized based on the changes in two soliton components (red and blue) b) Realization of multiple collisions used as parallel sequential computational tool

1.2   Why quadratic solitons?

Historically the science of optical solitons started soon after the experimental discovery of second harmonic generation (SHG), one of the first nonlinear processes in optics [14]. A theoretical explanation of the effect came soon afterward [15]. It was recognized in 1974 that processes leading to SHG can result in light self-confinement, leading to development of theoretical solutions named quadratic optical spatial solitons. However, almost at the same time as the development of the SHG story came the discovery of Kerr solitons (light self action in 1964 [16] and optical solitons in 1968 [17] and 1973 [18]) leading the nonlinear optics community into this direction. Kerr solitons require only one spectral component or beam. Moreover, the incident Gaussian beam input is relatively close to the sech(x) type of the soliton solution supported in Kerr systems. Therefore one would expect those types of solitons to be experimentally "easy" to generate. Availability of analytical expressions for Kerr solitons was another attractive aspect [17]. The final result was a relatively fast development of Kerr soliton science and postponement of quadratic solitons' development.

A very brief development of the optical soliton science (considering $\chi^{(2)}$ and $\chi^{(3)}$ nonlinearities only) is given in Figure 1.2. There is a large gap, indicated on the time chart as well, between the theoretical predictions and a series of the experimental observations of optical solitons even though the first observation was reported by Bjorkholm and Ashkin in the 1970s [19], however they did not call the observed features solitons.

3

1971 (Zakharov)
Kerr soliton
solution

1964 Chiao &
Talanov
Prediction of
Kerrr solitons

Kerr solitons

$$P^{NL} \propto \chi^{(3)} |E|^2 E$$
$$\Rightarrow n_{effective} = n + \tilde{n} I$$

$\Rightarrow$ self-guiding

Mid 1980s -1990s
different type of Kerr Solitons
vortex, gap solitons,
Manakov solitons, discrete solitons

1961 (Franken)
SHG experimental
observation

1962 (Armstrong)
theoretical
explanation

1967
Ostrovskii

1974, 1975
Karamizin &
Sukhorukov

Quadratic solitons theoretical
predictions

Quadratic solitons

$$P^{NL} \propto \chi^{(2)} EE$$

1995 Torruellas
1996 Schiek
experimental
observation of
quadratic spatial
solitons

2004

Figure 1.2: Simplified time line of $\chi^{(2)}$ (bottom) and $\chi^{(3)}$ (top) soliton research development.

Also one could ask why was it necessary to go into "tedious" quadratic soliton research, at least considering optical switching and computation, if we already had some of the effects demonstrated within Kerr solitons research. An important reason definitely lies in the order of nonlinearity. Using $\chi^{(2)}$ instead of $\chi^{(3)}$ immediately implies at least an order of magnitude decrease in power requirements. Also, even though quadratic solitons are more complex to generate than Kerr solitons, they also inherently offer two component configurations by having confined into a single soliton fundamental and second harmonic beams. However, dealing with quadratic solitons brings some complications like laser bandwidth and material and configuration requirements. Those will be discussed in more details later.

1.3 Scope of research

With the development of high power, ultrafast tunable laser systems, quadratic nonlinear crystals have become widely available for nonlinear optics experiments and spatial solitons have emerged as one of the most intriguing nonlinear effects. The research work discussed in this Dissertation concentrated on investigating quadratic spatial soliton generation and their interaction properties in bulk, (2+1)D systems. In order to later perform soliton interaction experiments a set of measurements on characterization of the soliton properties in the vicinity of NCPM was necessary. Multi-soliton generation occurred at high input intensities. This feature had not been previously reported in the quadratic soliton experiments in lithium niobate [12] and KTP [11] and the discovery stimulated extensive theoretical and experimental studies of the phenomena [20, 21, 22, 23]. This work is discussed in chapter 5.Another topic of the Dissertation research concentrated on soliton self-reflection which required a specially designed double-QPM PPKTP sample. The idea of intensity dependent beam routing, steering or simply reflecting dates back to the 1980s when intensity dependent reflection and transmission at an interface between two different Kerr media were experimentally investigated [24]. However in the experiments performed, the very small incident angles required dramatically limited the success of the experiment. On the other hand, the nonlinearity of a quadratic crystal can be modified in the sample fabrication process, finally resulting in a specially designed structure with modified nonlinear properties but completely unchanged linear properties. The idea of realizing soliton intensity dependent reflections in quadratic systems comes from the 1990s [25]. The first successful experimental realization of the phenomena is discussed in the Chapter 6 of this work.

Soliton collisions are one of the most intriguing topics in the spatial soliton field. Quadratic spatial soliton collisions were previously performed in only a very limited number of configurations, typically discussing only 0 and π relative phase [26, 27, 28]. Very detailed relative phase scans of soliton collision results are discussed here. The collision processes were investigated for various conditions (soliton formation, phase mismatch and collision angle). In addition, the birth of an additional soliton in a two soliton interaction process was observed in a non-planar quadratic soliton collision configuration for the first time. The only reported similar case was in 1997 for photorefractive solitons [29]. The feature, as discussed in this Dissertation, has potential to be used for all optical switching. These topics are covered in chapters 7 and 8.

In brief summary, this Dissertation is organized as follows.

Chapter 2 provides a brief overview of the basic concepts of quadratic nonlinear systems. Starting from the basic nonlinear polarization, the parametric equations, second harmonic generation under various conditions and finally the details of phase matching techniques are discussed. Most of the basic mathematical formalism needed for the later discussions is given in this chapter as well.

In Chapter 3 the laser system components are introduced and reviewed. The system consists of two units: a solid state laser and a tunable light conversion unit (OPG-OPA) pumped by the laser. The resulting tunable source OPG-OPA was used in the potassium niobate experiments and the Nd:YAG laser alone for the PPKTP experiments. The main features which facilitated the experiments, along with the drawbacks are discussed. Some of the evolving new system solutions, regarding the problems with the current laser, are introduced.

In Chapter 4 the theoretical basics of quadratic spatial solitons are given. In this chapter the spatial soliton concept is introduced and discussed along with the limiting Kerr soliton case. The main segments of the BPM numerical simulation tool are outlined.

Chapter 5 is dedicated to the single input beam nonlinear processes in potassium niobate. The material system is introduced and the details of the experimental setup, light source and measurements conditions are given. The single soliton generation properties and conditions are discussed. Once the input intensity is increased enough, multiple solitons are generated as reported in this chapter. The dependence of the multi-soliton generation on the input beam intensity and shape is investigated. The various multi-soliton patterns observed in the experiment are shown and interpreted theoretically. Based on the reported measurements the necessary conditions for the other experiments discussed in this Dissertation were established.

A periodically poled KTP sample, with a specially engineered quadratically nonlinear interface at the boundary between two quasi-phase-matched regions, was used to demonstrate intensity dependent reflections. The details of the experiments performed along with the results of the numerical simulations are given in Chapter 6. Some theoretical concepts on the self-reflection phenomenon are also introduced. The chapter also deals with the general PPKTP properties, concentrating on the properties of the sample used in the experiments. The properties and sample design are given.

Some general theoretical basics of quadratic soliton interactions and collisions are briefly introduced in Chapter 7. One whole section is dedicated to the experimental setup, discussing in detail the setup components. In fact the setup design was one of the most important factors in performing these soliton collision experiments. The work reported in this chapter was

concentrated on two configurations: nearly co-parallel solitons and solitons colliding at an angle of 0.9^0. The first configuration was sued to demonstrate fusion, repulsion and energy transfer processes. In the colliding section of the chapter the generation of an additional soliton upon collision is reported. Details on the additional soliton generation are given. Spiraling effects observed are reported in this chapter as well. The potential for applications of the observed effects is emphasized.

Chapter 8 describes various detailed aspects of the soliton collision experiments performed in PPKTP. Because of the finite sample sizes used in spatial soliton experiments, namely only a few diffraction lengths, it was not clear what the optimum conditions for studying interactions were. The outcome of a collision process can depend on the distance of the collision from the input facet, even if the other experimental conditions are kept the same. The effect is related to the distance required for a soliton to form when only the fundamental component is inputted. There is a minimum distance needed to generate the required harmonic. In addition, the effects of phase mismatch were investigated. The chapter also contains an investigation of the dependence of the output distribution from the soliton on the collision angle. The effects of these soliton collision variables were investigated for various input phase differences between the propagating beams.

In chapter 9 the main results of this thesis are summarized.

CHAPTER TWO: INTRODUCTION TO QUADRATIC NONLINEAR PHENOMENA

2.1   Nonlinear Polarization

One could say that in any optical system, no matter the complexity and number of the components involved, all possible outcomes can be predicted based on the Maxwell's equations. This could be considered to be canonically true if one is searching for new fundamental roles that have the potential to forever change the way we see the world. Even though optics "cannot offer" this kind of challenge it definitely has its own hidden surprises. In addition it has a great advantage in being able to visually show behavior that in the other scientific domains and fields remain buried deep in the physical systems themselves and can be seen only as a cause of some other "macroscopic" property.

Particularly interesting features in optics can be found in systems with nonlinear properties, as we will see in the following chapters. To introduce a basic nonlinear optics concept consider the nonlinear system polarization as a power series in electric field. Therefore the polarization can be written in the following way

$$\vec{P} = \ddot{\chi}^{(1)}\vec{E} + \ddot{\chi}^{(2)}\vec{E}\vec{E} + \ddot{\chi}^{(3)}\vec{E}\vec{E}\vec{E} + \cdots. \tag{2.1}$$

Here, $\vec{P}$ and $\vec{E}$ are polarization and electric field respectively. The terms associated with $\ddot{\chi}^{(1)}, \ddot{\chi}^{(2)}$ and $\ddot{\chi}^{(3)}$ are the linear, second and third order susceptibility tensors, respectively. $\vec{P}$ and $\vec{E}$ are treated here as vector quantities while the optical susceptibilities ($\ddot{\chi}^{(n)}$) are here considered in their most general form, as tensors. The second term (quadratic nonlinearity) in the equation is responsible for the most of the features discussed in this work. Because of the symmetry reasons associated with this term it can exist only in non-centrosymmetric mediums. On the other hand, the third term (third order nonlinearity) has no such limitations. However the influence of $\chi^{(3)}$ on an optical system is an order of magnitude weaker than the quadratic term effects. Typically whenever a quadratic term is nonzero the effects of the third order susceptibility can be neglected to first order. The polarization, as described by (2.1), can now be inserted into the wave equation

$$\nabla^2 \vec{E} - \frac{n^2}{c^2}\frac{\partial^2 \vec{E}}{\partial t^2} = \frac{4\pi}{c^2}\frac{\partial^2 \vec{P}}{\partial t^2}. \tag{2.2}$$

After neglecting the higher order terms we are left with only linear and quadratic terms. Second harmonic generation (SHG), sum (SFG) and difference frequency generation (DFG) result from the quadratic nonlinear term. Historically SHG was among the first discovered nonlinear effects [1]. A theoretical explanation of the phenomena came in 1962 [2].

2.2 SVEA and Second order processes

Before going into a more detail discussion of the previously mentioned quadratic nonlinear terms, the slow varying envelope approximation (SVEA) will be introduced, a very important approach in the treatment of the nonlinear phenomenon. For a more detailed description of SVEA see ref. [3]. SVEA is a central point of the theoretical quadratic soliton approach in this work. It is based on the assumption that the propagating electric field envelope changes slowly with propagation distance z. In a more mathematical form this assumption is given as

$$\left| \frac{\partial^2}{\partial z^2} E_0(z) \right| << \left| 2k \frac{\partial}{\partial z} E_0(z) \right|. \tag{2.3}$$

Here z is propagation direction, the electric field is defined as $E(x, y, z) = E_0(x, y, z) \exp(i(kz - \omega t))$ and k is the corresponding wavevector. The details on the beam dynamics along x and y directions is not consider here although for large z the solution should become z independent and localized in x and y. This gives us the final form for SVEA

$$e^{i(kz-\omega t)}\left(i2k \frac{\partial}{\partial z} + \frac{\partial^2}{\partial x^2} + \frac{\partial^2}{\partial y^2} \right) E_0(z) = \frac{\partial^2}{\partial t^2} P(z,t) \tag{2.4}$$

In principle most of the theoretical analyses in the quadratic soliton field are given within the scope of this equation. Of course once the applied electric field is strong enough to cause rapid changes in the electric field envelope with propagation through a nonlinear media, one has to use the full form Maxwell equations rather than SVEA. However, even in that case the SVEA approach is often a good starting point.

Consider more closely the processes contained within the interaction of an optical field ($\vec{E}$) with a quadratic media, defined with $\overset{\leftrightarrow}{\chi}^{(2)}$. A two frequency component electric field in its simplest form can be written as

$$\vec{E}(t) = \vec{E}_1 \exp(-i\omega_1 t) + \vec{E}_2 \exp(-i\omega_2 t) + c.c. \tag{2.5}$$

The resulting quadratic nonlinear polarization has several terms

$$
\begin{aligned}
P^{(2)}(t) &= \varepsilon_0 \chi^{(2)} E(t)^2 \\
&= \varepsilon_0 \chi^{(2)} \big[E_1^2 \exp(-i2\omega_1 t) + E_2^2 \exp(-i2\omega_2 t) + \\
&\quad + 2E_1 E_2 \exp(-i(\omega_1 + \omega_2)t) + 2E_1 E_2^* \exp(-i(\omega_1 - \omega_2)t) + c.c. \big] \\
&\quad + 2\varepsilon_0 \chi^{(2)} \big[E_1 E_1^* + E_2 E_2^* \big]
\end{aligned}
\tag{2.6}
$$

Here the first two terms containing $2\omega_{1,2}$ are the SHG terms (also called frequency doubling). They are followed by the SFG $\omega_1 + \omega_2$ and DFG $\omega_1 - \omega_2$ terms. The last bracket in the equation (2.6) is the so called optical rectification term (OR). The equation (2.6) is written as a scalar equation with the $\chi^{(n)}$ considered being scalar material constants rather than tensors. However this simplification does not change the basic nature of the listed terms and their dependence on the individual frequencies. These terms can be easily extended to the tensor susceptibilities version of the equation (2.6). In principle the SHG is the most often used to double frequency of a light source in order to get a shorter wavelength output. In this way one can get for instance 532nm output from a standard 1064nm Nd:YAG laser.

2.3 Up- and Down-conversion processes

In order to introduce a set of the coupled equations responsible for up and down-conversion processes, consider a nonlinear optical system with two beams in the system (see [3], [4] for more details). We call the beams fundamental beam (FW), frequency ω, and second harmonic (SH), optical frequency 2ω. The assumption is that the beams satisfy SVEA conditions. Therefore the evolution of the electric fields with propagation along z is given with the set of the coupled equations

$$i2k_{FW}\frac{\partial}{\partial z}E_{FW}(z)+\nabla_T^2 E_{FW}(z)=-2(\omega/c)^2 d_{eff}^{FW}E_{SH}(z)E_{FW}^*(z)\exp(-i\Delta kz)$$

$$i2k_{SH}\frac{\partial}{\partial z}E_{SH}(z)+\nabla_T^2 E_{SH}(z)=-(2\omega/c)^2 d_{eff}^{SH}E_{FW}^2(z)\exp(i\Delta kz)$$

$$(2.7)$$

here $\nabla_T=\dfrac{\partial^2}{\partial x^2}+\dfrac{\partial^2}{\partial y^2}$ and $\Delta k=2k_{FW}-k_{SH}=2k(\omega)-k(2\omega)$ is the so called, phase mismatch. If the phase mismatch is zero then the FW and SH waves have equal phase velocities. Δk depends on refractive index dispersion and therefore is wavelength, material temperature and propagating beam polarization dependent (in the case of anisotropic crystals, which is typically the case here). The first equation describes down- conversion and the second one up-conversion. In the process of up-conversion one 2ω photon (SH) is generated. In the down-conversion one 2ω and one ω photon generate one FW ω photon. Polarization information is implicitly included in the coupled equations through the d_{eff} coefficients. In its full form the quadratic nonlinear susceptibility tensor would be written as $\chi_{ijk}(-\omega,\omega_1,\omega_2)$. Here the i,j,k stand for the resulting and the two incident electric field polarization directions, respectively. The same with the frequencies, ω is

13

the frequency of the resulting wave, while $\omega_{1,2}$ are associated with the input waves. To make it easier to understand the nature of this notation assume that the two incident waves with frequencies ω_1, ω_2 are polarized along the x and y directions respectively. The resulting nonlinear polarization is given with $P_i = \varepsilon_0 \chi_{ixy}(-\omega, \omega_1, \omega_2) E_x(\omega_1) E_y(\omega_2)$ where i can be x, y or z. Typically most of the susceptibility tensor elements are equal to zero so that only one polarization component is finally generated. Therefore it comes naturally to define the effective d coefficient (d_{eff}) as

$$d_{eff} = \hat{e}(\omega) \times \frac{1}{2} \ddot{\chi}(-\omega, \omega_1, \omega_2) \times \hat{e}(\omega_1) \hat{e}(\omega_2) \tag{2.8}$$

Here the susceptibility tensor is sandwiched between the incident and resulting unit polarization vectors. d_{eff} quantifies the potential efficiency of the ongoing nonlinear process. A typical number for d_{eff} of "a good nonlinear material" is around 10pm/V, slightly varying with configurations (incident and resulting polarizations) and nonlinear media properties.

The susceptibility tensor has two more properties that strongly influence nonlinear behavior. The concept of intrinsic permutation symmetry is contained in the following expression: $\chi_{ijk}(-\omega, \omega_1, \omega_2) = \chi_{ikj}(-\omega, \omega_2, \omega_1)$. In addition to this intrinsic symmetry, a so called full permutation symmetry exists under a lossless media approximation. It implies $\chi_{ijk}(-\omega, \omega_1, \omega_2) = \chi_{jki}(-\omega_1, -\omega_2, \omega) = \chi_{kij}(-\omega_2, \omega, -\omega_1)$. In fact this implies that if a system consists of the same frequency components no matter if the process is SFG or DFG, the associated nonlinear parameter is the same. If these symmetry rules are applied to the coupled equations (2.7) $d_{eff}^{FW} = d_{eff}^{SH}$, which simplifies equations (2.7) to

14

$$\frac{\partial}{\partial z} E_{FW}(z) - iD\nabla_T^2 E_{FW}(z) = i\Gamma E_{SH}(z)E_{FW}^*(z)\exp(-i\Delta kz)$$

$$\frac{\partial}{\partial z} E_{SH}(z) - \frac{i}{2}D\nabla_T^2 E_{SH}(z) = i\Gamma E_{FW}^2(z)\exp(i\Delta kz)$$

(2.9)

where $\Gamma = \frac{(\omega/c)^2}{k_{FW}}d_{eff}$ and $D = 1/(2k_{FW})$.

2.4   SHG versus phase mismatch

Consider a system which for an input beam has a FW component only. With propagation some SH is generated due to the up-conversion. However, if the amount of generated SH is much smaller than the FW component, the system can be considered to be in the low depletion limit. Physically that means that the FW component remains essentially unchanged with propagation. From the point of the coupled system (2.9) that would mean that the right side of the first equation (down-conversion process) is negligible due to the small amount of the existing SH. Assuming further that the beams in the system are plane waves the diffraction terms from the right side of the equations automatically vanish. Therefore $E_{FW}(z) = const$. The generated SH intensity is given with

$$I_{SH}(\Delta k, z) = \frac{2}{nc\varepsilon_0}\Gamma^2 z^2 \operatorname{sinc}^2\left(\frac{\Delta kz}{2}\right)I_{FW}(z=0).$$

(2.10)

Here the sinc(x) function is defined as sinc(x)=sin(x)/x. Therefore, if the phase-mismatch Δk is zero the intensity of the generated SH grows quadratically with the propagation distance z in the nonlinear media. On the other hand it has an oscillatory behavior if $\Delta k \neq 0$. In addition, with larger Δk the period of the oscillations with propagation decreases.

15
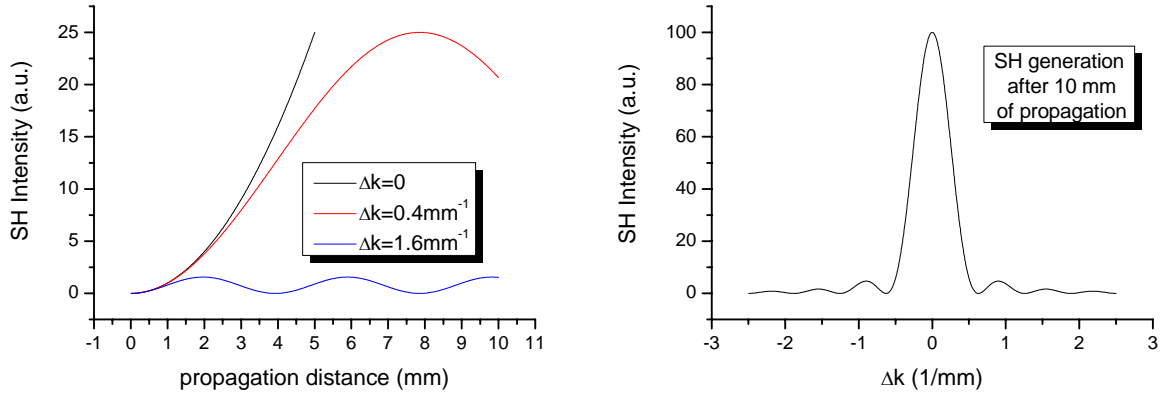
Figure 2.1: (left) SH generation with propagation distance for various phase mismatch parameters is shown. (right) sinc^2 type of behavior is numerically demonstrated for phase matching dependent SH generation after 10mm of propagation through a SH generation medium in the weak conversion limit.

Figure 2.1 shows the calculated behavior of the SH generation with propagation distance for several different values of Δk (left graph), and for a fixed propagation length the dependence on the phase mismatch (right graph). Obviously it is desirable to operate at small values of the phase mismatch to achieve an efficient SH generation. So far, only the low depletion limit was considered. However once the amount of converted FW becomes significant, depletion of FW has to be taken into account as well. The problem can be efficiently treated analytically at phase matching yielding a $\tanh(z/l_{PG})$ dependence of the SH intensity increase and a $\mathrm{sech}(z/l_{PG})$ FW intensity decrease with propagation z. Here $l_{PG} = 1/(\Gamma E_{FW}(z=0))$, representing a $1/e$ FW intensity drop after propagation for a $z = l_{PG}$ distance through the SH generation medium. The non-phase matched case shows quite a complex behavior that can be described in the form of

16

Jacobi elliptic functions. The main features of the solution are that an increase in the input FW leads to a narrowing in bandwidth, an increase in SH generation side-lobes and an inward collapse of the side-lobes. Therefore it is very different from the low depletion behavior demonstrated in Figure 2.1(right side graph).

2.5 Large phase mismatch and effective Kerr approach

From the previous chapter it was shown that SHG is strongly influenced by the phase matching condition. Large phase mismatched configurations tend to generate low average intensity SH and with propagation this SHG undergoes very rapid intensity oscillations. Furthermore, the FW is never depleted significantly and one can solve the up-conversion equation from (2.9) getting for the SH electric field

$$E_{SH}(z) = \Gamma E_{FW}^2 \frac{\exp(i\Delta kz) - 1}{\Delta k}. \tag{2.11}$$

By substituting the calculated SH field into the down-conversion equation in (2.9)

$$\frac{\partial}{\partial z} E_{FW}(z) - iD\nabla_T^2 E_{FW}(z) = i\frac{\Gamma^2}{\Delta k} \left| E_{FW}(z) \right|^2 E_{FW}(z)\left(1 - \cos(\Delta kz) + i\sin(\Delta kz)\right). \tag{2.12}$$

Considering a large Δk the conversions are very rapid and $\cos(\Delta kz) + i\sin(\Delta kz)$ averages out. Therefore the equation (2.12) becomes

$$\frac{\partial}{\partial z} E_{FW}(z) - iD\nabla_T^2 E_{FW}(z) = in_{2,eff} \left| E_{FW}(z) \right|^2 E_{FW}(z) \tag{2.13}$$

where $n_{2,eff} = \Gamma^2 / \Delta k$

This is a standard equation for a Kerr medium (third order nonlinear effect) with the difference

that $n_{2,eff}$ is both material and phase matching dependent, while in a real Kerr case it is only a material constant. Also, as can be seen from the definition of $n_{2,eff}$ that it can be both positive and negative. Therefore, if one operates far from phase matching the system behaves as a Kerr medium with a tunable nonlinear coefficient. However the nonlinear coefficient drops with phase mismatch and higher intensity is required in order to get nonlinear effects at large phase mismatch.

2.6 Phase matching

As discussed in details in the previous paragraphs, phase matching is a very important variable in quadratic nonlinear processes. Therefore it is important to know how to achieve a desired Δk value. From its definition $\Delta k = 2k(\omega) - k(2\omega) = \dfrac{2\omega}{c}\left(n(\omega) - n(2\omega)\right)$ it is obvious that because of material dispersion effects one cannot achieve $n(\omega) = n(2\omega)$. This is because in an isotropic medium far from a resonance phase matching cannot occur since only a single, monotonically decreasing, dispersion curve exists. However phase matching can be achieved under some specific conditions in uniaxial and biaxial crystals. This is so called birefringent phase matching. Another way would be to use a QPM (quasi-phase-matching) technique. For a review on the QPM technique see ref [5]. Birefringent phase matching and QPM techniques are not the only methods that can be used in satisfying $\Delta k = 0$ condition, however in this work only these two ways were used.

18

2.6.1 Birefringent phase matching

Birefringent phase matching relies on a correct combination between the beam polarizations and the orientation of the nonlinear medium in order to get $\Delta k = 0$. Historically this phase matching method was used in the first quadratic spatial soliton experimental observation [6]. In the simplest configuration, the so called Type I phase matching (Figure 2.2a), the FW and the SH are orthogonally polarized. Considering a uniaxial crystal and assuming an ordinary SH and an extraordinary FW, the phase matching can be achieved by tuning the incident beam angle. Technically this is realized by rotating the crystal itself. For this case the angle between the uniaxial crystal optical axis and the phase matching wavevector (k_{PM}) is given as:

$$\sin(\theta_{PM}) = \frac{n_e(\omega)}{n_0(2\omega)} \sqrt{\frac{n_0^2(\omega) - n_0^2(2\omega)}{n_0^2(\omega) - n_e^2(\omega)}}. \tag{2.14}$$

Obviously, the angle is completely determined by the material dispersion curves and fixed for a particular material by the choice of wavelength. In the same way one can consider a different configuration where the FW is ordinary and the SH extraordinary. The result for the θ_{PM} is almost identical.

Another birefringent phase matching configuration is the so called Type II phase matching (Figure 2.2b). Here the fact that two orthogonally polarized FW photons generate a single SH photon is used in manipulating Δk. The equation $n_e(2\omega,\theta) = \frac{1}{2}\left[n_0(\omega) + n_e(\omega,\theta)\right]$ has to be satisfied in order to achieve the phase matching condition within a Type II

configuration if SH is an extraordinary wave, or $n_0(2\omega) = \frac{1}{2}\left[n_0(\omega) + n_e(\omega,\theta)\right]$ if it is an

ordinary wave. In this work the Type I phase matching is used and therefore the details on the

Type II configurations are not further discussed.
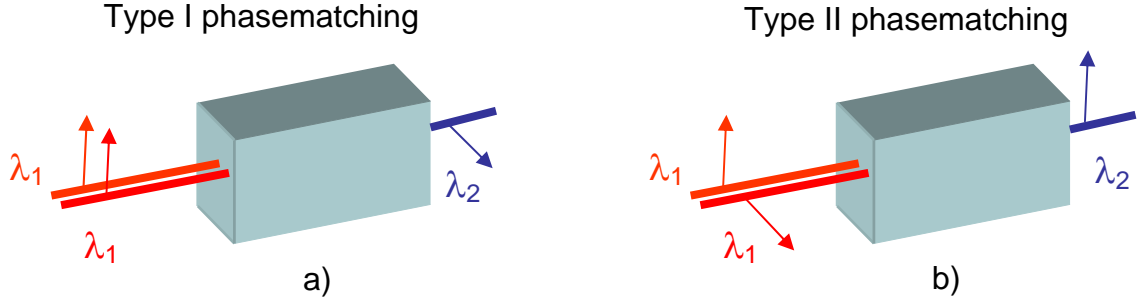
Figure 2.2: The birefringent phase matching configurations a) FW photons (λ_1) are parallel b) orthogonal.
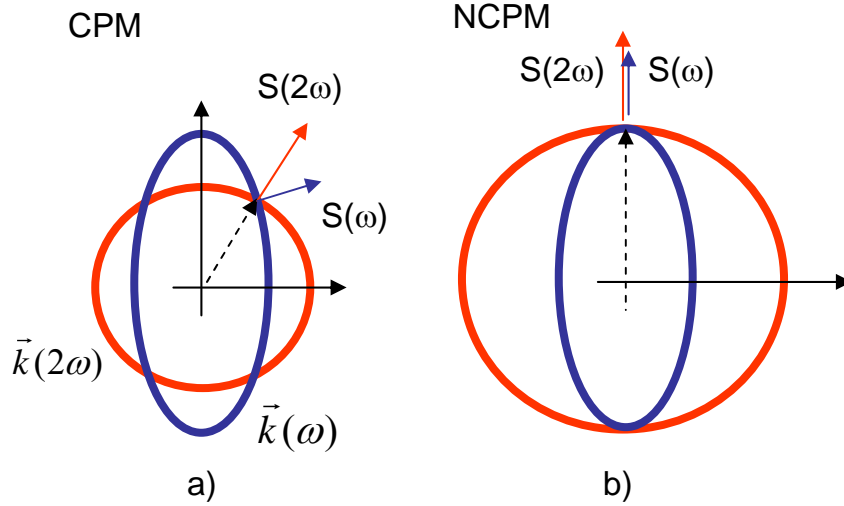
Figure 2.3: k vector ellipsoids are shown for the FW and the SH beam. a) Type I critical phase matching configuration (CPM) b) Type I noncritical phase matching (NCPM). Notice that in the NCPM the Pointing vectors (S(ω)for FW and S(2ω) for SH) are parallel while in the CPM case they are not.

The two major drawbacks usually connected with the birefringence phase matching method are: a) sensitivity to temperature changes, which is especially prominent in the Type II configurations; and b) inability to take advantage of the largest terms of the $\chi^{(2)}$ nonlinear tensor which are usually the diagonal ones.

An important limiting case of birefringent phase matching is noncritical phase matching (NCPM). Within the phase matching concept the acceptance angle is defined as the deviation of the incident FW angle from the phase matching angle that still provides an efficient SHG. For the SHG response in Figure 2.1, the high conversion Δk bandwidth extends to around $\pm \Delta k L = \pi$, where L is the SHG crystal length. Since $\Delta k(\Delta \theta)$ is a function of $\Delta \theta$, where $\Delta \theta = \theta - \theta_{PM}$, it is desirable to have a slow changing $\Delta k(\Delta \theta)$ around the phase matching point $\Delta \theta = 0$. For a Type I configuration with an ordinary SH wave the acceptance angle is given with

$$\Delta \theta \approx \frac{c\pi}{2\omega L} \left[\{ n_0(\omega) - n_e(\omega) \} \sin^2 (2\theta_{PM}) \right]^{-1}. \tag{2.15}$$

The equation is valid as long as $\theta_{PM} \neq 0$. In the case of noncritical phase matching ($\theta_{PM} = 0$) the index of refraction curves for the FW and the SH are tangential rather than crossed as they are for the critically phase matched configurations. Once the NCPM is achieved the acceptance angle changes to

$$\Delta \theta \approx \sqrt{\frac{c\pi}{2\omega L (n_0(\omega) - n_e(\omega))}}. \tag{2.16}$$

Therefore typically NCPM has much wider acceptance angles. Another point is that in the NCPM configurations the wavevector directions are along the crystal axes and there is no spatial walk-off between the FW and the SH propagation directions (a consequence of their Pointing

21

vectors being parallel). These two great advantages of NCPM make NCPM the most favorable configuration for performing the SHG and quadratic spatial soliton experiments [7].

2.6.2   Temperature tuning and phase matching

Material dispersion is always temperature dependent. Therefore it is possible by changing the material temperature to slightly shift the phase matching wavelength from its original "room temperature" phase matching value. This is a very common technique often used for fine tuning a configuration in the vicinity of its phase matching conditions. The tunable range is strongly material and phase matching type dependent. Typically Type II phase matching is an order of magnitude more sensitive to temperature changes than the NCPM configuration.

2.6.3   Quasi phase matching technique

Another phase matching technique that is gradually becoming more popular is quasi phase matching (QPM). The technique was first suggested in 1962 [2], at the time of the discovery of SHG. However, because of the fabrication difficulties, the method was the first realized in 1980s [5]. It was based on artificial modification of the original nonlinear properties during the sample fabrication process.
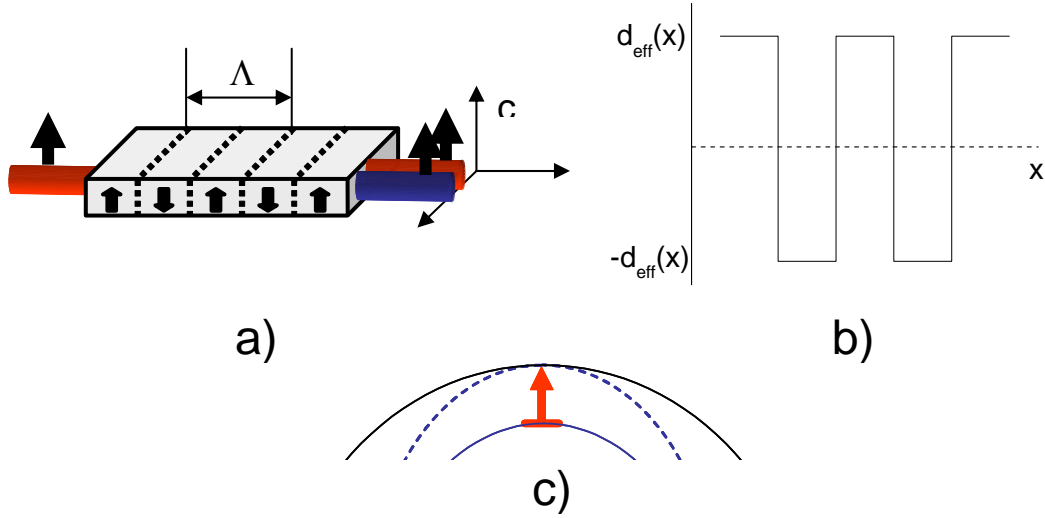
Figure 2.4: a) A QPM sample is shown. The arrows indicate the domain orientation. Λ is the corresponding periodicity of the QPM structure. c indicates the optical axis of the crystal. The beams propagate along the x direction. The arrows associated with the beams indicate polarization directions. b) Periodic variation of d_{eff} along the sample is shown. It alternates between d_{eff} and - d_{eff}. c) The $k(\omega)$ and $k(2\omega)$ curves are shown. QPM translates one curve resulting in phase matching. Notice that the curves are tangential.

The periodic structure shown in Figure 2.4 is a QPM. It has periodically flipped ferroelectric domains in the way indicated by the arrows. This can be achieved during the fabrication process by heating the sample to near the ferro-electric phase transition temperature (material dependent) and then applying a periodically patterned high voltage. After an appropriate period of time the applied voltage causes reorientation of the domains wherever the voltage is applied. After this process the domains remain identical except that the optical axes point in the opposite directions. The main challenge still remains the making of high quality sample, i.e. achieving uniformity across the sample and an unbroken QPM along the whole sample length.

23

A mathematical background for the QPM technique is given in the following paragraph. Since *d(x)* changes periodically along the crystal we can decompose it into a Fourier series

$$d(x) = \sum_p d_p \exp(ipKx) \tag{2.17}$$

Here $K=2\pi/\Lambda$. The coefficients d_p can be easily found from (2.17) from the details of the *d(x)* dependence. If we assume that the domains pointing upward and downward are of the same size, then only the odd terms in the series (2.17) remain. $d_p = 2d_{eff}(-1)^{(p-1)/2}/(p\pi)$, where *p=1,3,5,...* . The right side of the equation (2.9) becomes $\sum_p d_p E_F^2 \exp[i(\Delta k + pK)]$. Therefore if

$\Delta\tilde{k} = \Delta k + pK = 0$ for a certain *p* the phase matching condition is satisfied. Because $d_p \propto p^{-1}$, one tends to achieve the phase matching condition for the smallest *p* values, primarily $p=1$. Note that phase matching can be achieved at any desired wavelength. Therefore, the QPM technique makes available for nonlinear optics at convenient wavelengths materials which otherwise require using tunable laser systems. The most often used polarization configuration (with co-polarized FW and SH), is the one shown in Figure 2.4a. This configuration is also sometimes called Type 0 phase matching configuration. Because at phase match the FW and the SH index of refraction curves are tangential (Figure 2.4c), this configuration satisfies NCPM conditions. It is also very beneficial to combine the QPM with the temperature tuning to get more variable system parameters.

CHAPTER THREE: LIGHT SOURCE

3.1 Picosecond Laser

A commercial mode-locked picosecond Nd:YAG laser (EKSPLA PL2143A) was used as a light source in all of the experiments discussed in this work, either providing the laser beam for the experiments directly or serving as a pump laser for a tunable OPG-OPA. This unit is discussed in more detail in this chapter.

What follows is a brief overview of the working principles of the laser the schematic of which is reproduced in Fig. 3.1. A Nd:YAG rod (R1) pumped with the flash lamps enables the cavity to build up an oscillating optical field. The cavity is defined by a mirror M1 on the left side and a dye cell and a spherical mirror M5 on the right side. The dye gives passive modelocking and is the component that requires the most frequent maintenance since the dye "age" is crucial for the laser output shot-to-shot energy stability. A single pulse of 25ps duration is formed and travels back and forth in the cavity. It is stabilized by two Pockels cells (PC1 and PC2). PC1 is modulated with a RF signal closely adjusted to the cavity round trip time. It works as a timed shutter forcing the oscillator to form a single pulse. This allows the oscillator to build

up a low intensity stable oscillation for a well defined duration. Once the pulse is formed, the Pockels cell PC2 is activated, effectively working as a half wave plate. The polarization is flipped 90^0 causing a new cavity to be activated (whose left end is defined by the M2 mirror) once light is reflected by the polarizing beamsplitter P1. The previously formed pulse in the main cavity travels about 10 round trips in the new cavity gaining intensity until eventually the complete depletion of the population inversion occurs in the Nd:YAG rod. Once the pulse reaches a pre-set intensity it is extracted via Pockels cell PC3 and a polarizing beamsplitter P5. The pulse is further amplified in a double-pass Nd:YAG amplifier rod (R2). This amplified pulse passes through a BBO SHG crystal. Green 532nm (SHG beam) and 1064nm (original laser beam) light are separated by a sequence of polarization dependent beamsplitters. The 1064nm output can reach up to 25mJ and the 532 up to 11mJ. The output power can be controlled additionally by adjusting the timing of the amplifier rod flashlamp pumping. If pumping coincides with the pulse transit time the amplification is more efficient, resulting in higher output beam energy. The repetition rate is determined by the flashlamp's pumping rate that can be set to be as high as 10Hz.

The laser has an additional option by which it is possible to obtain either 25ps (initial configuration) or 50ps pulses. Switching from one mode to the other is relatively easy to control by a flip-adjustable Fabry-Perot etalon placed between P2 and QWP2. Unfortunately both modes have roughly the same bandwidth (0.16nm in 25ps and 0.13nm in 50ps case), and therefore experiments based on variable bandwidth are not supported by the existing laser system. For a more detailed discussion on solid state laser working principles see ref. [1]
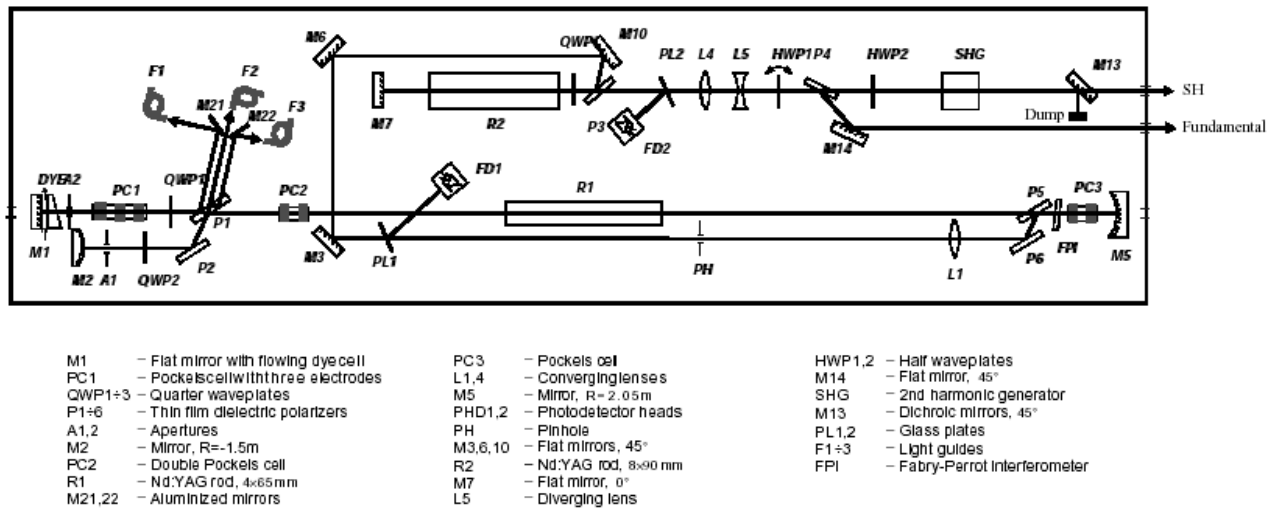
Figure 3.1: Schematic of the EKSPLA PL2143A Nd:YAG laser. The cavity is defined by mirror M1 on the left side and a dye cell and a spherical mirror M5 on the right side. The dye gives passive modelocking and is the most frequently maintained part in the laser (since the dye "age" is crucial for the laser output energy).

The laser described was far the best one in its category commercially available at time of purchase. Recently, however, some competing designs have appeared on the market. Those could eventually overcome the problems associated with this laser configuration. As already mentioned, one of the major problems is the use of dye as a saturable absorber which requires regular maintenance and reduces measurement accuracy over long time periods. In addition, the full dye change process requires several steps involving directly the laser cavity adjustment, resulting in a small, but noticeable change in the beam directionality. Since the laser beam is used as a pump for another tunable unit, this small directionality problem becomes a significant problem requiring a serious adjustment of the tunable unit. A solution to this problem, as pointed out by the Quantronix-Continuum picosecond lasers development team, is to use solid state

27

saturable absorbers. They are just as efficient as the dye saturable absorbers, more reliable and do not require maintenance.

Another problem often associated with this laser is the low repetition rate. The company currently offers a version with a 50Hz repetition rate with indications that 200Hz could be reached in the near future. Higher repetition rates can be achieved only by using diode pumping instead of the flashlamp pumping used in the current laser design. However, moving toward the diode pumped design immediately cuts the output by an order of magnitude with a maximum output of 5mJ only. Most of the applications, in fact, do not require even a mJ output. However to pump a tunable unit one has to achieve a minimum pump power. Naturally the solution is to increase the conversion efficiency of the tunable sources to better than the 10-17% conversion currently achieved with the EKSPLA tunable source.

3.2   OPG-OPA tunable source

The green 532nm output was used to pump an EKSPLA Optical Parametric Generator-Amplifier (OPG-A) which is tunable from 680nm to 2300nm. The average output energy is wavelength dependent and typically higher than 0.2mJ. The output energy stability of the OPG-A (usually around 10% rms) is mainly influenced by the pump laser stability (usually below 1.5%). As seen from the schematic bellow (Figure 3.2) the input beam is divided into two beams, with the weaker one (15% of the input) making a double pass through an OPG crystal. The crystal is adjusted by automatic angle tuning to give a seed wavelength for an OPA crystal. Once the seed beam is created, the pump 532nm is filtered out and the seed is narrowed in bandwidth

by passing it through a lens-grating-pinhole-lens system. Finally the seed beam and the stronger part of the pump are combined in the second BBO crystal working as an OPA. (For more details on the basic physics of the OPGs and the OPAs see refs. [2, 3].)
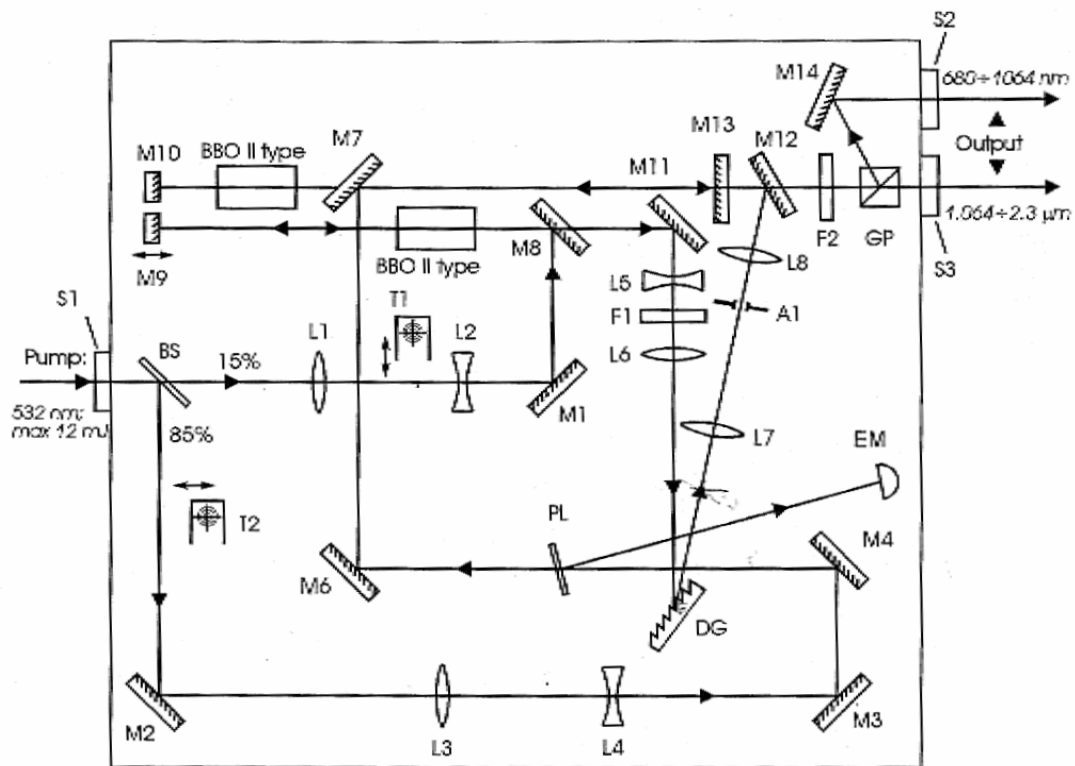
Figure 3.2 Schematic of EKSPLA PG501VIR OPG-A.

Naturally, the section where the seed and the pump are combined is very sensitive to the alignment. It determines the bandwidth stability, shot-to-shot energy stability and output beam profile. In fact, the above mentioned 0.5nm bandwidth is an average bandwidth measured over a number of laser shots. However, from the single shot measurements, performed by using of a

monochromator with a CCD camera at the output, the single shot OPG-OPA bandwidth was estimated to be around 0.2-0.3nm.

The output beam profile and the beam divergence are determined by a number of factors, primarily by the pump laser beam divergence, the seed-pump alignment inside the OPG-A unit, the seed beam central wavelength versus OPA crystal orientation, etc. Therefore it is a very complex task to maintain the same quality of the OPG-A output beam over a long period of time. In order to solve this problem and to provide the long term stability of the output beam profile, directionality and divergence, it is necessary to use a special spatial filtering approach where an additional aperture is used. The aperture (2mm opening) was placed just before the spatial filter focusing lens. The aperture provided constant tunable laser source beam size which was of great importance for efficient operation of the spatial filter. The beam was focused down and spatially cleaned after passing through a 75μm pinhole. This two step procedure provided a laser beam with excellent beam profile quality (M^2 laser beam coherence factor close to one). A drawback was the resultant shot-to-shot energy stability. Instead of the initial 10% rms the instability increased to 12% rms. LabView control of the experimental setups and the data acquisition was needed to avoid this problem. It provided simultaneous measuring of the camera images and all the setup detectors on a shot-to-shot basis. In this way the experimental errors were significantly reduced.

CHAPTER FOUR: BASICS OF QUADRATIC SPATIAL SOLITONS

4.1   The Concept of a spatial soliton
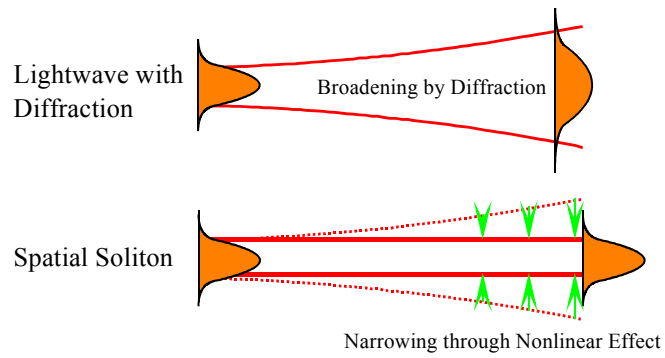
Figure 4.1: Propagation of light in a linear medium (top). Soliton propagation in a nonlinear medium (bottom)

The nonlinear optics world is considerably different from the linear one, even at its very foundations. For instance, plane waves, the natural eigenmodes of a linear system, tend to show filamentation and beam-breakup if propagated in a nonlinear medium (quadratic systems [1, 2] and Kerr systems [3]). Moreover, the nonlinear system eigenmodes are the localized solutions

called solitons. If constrained to CW beams and the spatial domain, one is interested in spatial solitons only. The spatial solitons maintain their transverse beam profiles while propagating in a nonlinear medium. In addition, they are stable against various small amplitude and/or phase perturbations. Moreover, they are robust, evolving even from inputs with parameters that are initially quite far from a soliton solution, as will be evident in the following chapters.

To illustrate the basics of spatial soliton formation, a laser beam tightly focused onto a nonlinear medium is considered. The beam tends to broaden as a result of diffraction (Figure 4.1a). The effect is governed by Maxwell equations and is a completely linear behavior. However, if the beam intensity is gradually increased, it starts to narrow due to nonlinear processes, as shown in Figure 4.1b. If the narrowing caused by the nonlinear effects cancels the broadening caused by the liner effects the beam propagates without changing of its transverse profile. If the feature is stable to perturbations it is called a spatial soliton.

To get more insight into the basic features of solitons, the so called, Kerr solitons are considered first. Kerr soliton-like behavior can be recognized in quadratic nonlinear systems at large phase mismatch conditions, as introduced in section 2.5. Even though the main goal of this dissertation is to investigate the (2+1)D systems here a (1+1)D system is considered since Kerr systems do not support stable, soliton type of solutions in (2+1)D configurations. Considering a planar waveguide configuration with a Kerr nonlinearity, a laser beam launched into this structure will behave according to the following equation:

$$\frac{\partial}{\partial z} E(z, x) - iD \frac{\partial^2}{\partial x^2} E(z, x) = in_2 |E(z, x)|^2 E(z, x) \qquad (4.1)$$

32

A solution of the equation (4.1) is of the form

$$E(z, x) = \sqrt{\frac{2D}{n_2 a^2}} \frac{1}{\cosh(x/a)} \exp\left(i \frac{D}{a^2} z\right). \qquad (4.2)$$

Obviously, the x and z dependences are separated. Therefore, the wave propagates in the z direction without change of its transverse profile in the x direction. The nonlinear propagation does introduce an additional, nonlinear contribution to the phase. In addition, notice that the resulting field amplitude is fixed by the material constants and the beam spot size a. The soliton transverse shape is given by $1/\cosh(x/a)$. The initially launched Gaussian beam shape has to evolve with the propagation into the soliton solution, requiring some propagation distance and radiation loss in the soliton formation process.

From a less mathematical point of view, the propagating beam induces a nonlinear index change in the region where it propagates. Based on equation (4.1), the induced index change comes from the nonlinear part and is $\propto n_2 |E|^2$. Once the index is locally changed, a waveguide is generated. The waveguide takes the shape of the propagating beam so that the beam satisfies the waveguiding conditions. In that way the induced beam profile causes a small change in the waveguide itself, in the next iteration step. Therefore, the equation has to be self-consistently satisfied in the plane of the waveguide. The self-consistent solution is the one already given with (4.2). Therefore, it is clear that the soliton solution results from the self-guiding effect. In the case of quadratic nonlinear systems, different from Kerr systems, there is no index of refraction change involved in the self-guiding processes. The background for the self-guiding is in the up- and down- conversions, as experimentally demonstrated in the following chapters.

4.2   Introduction to quadratic spatial solitons

Theoretically predicted in 1975 [4], quadratic spatial solitons were experimentally observed for the first time in a Type II phase-matched bulk KTP crystal [5]. Using the OPG-OPA unit as a tunable laser source gives a unique opportunity to observe this type of phenomena under non-critically phase-matched conditions.

The previous section discussed one of the aspects of quadratic solitons that can be obtained analytically. A limiting case of quadratic solitons with the very extensively investigated Kerr solitons has been identified. However, there is another analytical solution. Different from the Kerr case where the solitons have a sech(x) field profile, this additional solution (at a finite phase-mismatch) has sech^2(x) behavior for both the FW and the SH. Moreover, the ratio between the two harmonics is finite, i.e. nonzero, given by $E_{SH}/E_{FW} = \sqrt{2}/2$, under the conditions restricted to $a^2(2k_{FW} - k_{SH})k_{FW} = -3$ [4, 6]. This gives $sign(2k_{FW} - k_{SH})(2\pi L_d/L_{ch}) = -3$, where $L_d = (\pi a^2 n/\lambda)$ is a characteristic diffraction length, $L_{ch} = \pi/|\Delta k|$ coherence length and a is beam width. However, for all other cases it is necessary to treat quadratic nonlinear systems numerically.

A typical numerical method for solving the coupled equations system (2.9) is the beam propagation method (BPM), also known as the split step method.[7] It involves solving the linear and nonlinear propagation terms separately. A single propagation step is divided into the two half-steps. In the first half-step the nonlinear influence is neglected. The beams propagate under the linear effect (i.e. diffraction) only. An effective way to perform this step is by solving of the equation in Fourier transform space. During the second half-step the propagation is

34

diffractionless and the coupled nonlinear equations are solved by using the 4th order Runge-Kutta solver [7]. The BPM formulated in this way is a very powerful tool for performing numerical soliton simulations. Another alternative would be to use a FDTD (finite difference time domain) approach [8]. However, the FDTD is exceptionally time and memory consuming. Therefore, it is not very suitable for investigating 2D quadratic systems with a typical propagation distance of around 10mm, which is exactly the main goal of this work.

In Figure 4.2 is given an example of simulated (1+1)D quadratic soliton generation. Here the (1+1)D designates one transverse dimension and one time or propagation dimension. A Gaussian beam was used as the input field profile in the numerical simulations. Only the FW was launched. Choosing this input condition means starting very far from the soliton solution. However, this corresponds to a typical experimental environment. As indicated by the analytical solution given earlier, the FW and the SH components have comparable intensities in a steady-state soliton. The missing SH in the simulations is generated due to the up-conversion process which occurs initially on propagation in the nonlinear medium. As can be seen in Figure 4.2a there are several strong intensity SH oscillations before a quasi stable solution is reached. Figure 4.2b shows the FW intensity profile on propagation through the medium. Corresponding to the intensity SH conversions in Figure 4.2a there are several large oscillations along the soliton formation path shown in Figure 4.2b. Notice the significant amount of energy radiated from the vicinity of the second peak along the propagation path. The process of quadratic soliton generation is clearly nonadiabatic. In fact, by putting more energy into the system the radiated part grows larger. Therefore, a higher input FW power does not necessarily mean more efficient soliton generation. It is usually considered that an experimentally formed soliton is essentially

generated after several intensity oscillations (2-3). This occurs typically after about three diffraction lengths ($3 \times l_D$ is typically around 3-5mm in our case). In the next stage of the propagation the "soliton" undergoes small magnitude transverse profile adjustments followed by small magnitude intensity oscillations.
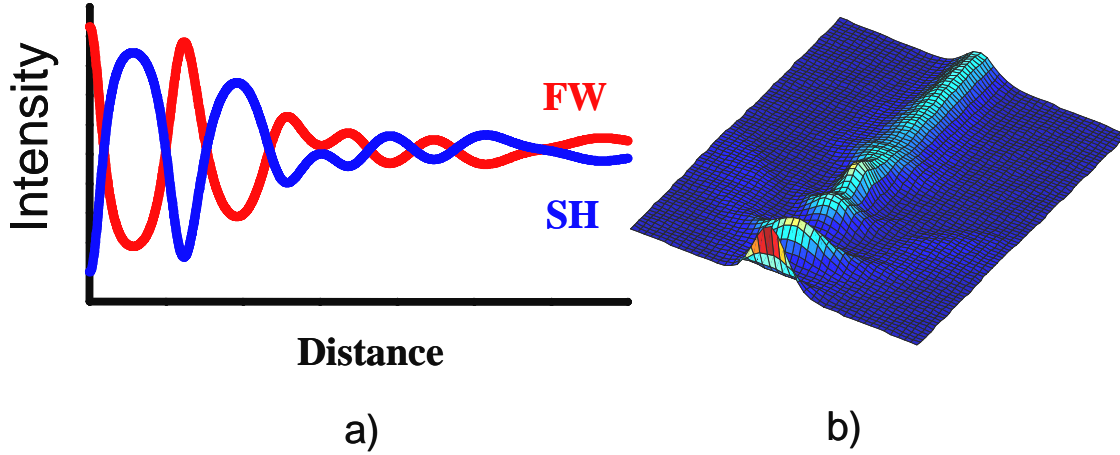
Figure 4.2: (1+1)D numerical simulations show the details of soliton generation. Only the FW beam is input into the nonlinear medium a) Peak intensity versus distance for both FW and SH is shown. b) Under the same conditions as in a) the FW intensity profile with propagation distance is shown. Notice the radiated energy from the second hump. A soliton is well formed after half of the propagation shown.

Notice that both the FW and the SH are required in order to generate a soliton. This is very different from the effective Kerr case, where the SH component does not follow the FW dynamics and is almost negligible (but never zero) in magnitude. Based on the basic equations set (2.9) it is known that quadratic systems do not generate index of refraction change. Here the index of refraction point is understood from the Snell's law aspect. For instance one could launch a probe beam of different wavelength and polarization such that it crosses the quadratic spatial

36

soliton path. Since the probe beam will not interact, no deflection occurs. Thus there is no indication of an index of refraction change associated with the quadratic soliton. Therefore, the physics behind the quadratic soliton formation differs from that in all other optical soliton systems.

Intuitively it is clear that the narrowing can be associated with the SHG processes. To see this one can take a gaussian FW as an input beam ($\sim exp(-r^2/w^2)$) and set $\Delta k=0$ (phase-matching). In the up-conversion equation, describing conversion of the FW to the SH, the FW comes squared. Thus the generated SH is $\sim exp(-2r^2/w^2)$, and hence narrower than the initial FW. This new SH and the remaining FW interact in the down-conversion process leading to narrowing of the FW $\sim exp(-3\ r^2/w^2)$. Therefore, narrowing can be induced by the conversion processes alone. Another important factor is the phase mismatch Δk. The effect of the phase-matching factor is known as cascading. Further narrowing occurs if Δk is positive (medium acts as a positive lens, giving a positive curvature to the wave-fronts). If negative, it effectively leads to defocusing and hence competes with the narrowing caused by the above mentioned "conversion narrowing". Once the natural diffraction and the narrowing caused by the nonlinear effects are equal, (this is satisfied when the diffraction length $L_D = \pi w_0^2 n/\lambda$ and the parametric gain length $L_{pg} = 1/\Gamma\sqrt{I}$ are approximately equal) conditions for the creation of a soliton are satisfied. Even though the steady-state beam profiles are invariant under the propagation, the beams (FW and SH) continue to interact with each other. The photons exchange rate is now equally fast for up- and down-conversion and hence effectively the net conversion is zero. Furthermore, with propagation a nonlinear phase rotation occurs. Here the phase rotation is understood as a phase change

associated with the quadratically nonlinear properties of the medium. Both FW and SH are gaining some phase change with the propagation, however in a soliton their phase difference is constantly zero even though their individual phases are changing with the propagation. For instance in the Kerr limit discussed above an analytical solution was given with equation (4.2). For this particular solution the phase associated with the nonlinear process (nonlinear phase rotation) is given with $\exp(-Dz/a^2)$. Mutually trapped into a quadratic spatial soliton, the FW and SH are in-phase and have constant phase across the beams [9].

In the previous paragraph the basics of spatial soliton generation were given. The system consisted of a FW launched into a nonlinear medium. This type of configuration is sometimes called the SHG regime configuration. Another experimentally explored configuration is the OPA configuration [10] where the SH is launched into a crystal. The conversion process follows either due to a small initial amount of FW launched along with the SH or from the quantum noise. This regime is not investigated here. Also, the previously discussed spatial solitons are bright spatial solitons, which constitute only one of the soliton categories. However, in this work only bright spatial solitons generated in the SHG regime are investigated and discussed.

CHAPTER FIVE: SPATIAL SOLITONS AND MULTI-SOLITONS PROPERTIES

In this chapter the details of the soliton and multi-soliton generation are discussed. The potassium niobate (KNbO$_3$) crystal configuration is particularly interesting since the noncritical birefringent phase matching can be achieved at room temperature at 983nm FW. In addition, the material has a very large nonlinear coefficient associated with this NCPM. Therefore it does not come as a surprise that KNbO$_3$ solitons were demonstrated to have the lowest threshold for soliton generation among all birefringently phase matched materials.

5.1   Potassium niobate material properties

Tunable laser systems, like the one described earlier, are an important technology in the development of soliton science. Particularly in the case of potassium niobate the most attractive features were expected to occur at ~983nm. KNbO$_3$ is a biaxial crystal with a large, phase-matchable quadratic nonlinear coefficient of 16 pm/V [1, 2]. The drawbacks are usually related to fabrication difficulties. A well-known problem is the fabrication of large quantities of KNbO$_3$ samples/devices with the same optical properties. Another problem particularly important for SHG is the relatively strong two photon absorption around 490nm [3].

The crystal available from Peter Gunter's group at ETH for the experiments was a crystal with the [010] cut. This can be used for noncritical, Type I, birefringent phase matching at $\approx$983nm around room temperature ($\approx 20^0$C). Under room temperature conditions the $KNbO_3$ can be non-critically, Type I, phase matched at both 983nm and 857nm for different cuts, and Type II phase matched at 1171, 1402 and 3172nm [1, 4]. At 983nm the non-critical phase matching occurs for the FW polarized along the crystal's a-axis and the resulting SH along the c-axis. The propagation direction is along the b-axis (our current sample case). In this configuration $d_{eff}=d_{13}$ has a very high value of 16.4pm/V [1].

5.2   Experimental setup
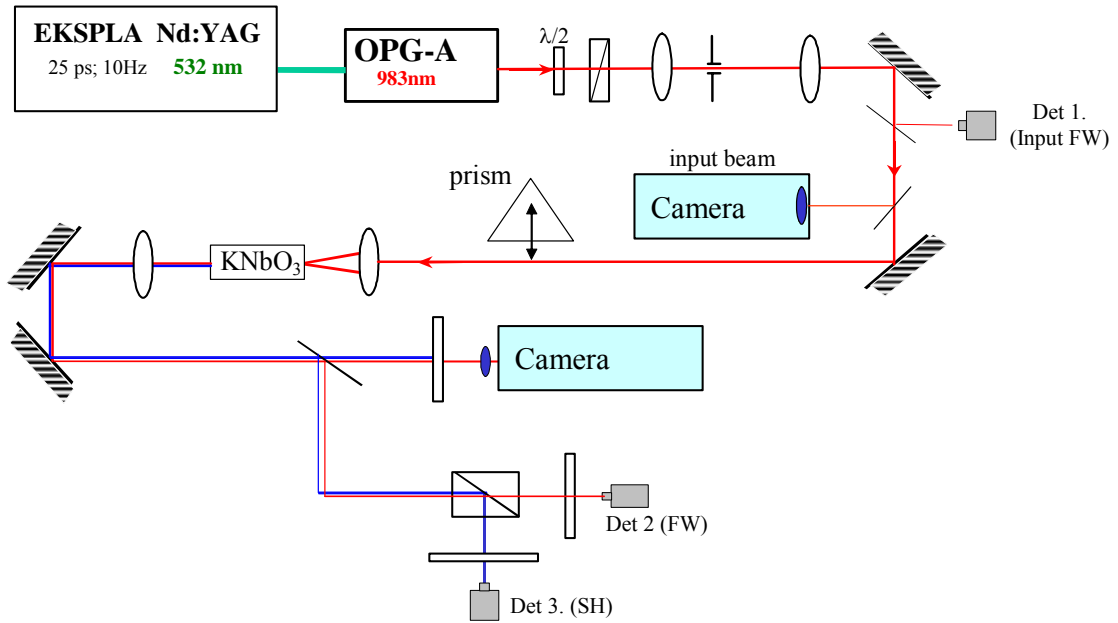
Figure 5.1: $KNbO_3$ experimental setup.

The experimental setup, as shown in Figure 5.1, was in fact the final design. The setup was initially used in the potassium niobate (KN) quadratic soliton generation and the threshold measurements. However, due to some complexities in the soliton generation, such as the formation of the multi-solitons, the same setup was later used to investigate the detailed multi-soliton features. The OPG-OPA unit was tuned to have the output at around 983nm (the NCPM condition). Even though the output OPG-OPA beam was of a good quality (round and uniform after several meters of propagation), to make it more Gaussian-like and to achieve a higher degree of coherence (M^2 close to one), spatial filtering was applied. In fact, the beam was first partially confined by a 1-2mm aperture. After passing through the aperture the beam was spatially filtered with a 75μm pinhole. The beam quality was improved but the energy stability slightly decreased (caused by the OPG-OPA's pointing instability). To solve this issue, a LabView computer control was performed. In addition, the spatial filtering pinhole was used to control the beam ellipticity. That was a crucial element in investigating the multi-soliton features. The OPG-A unit provided up to 100GW/cm^2 confined in a Gaussian shaped FW. A set halfwave plate-polarizer was used to control the beam energy and the polarization state (horizontal in this experiment). The FW only (983nm) was focused down on the input sample facet. For the three different configurations that were used, a 10cm planoconvex, 13cm doublet and a 8cm planoconvex focusing lenses produced beam sizes of 22, 16.4 and 18μm at the sample surface, respectively. Another lens imaged the output from the sample onto a CCD camera. To monitor the beam symmetry, an additional camera was used to capture the spatial profile of the input beam before it was focused down onto the sample. In that way the input beam asymmetry was

known. The detectors (input beam, output FW and output SH) and the cameras were synchronized and driven on a shot-to-shot basis by the LabView programs.

Before arriving at this final setup design, several other possibilities were investigated. For example, a smaller beam spot size in the focal plane had been tested. However, it was found that the small input spot was not able to evolve into a quadratic soliton. The reason for that was that higher intensities are required for soliton formation and this increased the two photon absorption for the SH. Moreover, in order to achieve a better beam profile the output beam from the OPG-A was propagated for around 6 meters before it was focused down on the crystal. The resulting beam was very symmetric. However, it turned out that even small disturbances, like turning on and off the laser, could change the focusing plane position by about 50μm, which was at the tolerance limits of the alignment. In addition, the generated solitons would "wander" over about 50μm in the crystal output plane. Since one of the main goals was to perform soliton collisions these problems were intolerable. Therefore the building of the setup as shown in Figure 5.1 was crucial.

5.3   The noncritical phase matching wavelength condition

The OPG-OPA unit can be tuned with 0.1nm precision and it is important to note that a 0.1^0C temperature change gives a 0.03nm change in the NCPM wavelength. For the given 11.4mm KN sample the acceptance bandwidth is around 0.15nm.The multi-shot averaged measured bandwidth at 983nm is $\cong 0.5$nm. As already mentioned in the Light source chapter, the single shot laser bandwidth is around 0.3nm and the OPG-OPA source has a shot-to-shot

frequency jitter giving the 0.5nm average laser bandwidth. It is important to understand that with the 0.5nm single shot bandwidth, the nonlinear process would use only a fraction of the incident beam bandwidth resulting in a decreased nonlinear efficiency. On the other hand, a real bandwidth of 0.3nm would give an efficient usage of the laser beam. However, on a shot-to-shot basis it gives larger fluctuations, since some of the laser shots fall outside of the acceptable crystal bandwidth. Therefore, it is advantageous to use LabView in order to provide the single shot measurement control. The data, the input-output detectors readings and camera pictures, were taken simultaneously allowing the "bad laser shots" data to be rejected during the post-measurement, manually accomplished, data processing. A primary reason for data rejection was a too low/high laser shot energy.
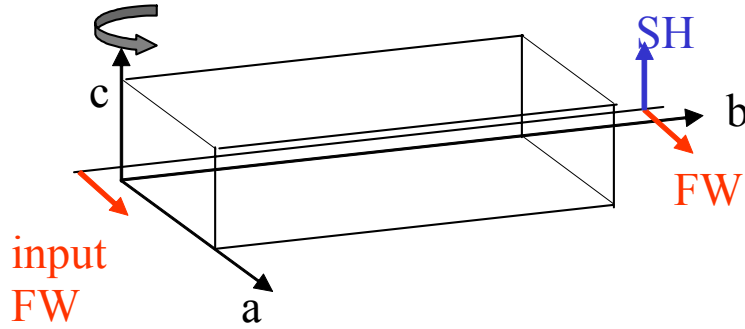
Figure 5.2: The schematic shows polarization direction of the incident wave (FW), the output waves polarizations (SH and FW) and the crystal axes *a*, *b* and *c*. *b* is the direction of propagation. The angle tuning was performed by rotating the crystal around *c* axis as indicated.

To determine the NCPM wavelength, a relatively wide FW beam was launched into the sample. In this way a plane wave configuration was mimicked which is the ideal case for the

43

angle tuning measurements. The dependence of the SH generation versus wavelength is measured. The process is based on the SHG functional dependence on the phase-mismatch induced by the wavelength variation. By assuming the low depletion limit for the conversion, one expects to observe a dependence similar to Figure 2.1(right). The experimentally measured curve is shown in Figure 5.3. The source bandwidth, the shot-to-shot energy oscillations and the non-plane wave incident beam slightly influenced the shape of the measured curve. This measurement gave a very good estimation for the phase-matching wavelength.
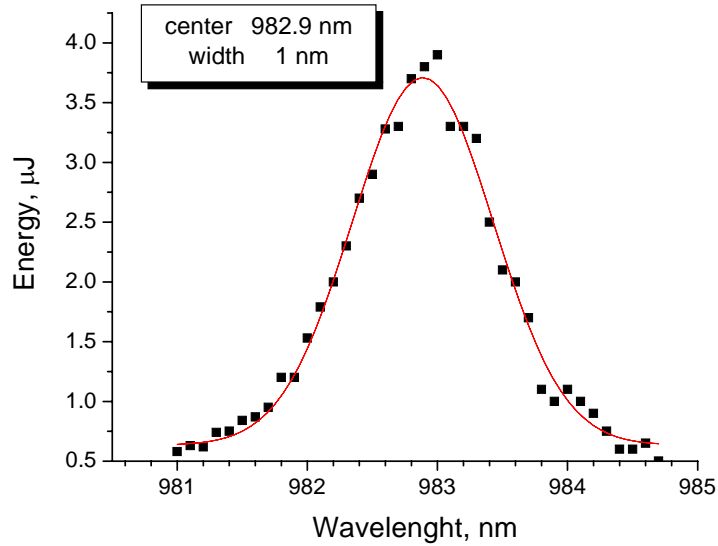
Figure 5.3**:** A measurement of SHG versus OPG-OPA output wavelength is shown. Squares are measured data and the red line is the fitting curve.

To determine the phase matching point even more accurately, SHG angle tuning measurements were performed. The crystal was rotated around its c-axis as shown in Figure 5.2.

For the NCPM case, just a single SHG peak was observed while for the off phase matching condition two peaks appeared symmetrically around the zero angle (Figure 5.4). The index of refraction curves for the FW and the SH are given at the source wavelength and illustrated in the insets. Once the wavelength is above the NCPM wavelength the SHG efficiency drops but still shows only a single peak SHG tuning curve. In this way, 983.7nm was estimated to be the NCPM wavelength. The large acceptance angle and the symmetry property of the parametric processes, caused by operating in vicinity of the NCPM, are expected to have an important influence on the soliton experiments. The measurements discussed in the following sections showed this very clearly.
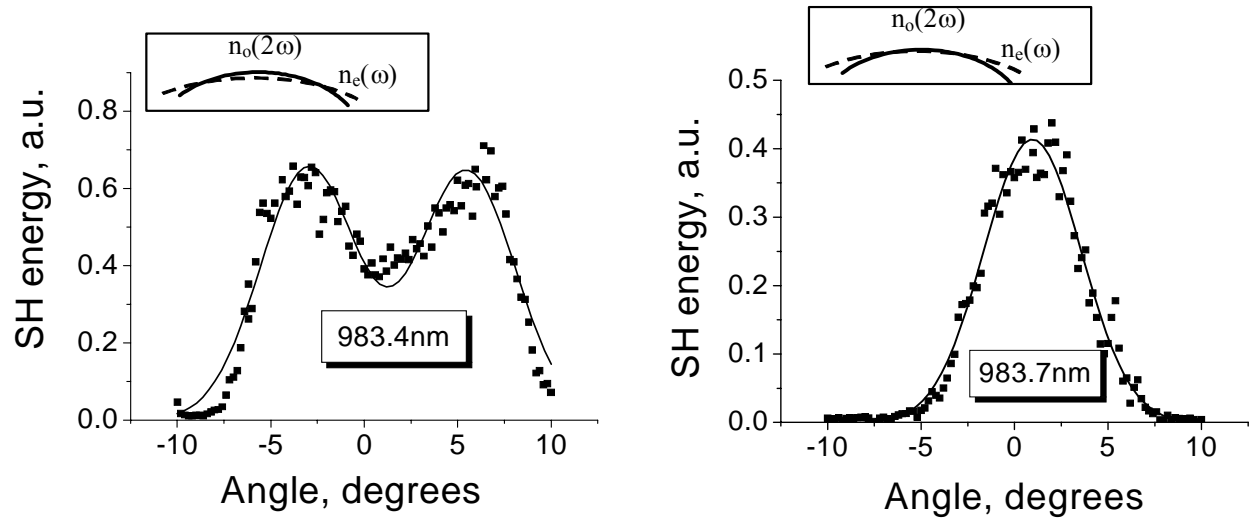
Figure 5.4: SHG angle tuning curves are shown for critically phase-matched (left) and NCPM (right) configuration. The lines are guides for eyes. The insets illustrate index of refraction curves for FW and SH. The intersection type (crossed for CPM and tangential for NCPM) is indicated.

5.4   KN soliton threshold measurements

Having defined all the necessary conditions for the efficient parametric processes, the next step was to launch the beam and to generate a soliton. The soliton generation typically starts with inputting the FW only. In the first few millimeters of the $KNbO_3$ sample, the SH was created from the input FW, as given by the parametric processes (2.9) and illustrated in Figure 4.2. After the several amplitude oscillations indicative of the energy exchange processes which occur within the first two diffraction lengths, a soliton is largely established.
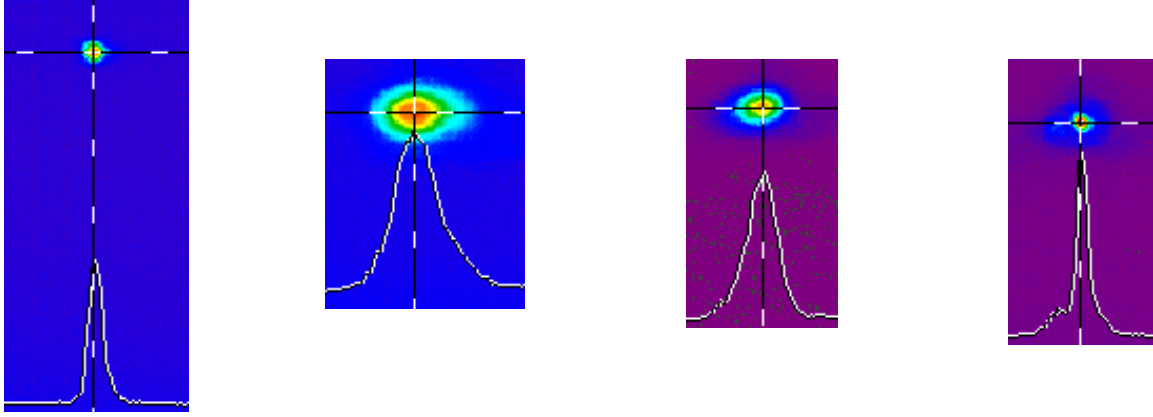
Figure 5.5: From left to right: input beam at the focus, diffracted beam in air, diffracted beam after propagation through the sample, soliton at the output of the crystal. Note the small asymmetry of the input beam.

A typical method for verifying soliton formation under the experimental conditions is to compare the input and the output beam sizes. Since approximately three diffraction lengths are required for the propagating beam to "stabilize" into a soliton, it is necessary to propagate the input beam for at least this distance to ensure soliton formation experimentally. The $KNbO_3$

sample used in the experiment was 11.4mm long which is equivalent to three diffraction lengths for an input beam of 22µm, and five diffraction lengths for a 16.5µm beam. By adjusting the input beam spot size the effective length for soliton propagation is determined accordingly. This is why most of the time the sample length in the literature is expressed in units of the diffraction length rather than the actual sample length.
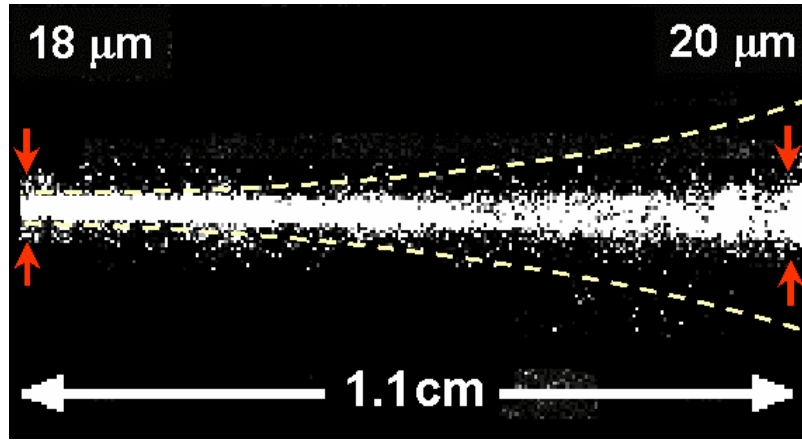
Figure 5.6: Top view picture of a soliton (picture taken by a CCD camera mounted above the $KNbO_3$ sample). The dashed curves show the expected beam diffraction.

Figure 5.5 shows a typical experimental outcome of a soliton generated after propagating through a three diffraction lengths long sample. As seen from the pictures the output beam is approximately the same size as the input beam. A top view picture of the soliton formation was taken by a sensitive CCD camera mounted above the sample (Figure 5.6). Unfortunately it was not possible to observe the beam completely free of the nonlinear effects (pure diffraction) because of the limited camera sensitivity. The observed pattern was caused by the spuriously scattered light. The CCD picture shows the soliton trajectory and the beam confinement. This

47

kind of observation required very special conditions: a) using a very sensitive CCD camera and b) very well controlled background light. Therefore, in the case of the periodically poled KTP (PPKTP) sample which will be introduced in detail in the following chapters, the top view measurements were not possible. This sample was phase-matchable at about 10 degrees centigrade above room temperature which required operation inside an oven and small thickness (0.5mm) of the PPKTP sample resulted in too much scattered light from the oven's inner surface located right under the PPKTP sample.
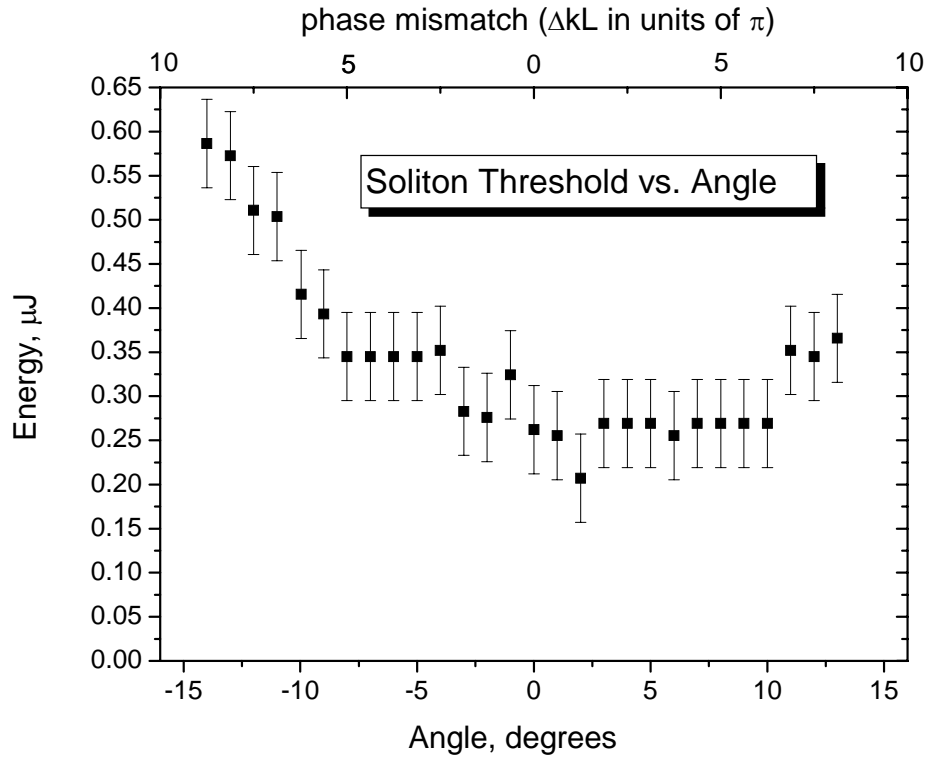
Figure 5.7: Soliton threshold pulse energy versus the rotation angle of the crystal around the c-axis (6^0 in angle corresponds to a 3.5π phase mismatch)

Once the imaging camera was calibrated to give a good estimate of the beam size, it was used to determine the soliton threshold versus the rotation angle of the crystal, see Figure 5.7. The Gaussian-shaped FW was focused down to a 22μm spot on the input crystal surface (resulting in three diffraction lengths for the soliton propagation). The minimum threshold was measured to be ≈0.27μJ which corresponds to ≈3GW/cm^2 for a 22ps pulse and the given beam waist. This threshold is the lowest one reported to date for birefringent phase-matching, and is a direct consequence of the high value for d_{eff}. This is comparable to the value for quasi-phase-matched LiNbO$_3$ for which the soliton threshold value was reported to be as low as 1GW/cm^2 [5].
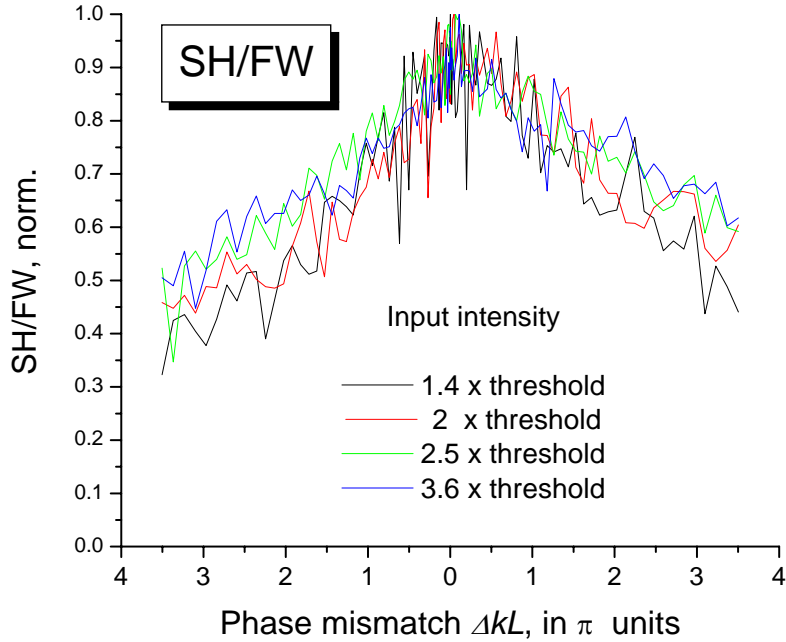
Figure 5.8: Normalized ratio of SH/FW output intensity versus phase mismatch for different input beam intensities.

The dependence of the soliton threshold on the external incidence angle is shown in Figure 5.7. The crystal was rotated around its c-axis which corresponds to rotation of the FW wave-vector in the b-a plane. The parametric processes have an enhanced bandwidth near NCPM and this was also expected in the soliton case. Here one can see that the soliton threshold increases slowly with the rotation and it is approximately uniform over a wide range of the incidence angles ($\approx 14^0$). The small asymmetry in the threshold curve about zero incidence angle is due to the $\pm 1^0$ uncertainty in the crystal cut and a small error in the crystal positioning (1-2^0).
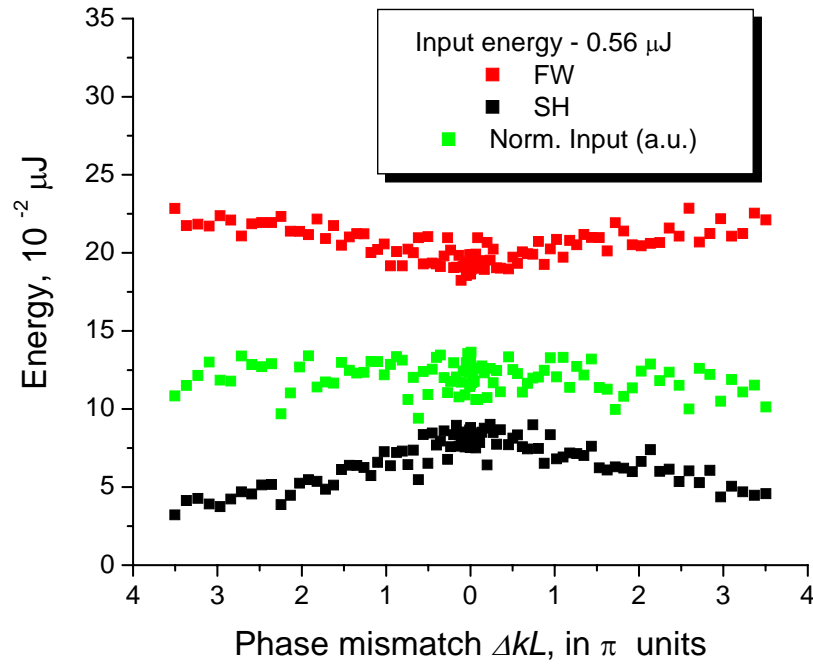
Figure 5.9: Dependence of the soliton content on phase mismatch.

The spectral content (FW versus SH) of the generated solitons was measured also. The ratio SHG/FW changes by a factor of two going from 0 to 3.5π mismatch, but it stays almost constant when the input intensity increases from 1.4 to 3.6 times the single soliton threshold.

The measurements done on the threshold and the spectral content of a single soliton around NCPM provide an excellent insight into the angular sensitivity of the soliton properties and are a good starting point for further research on multi-soliton generation and soliton collisions. Also, these measurements showed all the advantages provided by operating in vicinity of the NCPM. Later measurements on the PPKTP samples showed that the concept is generic.

During the generation of the first KN solitons, under the conditions described earlier, mutisoliton generation was also observed. In fact it turned out to be "a problem" to generate a single soliton for intensities high above threshold. Hypothetically, if one considers the simplest possible scenario for which the input FW beam is cylindrically symmetric and the diffraction is assumed to be equal in both transverse beam directions, any increase in the input power should lead to a monotonic narrowing of the generated soliton. In fact, if two-photon-absorption (TPA) is not a dominant effect, the narrowing is the only effect expected to occur.

In the experiments performed on the $KNbO_3$ sample, increasing the input FW energy resulted in the creation of the multiple solitons. The first set of the measurements, just an extension of the single soliton threshold measurements, showed a multi-soliton alignment along the crystal a-axis (horizontal alignment) [6]. The more detailed discussion is given in the following section.

5.5 Multi-soliton generation in KN

5.5.1 *Physics of multi-soliton generation*
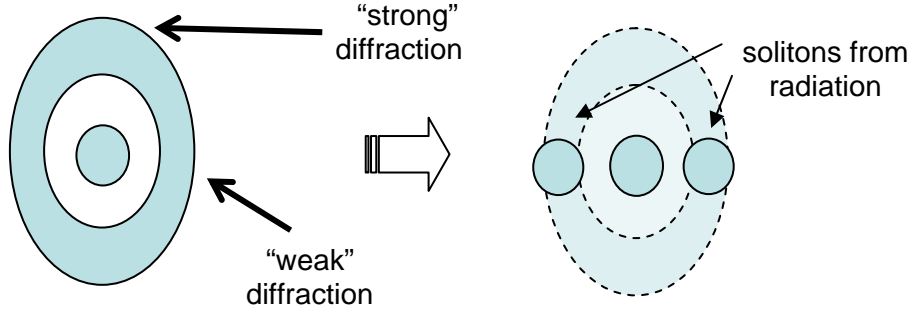
Figure 5.10: Illustration of a multi-soliton generation scenario. Increased input beam intensity results in larger amount of light emitted into a radiation "ring". Regions with higher intensities eventually lead to a collapse of parts of the ring into new solitons.

Historically multiple soliton generation was observed for the first time in a KN soliton generation experiment [6] while trying to excite high intensity single solitons. The input beam profile was nearly round and at that time multi-soliton generation had not been considered at all as a possibility. The unusual nature of this effect inspired several detailed theoretical and experimental studies [7, 8, 9, 10, 11]. Some of these aspects are discussed in this chapter.

Since at the time of the discovery of multi-soliton generation the beam shape (beam profile symmetry) was not considered to be an issue (namely, the beam was spatially filtered), the cause of the multi-soliton generation was assumed to be due to anisotropic diffraction [7].

For perfectly round input beams, multi-soliton generation is due to a combination of the different diffraction coefficients (i.e. along the a- and c-axes) associated with the propagation of radiation in an anisotropic crystal, and the generation of solitons by the inputting of the fundamental field only instead of the steady state soliton solution which consists of in-phase FW and SH fields at a specific amplitude ratio. Because the input is not matched to a steady state soliton, excess radiation is emitted in the form of rings as the required SH is generated and phase alignment takes place between the FW and SH. The resulting oscillations in the FW and SH intensity associated with this evolution process were shown previously in chapter 4, Figure 4.2. This radiation is emitted in the form of elliptical rings due to the anisotropic diffraction in the crystal. This concept is illustrated in Figure 5.10. Increases in the input beam intensity result in more radiation, mainly concentrated in a series of radiation rings, typically with one slowly diffracting ring carrying most of the emitted energy. As shown by Polyakov et. al. [7] the symmetry of the radiation ring from circular to elliptical is broken by the optical anisotropy (birefringence) of the material. Furthermore, if the incident beam itself is not circular but exhibits ellipticity, the resulting radiation ring becomes elliptical from this effect alone, for example in an optically isotropic medium. In an optically anisotropic material, this incident beam ellipticity can either enforce the ellipticity due to anisotropic diffraction, or tend to cancel it. This interference effect of course depends on the orientation of the incident beam ellipticity relative to the anisotropic diffraction. Since the symmetry in either case or a combination of the two is broken, it causes the formation of a higher intensity region in the ring which can potentially lead to the generation of additional solitons, as indicated in Figure 5.10. Note that the collapse of high intensity regions in the rings into additional solitons occurs due to the same physics that was described for single

53

soliton generation in Chapter 4. Again there is a trade-off between diffraction and beam collapse and sufficiently high intensity is needed in the ring to overcome diffraction. Because diffraction is the slowest along the minor axis of the ellipse, it is along this axis that the solitons preferentially form.

Expressed in mathematical form the phenomenon is given as

$$\frac{\partial}{\partial z}E_{FW}(z) - i\left(D_{11}\frac{\partial^2}{\partial x^2} + D_{12}\frac{\partial^2}{\partial y^2}\right)E_{FW}(z) = i\Gamma E_{SH}(z)E_{FW}^*(z)\exp(-i\Delta kz)$$

$$\frac{\partial}{\partial z}E_{SH}(z) - \frac{i}{2}\left(D_{21}\frac{\partial^2}{\partial x^2} + D_{22}\frac{\partial^2}{\partial y^2}\right)E_{SH}(z) = i\Gamma E_{FW}^2(z)\exp(i\Delta kz).$$

(5.1)

Here $D_{i,j}$ are the coefficients associated with the diffraction parameters. For an isotropic case they are all equal and given with $1/(2k_F)$ where k_F is the propagation wavevector of the fundamental wave. The differences among the $D_{i,j}$ coefficients can be induced by i) incident beam ellipticity and/or ii) index anisotropy associated with the propagating beam wavevector directionality. As discussed above, depending on the experimental conditions, these two effects can compete or work together in order to support the multi-solitons. They already have equal influence for a beam with just 4% ellipticity, which is essentially an "unnoticeable" amount of ellipticity from an experimental point of view. In fact, the very detailed numerical calculations done for PPKTP [12] identified asymmetry in the beam shape as the dominant factor. Therefore, the beam ellipticity is most of the time the dominant effect. The numerical simulations showed a strong influence of the input beam shape on the multi-soliton generation, predicting dramatically changed output patterns even for only a few percent of ellipticity.

54

The first extensive numerical and experimental efforts on understanding the multi-solitons were concentrated on the PPKTP multi-solitons. As shown in the experiments and implied in the simulations, the multi-solitons have a tendency to align along a preferred axis in PPKTP [7, 8, 9]. Figure 5.10 was found to explain very well this phenomenon.

5.5.2 *Experimental observation of multi-solitons*

First introduced experimentally, later investigated theoretically and then again experimentally, multi-soliton generation turned out to be a complex topic. After several iterations between the experiments and theory a thorough picture of the multi-soliton generation process have been obtained. The current status on multi-solitons, at least considering the quadratic nonlinearity, is given on the following pages.

Soliton number and patterning (orientation) were investigated over a wide range of input intensities (from 3 to 40GW/cm^2). Based on the numerical calculations the importance of the input beam shape has been identified [8]. Thus a spatial filter modification (the pinhole particularly) has been used in the experiments to gain control over the shape of the incident beam.

In the PPKTP system, investigated numerically and experimentally by Polyakov et. al. [9], the multi-solitons showed a very reproducible and regular behavior. The alignment strictly followed the beam asymmetry which was determined by the spatial filter alignment. When the input intensity exceeded a certain threshold, three well separated solitons were formed. A small jitter in their positions was observed at the sample output. Further input intensity increase

resulted in collapse back to one soliton generation. This soliton was sitting on significant background radiation ("bath" of radiation) which increased with further increases in the input beam intensity. The agreement between the experiment and the simulations was excellent in the PPKTP case.

If the system asymmetry (input beam ellipticity or diffraction anisotropy) is not considered with the intensity increase only one soliton, with progressively smaller width, is generated. Different from Kerr case which does not support soliton formation in (2+1)D systems (a self-focusing occurs for too high and a beam broadening for too low intensity), the quadratic nonlinear systems effectively behave as saturable nonlinear systems, therefore resulting in a soliton formation rather than self-focusing at high intensities.

5.5.2.1   Number of solitons versus input intensity in KN

In order to investigate the multi-soliton phenomena experimentally, two different input beam configurations, an elliptical and a cylindrically-symmetric beam (ellipticity measured to be less than 5%), were initially used. The results of experiments are shown in Figure 5.11 and Figure 5.12. In Figure 5.11 a "highly" elliptical beam was used while in Figure 5.12 a round, cylindrically -symmetric input beam was used. The input beams shown in the figures are the collimated beams at the output from the spatial filter. The intensity dependent output pattern was investigated.

one soliton
(two starts at 0.45μJ)

90% two

≥50% one; 20% two
20% blurred spot
(only 1 at 2 μJ)

input beam

input 0.3μJ

input 0.83 μJ

input 1.23μJ

≥60% two and three
(from 2 to 3 μJ)

40% one, 30% two
(from 3 to 3.3μJ)

three symmetric

input 2.2 μJ

input 3.1μJ

input 4.6μJ

input 4.7 μJ
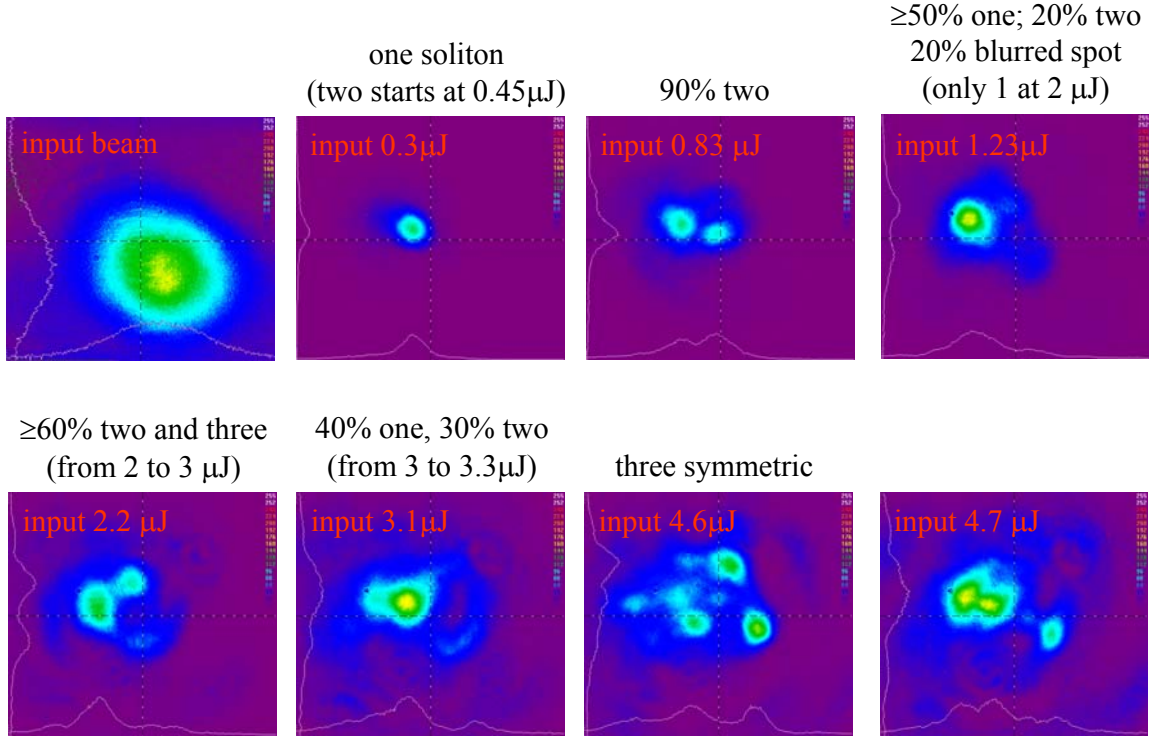
Figure 5.11: A collage of the output patterns is shown for the various input intensities. The input beam is "highly" elliptical. The additional captions above the pictures describe details of the statistical behavior of the output patterns.

As seen in the experiments, different input beam intensities result in dramatic output pattern changes and the patterns behave chaotically and vary dramatically from shot-to-shot. Note that the pulse energy varies by 10% from shot-to-shot. Therefore, only the most dominant patterns are shown in the figures. The caption above each camera picture indicates the statistical character of the behavior. At around $3GW/cm^2$ a single clean soliton is generated. Steady two soliton generation is obtained at slightly higher intensities (around $4.5GW/cm^2$ for the highly elliptical configuration and $5.5 \ GW/cm^2$ for the symmetric one). Further intensity increase results in higher background radiation not captured by the soliton-like beams. Despite the high

transverse mobility of the solitons which are sitting on the top of the background radiation, in some intensity regimes the tendency of returning to a single soliton realization is clearly visible. If the intensity is above $30GW/cm^2$, which is around 10 times the single soliton threshold, the output patterns show more variety. In the elliptical input beam case the diversity of the observed patterns is more obvious.
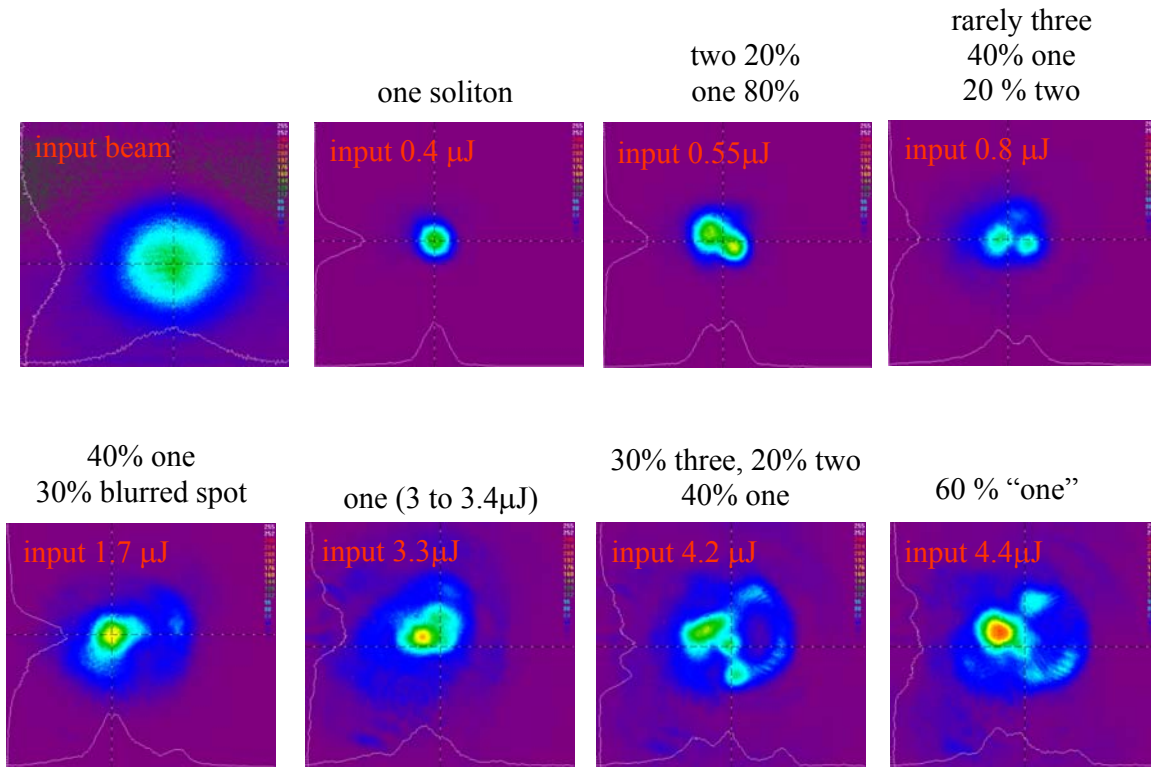
Figure 5.12: A collage of the output patterns at various intensities for a symmetric, round input beam. The captions above the pictures describe the statistical character of the "chaotic" output patterns behavior.

Therefore, the output patterns show similar behavior in both the elliptical and the round-symmetrical input beam configurations. The patterns vary in a similar fashion with input

intensity variations. However, only a statistical approach can be applied in characterizing and investigating the patterns, partially due to the instabilities of OPG-OPA output.

In order to understand better the multi-soliton generation features just discussed, CW 2D numerical calculations (results given in Figure 5.13(top)) were performed for symmetric input beams in anisotropic KN. The main effort was concentrated on determining the number of the generated solitons versus input intensity for the experimentally defined parameters. Also, the calculations were simplified by assuming anisotropic diffraction to be the only break-up mechanism. (Detailed discussion in reference [9] shows that the anisotropic diffraction and beam ellipticity mechanisms are mathematically almost equivalent.)

The Figure 5.13(top) shows the run-off angles versus input intensity. Here the run-off angle corresponds to the propagation angle of the additional solitons relative to the original, central soliton. The solitons have a tendency to separate faster for larger run-off angles. Starting from low input intensities, the first threshold is the one that generates the single soliton. At higher input intensities, first two and then three solitons are generated. Finally, with the further increase, the number of solitons decreases back to one.

It is important to know that the additional solitons are generated in phase with one another. Therefore their attractive forces increase as their intensities increase. Furthermore, the higher the intensity, the closer to the propagation axis the extra solitons form, as seen from the simulations. Both factors eventually lead to a collapse of the additional solitons resulting in single soliton generation again.

In a similar fashion to that for PPKTP, the simulations give aligned multi-solitons, but always aligned along the crystal axes. Although in most experiments it is the beam ellipticity that

59

governs the alignment direction, the evolution of soliton number with increasing input intensity predicted for dominant anisotropic diffraction is still valid.
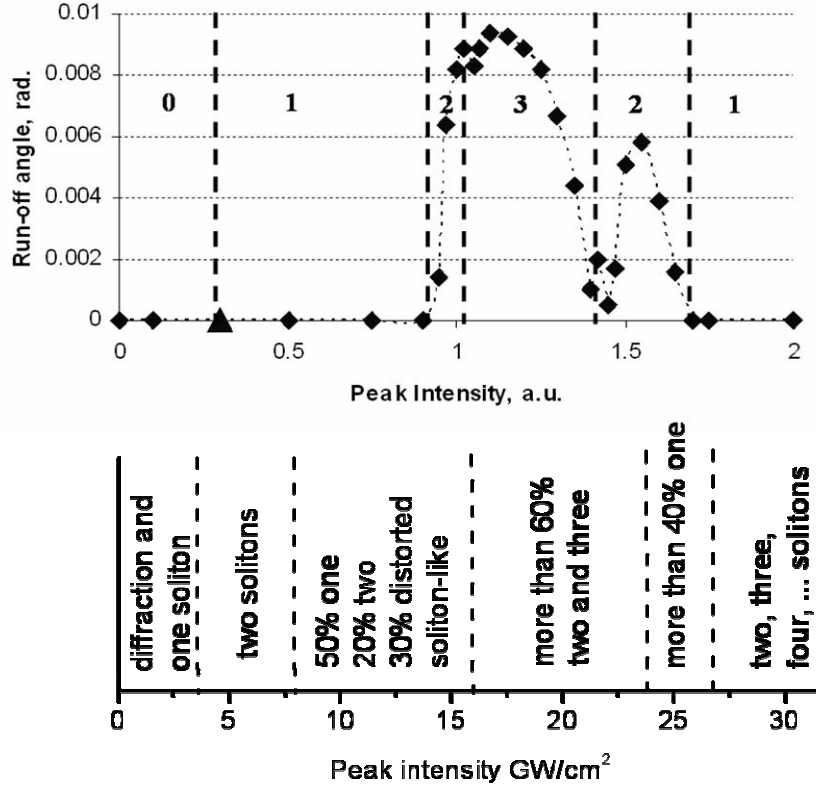
Figure 5.13: CW, 2D numerical calculations (upper) and pulsed experimental data (lower) for the number of solitons generated versus input FW beam intensity. Note the statistical character of the experimental data.

A slightly asymmetric beam was used in order to experimentally investigate the effect of an elliptical input beam alone. A number of the output pattern outcomes were recorded and statistically processed which finally resulted in the Figure 5.13(lower) graph. Following the input

60

beam intensity increase, first a single soliton was observed. At higher input intensities two solitons appeared, initially aligned along the preferred direction determined by the small amount of the input beam asymmetry.

a)

b)
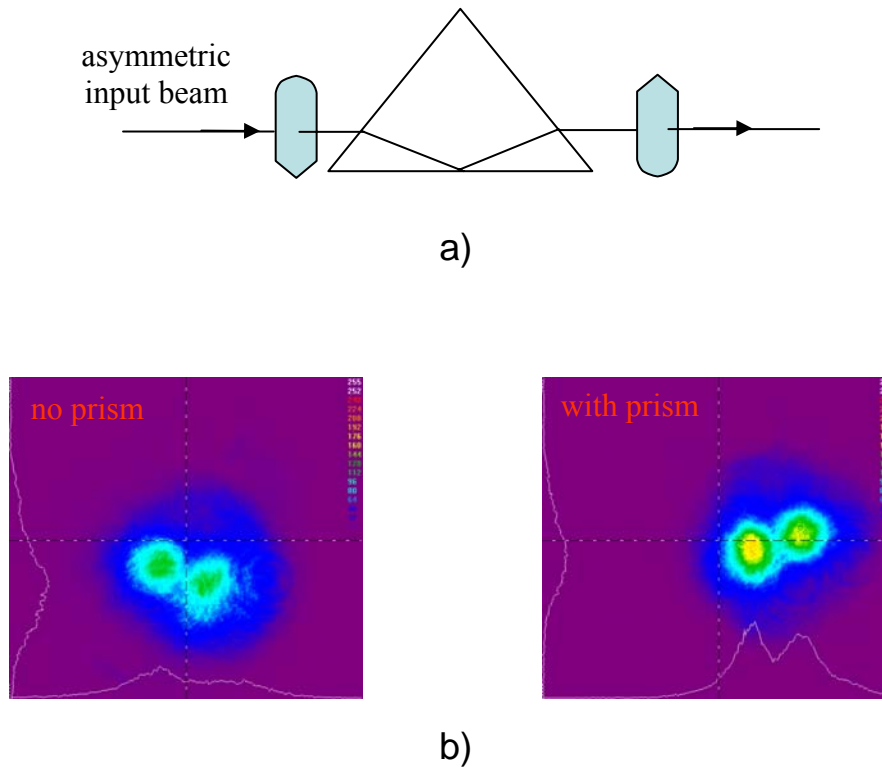
Figure 5.14: a) Schematic showing the Poro prism whose role is invert any input asymmetry in the input beam. b) Output from the KN sample for conditions in which two solitons are generated both without (left) and with (right) inverted beam asymmetry created by the Poro prism shown in a).

The two solitons preferred orientation was verified by introducing a Poro prism (right angle prism) into the incident beam line shown in Figure 5.1. The prism affects the beam symmetry, as illustrated in Figure 5.14a. Due to a single reflection on the prism's longer surface

the prism effectively inverts the symmetry of the incident beam. However, the beam directionality remains untouched. Since the beam is well collimated the prism does not introduce any aberrations or the beam size changes.

In Figure 5.14b the outputs from the KN sample are shown with and without the prism in place, respectively. The input intensity conditions were adjusted to satisfy two soliton generation. The output patterns are obviously the mirror images. Therefore the output multi-soliton pattern orientation is determined by the input beam asymmetry. With further intensity increase (above $7GW/cm^2$), the two generated solitons lost their preferred alignment direction.

Very dynamic and chaotic output patterns appeared around $15GW/cm^2$. The soliton-like spots were no longer nicely shaped and the number of the spots was different from shot-to-shot, ranging from one to three. Therefore, the experiment gave just a rough statistical agreement with the theory, reflecting only the tendency of the theoretical predictions on the soliton number. The main features were recognizable, but there were significant deviations. Clearly some other effects beyond anisotropic diffraction and just elliptical input beams are important for the multi-soliton dynamics and behavior in KN at the high intensities.

5.5.2.2   Noise effects on the multi-soliton patterning

Since the multi-soliton output patterns in KN varied from shot-to-shot and the OPG-OPA is well-known as a spatially and temporally noisy light source, more details of the influence of noise on multi-soliton generation were investigated. The intention was to estimate how

dramatically the output patterns can change under some nominally fixed conditions. To estimate the importance of the laser source's noise alone, the incident beam was intentionally made slightly elliptical. In this case an efficient multi-soliton generation was achieved. It was dominated by the beam ellipticity and away from the unstable, almost symmetric input beam condition.
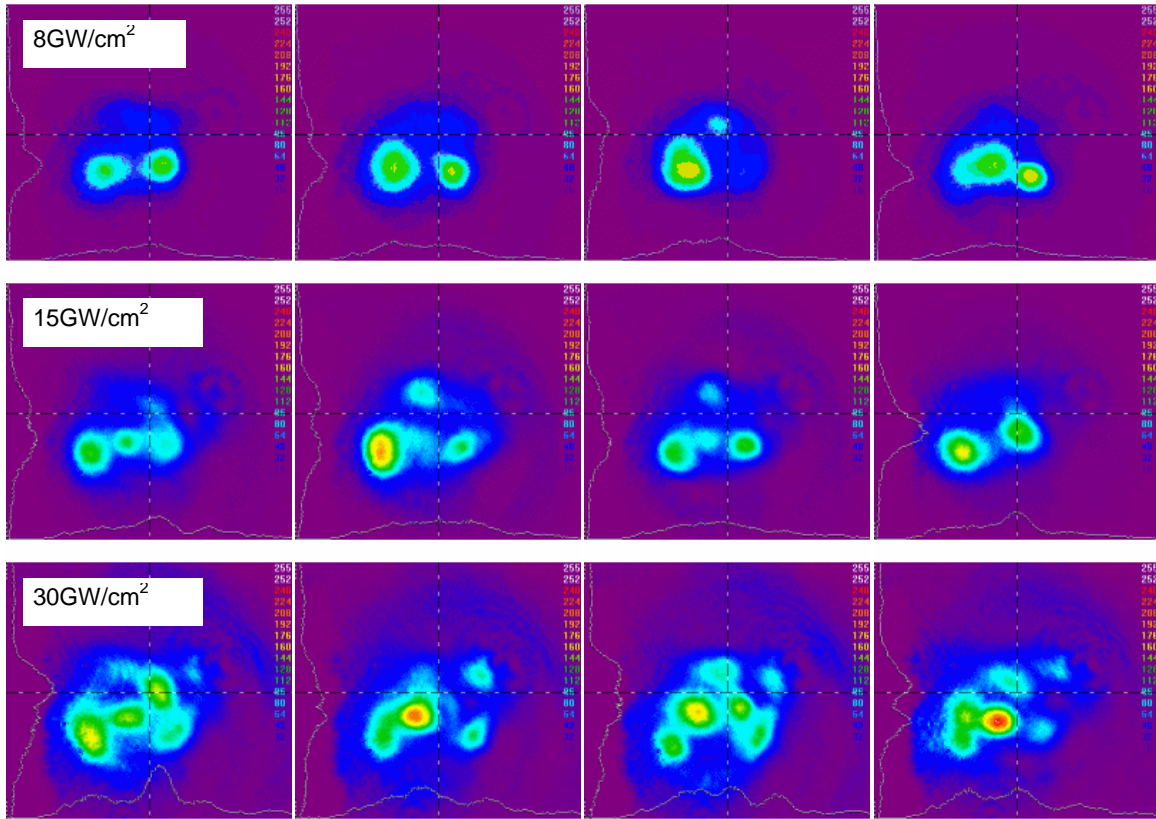
Figure 5.15: Three collages of output beam patterns obtained for peak input fundamental beam intensities of 8 GW/cm^2, 15 GW/cm^2 and 30 GW/cm^2. Successive frames correspond to successive laser pulses at nominally (to within the laser shot-to-shot energy uncertainty) the same peak input intensity.

For the given configuration (i.e., a beam waist of ~18μm), the single soliton threshold is about 2.7 GW/cm^2 [6] and multi-soliton generation first appears with two soliton generation at ~5GW/cm^2. Notice that the output multi-soliton patterns, shown in Figure 5.15, consist of irregularly shaped beams. Apparently for such a complex situation where several beams exist at the same time with the potential to interact, collide and merge, the 1 cm crystal was not long enough to allow all of the beams to completely evolve into solitons.
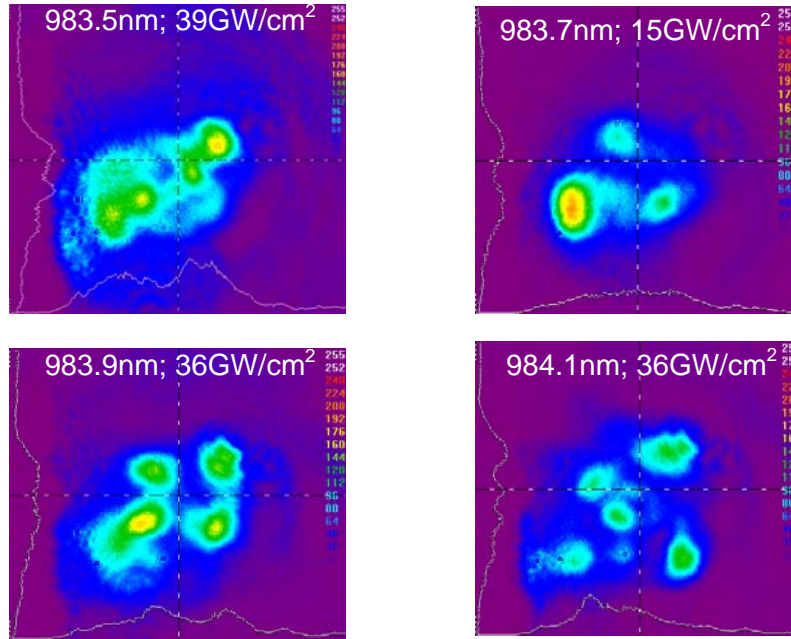
Figure 5.16: High power output patterns corresponding to nominally the same input beam shape are shown. The small difference in the FW wavelength just slightly influenced the phase-matching condition (OPG/OPA bandwidth is ~0.5nm).

Figure 5.15 shows the output patterns for three different intensities 8, 15 and 30 GW/cm^2. In each case there is a collage of the output patterns corresponding to successive laser pulses of nominally the same total energy. In Figure 5.15a (5 GW/cm^2 peak intensity input), the dominant pattern consists of two localized beams aligned horizontally. The generation of two well-defined light spots is clearly visible. With an intensity increase the pattern starts to change, becoming more chaotic. For the FW inputs of $\approx$15 GW/cm^2, i.e., 5 times the single soliton threshold, the output patterns are more complex, exhibiting 2-3 localized spots (Figure 5.15b). These high intensity beams are not aligned along a single line. They are sitting on a large intensity background. At even higher input intensities, of the order of 7-10 times the single soliton threshold (Figure 5.15c), the successive output patterns vary dramatically from shot-to-shot. The background is even more obvious. It has the ability to further destabilize the output pattern due to the increase in the solitons transverse mobility. Up to 5 non-collinear light spots are observed, however the most dominant pattern is the three beam configuration. Furthermore, the energy is usually concentrated in one of the soliton-like beams.

Figure 5.16 shows a variety of interesting patterns observed experimentally, and the conditions under which they were obtained. The input beam symmetry was nominally the same. However, the patterns were generated at slightly different FW wavelengths. Considering the OPG/OPA bandwidth of ~0.5nm the changes introduced by varying the FW wavelength are relatively small. In addition to changes in the phase mismatch (Δk>0 for λ>983.7nm), the OPG/OPA might produce slightly different "random" noise at the different wavelength settings which can seed some different output patterns. Notice the formation of the multi beam

configurations (up to 5 solitons) sitting on the high intensity background. Typically, as seen from Figure 5.15, in a multiple output beam situation one beam gains more total intensity than the others perhaps due to the multi beam interactions during the propagation through the 11mm sample. However, as shown here in Figure 5.16, multi-soliton outputs with quite uniformly distributed intensities over the beams are also possible.

Also, it is important to point out that with increasing input intensity, the differences between the successive output patterns increased. That is an indication for spatio-temporal nonlinear dynamics mediated by both the spatial noise imprinted on the beam profiles and the temporal noise imprinted on the pulses. Minardi et. al. recently have shown that the spatio-temporal dynamics generated in high power up- and down-conversion processes can lead to pulse break-up in time [13]. On the other hand, the high peak-power is associated with soliton and multi-soliton formation in the spatial domain. Combined together the temporal and the spatial dynamics result in spatio-temporal effects that might be responsible for the observations in the KN multi-soliton experiments. It is noteworthy that the multi-solitons generated in a PPKTP show the numerically expected behavior. Neglecting the differences between the PPKTP and the KN crystal systems, the major difference in the multi-soliton generation is in the light sources (1064nm laser light used in the PPKTP experiment and 983nm OPG-OPA beam in the KN experiment). Since the OPG-OPA output has at least an order of magnitude higher noise than the laser, it is reasonable to associate the KN multi-soliton behavior with the OPG-OPA noise.

The FDTD simulations performed (Figure 5.17) show the output intensity distributions corresponding to a high power input beam after propagation though a quadratically nonlinear medium. A small amount of noise was added on the top of the input Gaussian shaped pulse in

66

both spatial and temporal domain. The x-t cut, given in Figure 5.17a, shows the realization of a combined temporal and spatial beam break up. A "virtual camera" positioned at the end of the sample integrates the signal in time, due to the camera response time. The pattern seen by the camera is shown as the 3D and contour intensity plots in Figure 5.17b. The intensity distribution corresponds qualitatively to the experimentally observed multi-soliton features.
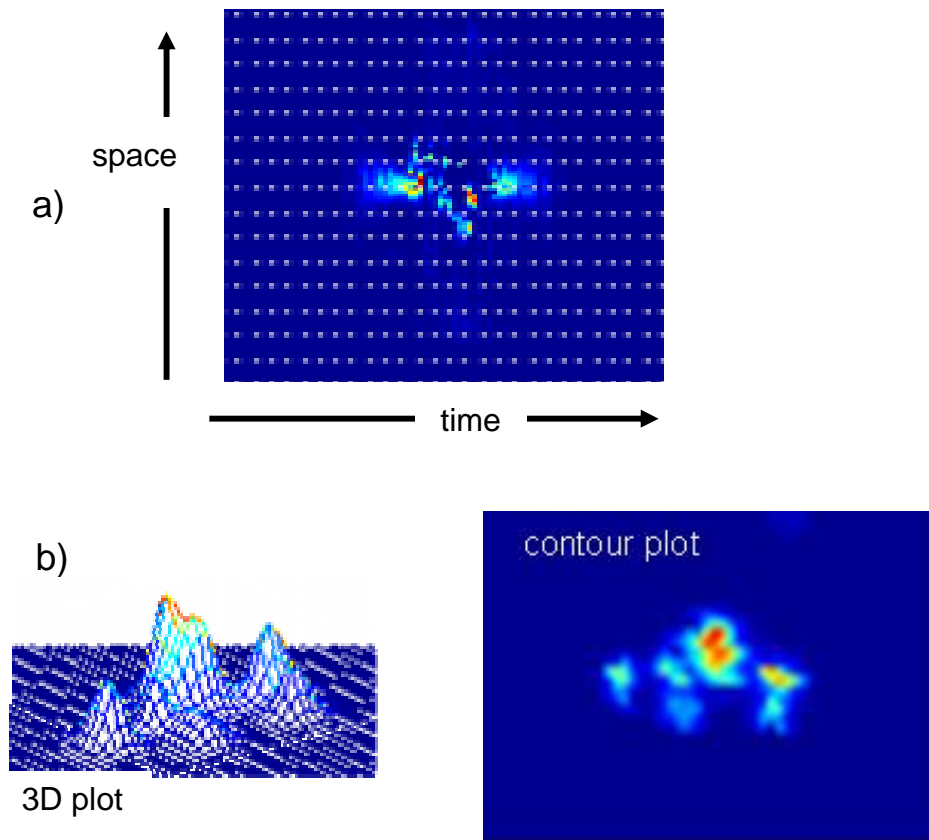
Figure 5.17: The FDTD simulations results show time-space dynamics of a laser pulse after propagation through a nonlinear medium. a) Shows intensity distribution of the pulse in a x-t cut. b) The output x-y cut intensity profile (averaged in time) is shown as a 3D plot and a contour plot. These correspond to the camera pictures.

67

In conclusion, quadratic nonlinear media support multi-soliton generation in the vicinity of NCPM at high input peak-powers. This was observed in the KN case just discussed. The output soliton patterns vary on shot-to-shot basis. The experimentally investigated properties just partially agree with the numerical simulation effects. The discrepancy is believed to be associated with the noise induced effects in the experiments performed.

CHAPTER SIX: QUADRATIC SOLITON SELF-REFLECTIONS IN PPKTP
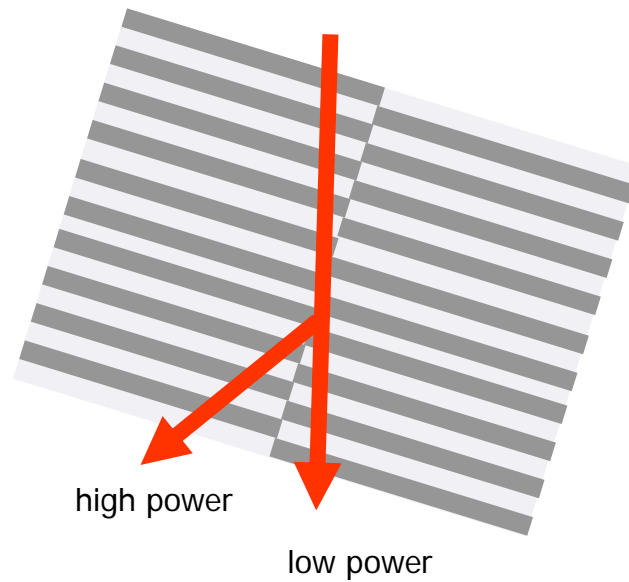
Figure 6.1: Illustration of a self-refraction. A high power beam is reflected and a low power transmitted.

In this chapter the details of the first observation of the quadratic soliton self-reflections are given. A specially engineered quadratically nonlinear sample was used in order to demonstrate this soliton feature. If a low power beam propagates through the engineered structure (Figure 6.1) it passes through the interface between the periodic structures, however a high power soliton can reflect under a certain incident angle and input intensity conditions. The process is called self-

reflection since the soliton beam itself is the cause for the reflection from the interface. More details are given bellow.

6.1   PPKTP sample properties

As introduced in Chapter 2, QPM is a common technique used to achieve phase matching at any desired wavelength. In order to perform a soliton self-reflection experiment a 7.5mm long periodically poled potassium titanyl phosphate (PPKTP) crystal was fabricated. The sample consists of two identical QPM gratings dislocated laterally for half a period, as shown in Figure 6.2. Even though QPM fabrication principles are well known, it was a challenging task to fabricate a sample with a double QPM structure which has a well defined boundary region between the QPM regions (Figure 6.2). The sample structure, as seen in the microscopic picture, is visible due to the etching procedure that was applied at the last stage of the fabrication. The channels in the structure are only one micron in depth and they do not influence the bulk sample properties.

In the fabrication process a relatively low coercive field of 3.8-4.0kV/mm was used during the low temperature poling to minimize the natural tendency of the poled lines to expand, allowing two very closely spaced (few microns separation) grating structures to be fabricated without merging [1, 2]. A nominal 9μm poling period along the crystal's a-axis gave a NCPM at 1064nm at a temperature of ~36^{0}C for propagation along the a-axis [1-3].
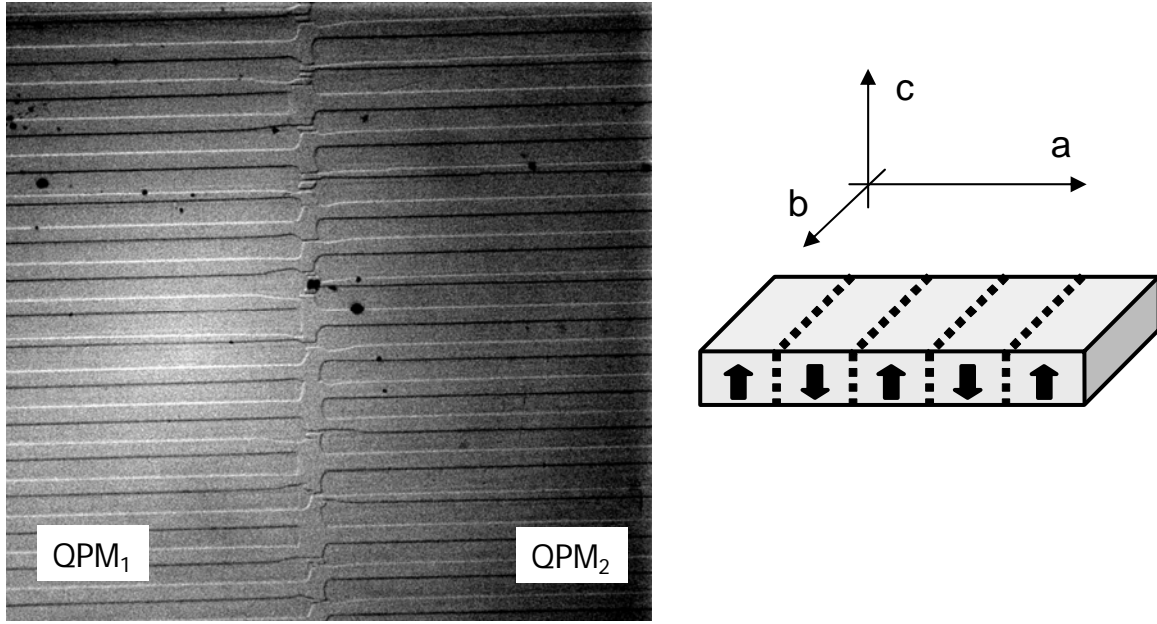
Figure 6.2: (left) PPKTP sample with a double QPM structure. The horizontal lines are the QPM domains. The vertical line is the interface between the two QPM regions. The thickness of the interface is 6μm. (right) a, b and c are the sample crystal axes.

In order to initially determine the NCPM temperature a 40μm wide beam was launched into the sample. This slowly diffracting beam, 60μm wide at the end of the sample, was launched through one QPM region only. The sample temperature was controlled by a LabView driven, home made oven with a limited temperature stability of around 0.1^0C. The 1064nm FW launched from a Nd:YAG laser was used to generate the SH in the low depletion limit. The SHG efficiency as a function of the sample temperature is shown in Figure 6.3. The SHG efficiency corresponds well to the theoretical sinc^2 dependence. However it does not reach zero at the first minimum since the FW beam is not a plane wave but rather a slowly diffracting beam with a distribution of wavevectors that contribute to the SHG. As the FW intensity increases the SHG

71

tuning curve broadens and becomes asymmetric. The intensity change is even more dramatic if a narrow input FW beam is used [4].
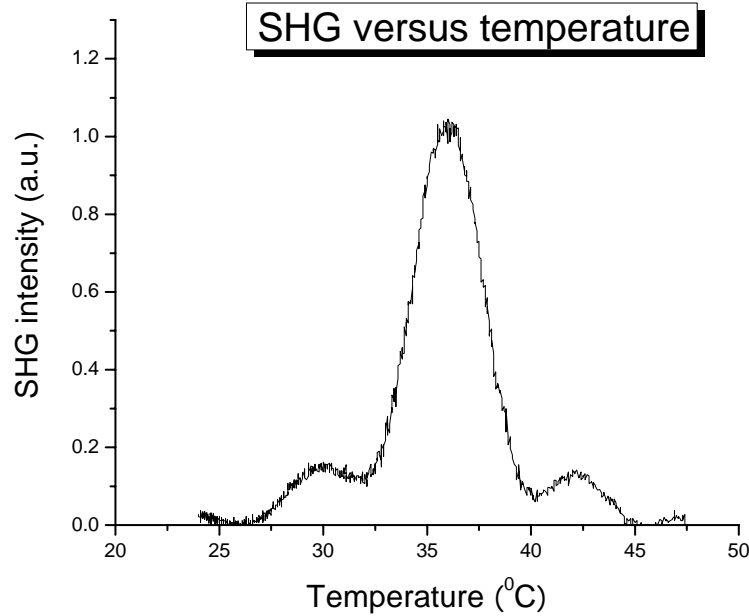
Figure 6.3: SHG intensity as a function of the sample temperature. A 40μm wide beam was used. The input FW intensity was kept low in order to satisfy the low depletion limit condition.

The mask used for the poling had a half period dislocation as shown above and the interface in the a-b plane was located approximately in the middle of the sample. The interface region extends laterally over approximately 3-6 micrometers.

The fabricated sample was a state-of-the-art sample. In fact, this sample was the only good one out of the total eight of samples fabricated in the similar way. The problems associated with the other samples were the surface polishing quality, broken QPM poling lines, thick interface

72

regions, low SHG efficiency, etc.. In fact, the longer the sample the more difficult it is to fabricate the desirable properties.

Total output as a function of the input
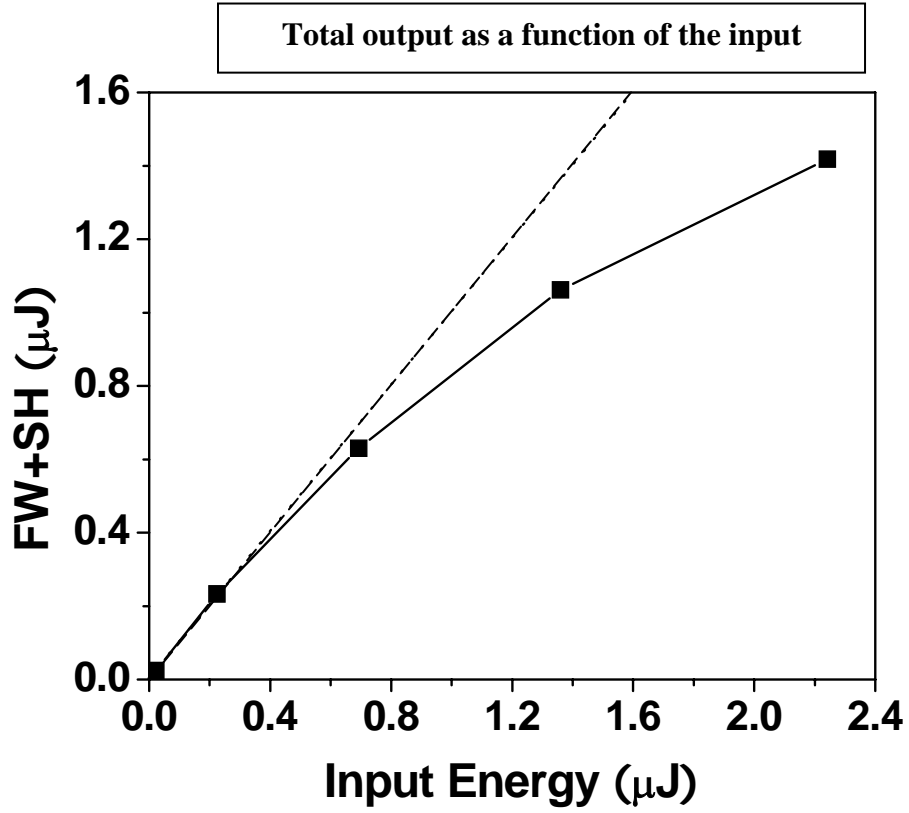
Figure 6.4: Total output pulse energy (FW+SH) dependence on the input FW pulse energy is shown for a focused beam (~18μm spot size).

PPKTP is an attractive medium for its large angular bandwidth for soliton generation which means that the solitons remain essentially the same for small changes in the incident angle. This aspect is similar to the previously discussed wide KN soliton threshold bandwidth which is believed to be a direct consequence of working in the vicinity of NCPM. In PPKTP the NCPM is

realized by using co-polarized FW and SH and in this particular experiment the polarization was set along the c-axis thus using the d_{33} nonlinear coefficient. Furthermore, the high PPKTP effective nonlinearity $d_{eff} = 2d_{33} / \pi = 9.5 \text{pm/V}$ (for a 50% poling duty cycle) allows soliton generation at intensities for which multi-photon absorption is low. In order to determine the effects of multi-photon absorption (particularly TPA) of the sample for a high intensity beam propagating through one of the QPM gratings, the total output energy was measured as a function of the input FW energy. A pyroelectric energy-meter, distinctive for its flat wavelength response, was used in the measurements. Figure 6.4 shows the measured dependence for the focused beam (18μm spot size), which was used in the soliton self-reflection experiment discussed in the following sections. The soliton energy regime used in these experiments was around 0.5-1 μJ/pulse ensuring that the multi-photon absorption effects were low, as seen in Figure 6.4.

6.2   Theoretical background

The basic optical phenomena of reflection and transmission at an interface between two media with different refractive indices are governed by the Fresnel laws. This feature is linear. Considering in addition nonlinear optics, the Kerr effect can perform an intensity modulation of the refractive index. Therefore, if two materials, with equal refractive indices but different Kerr properties form an interface, an intensity dependent reflection can occur [5]. The phenomenon does not follow the classical Fresnel reflection law [6]. However, the induced index change is relatively weak and can influence beam behavior only at a small incidence angle. In addition, the

materials forming the interface have to satisfy certain conditions on the nonlinear properties in order to show intensity-dependent effects.

A quadratic nonlinearity offers very different horizons in realizing intensity dependent reflection/transmission effects. The quadratic nonlinear properties can be modified by using the QPM technique, without introducing an index of refraction change.

The possibilities resulting from using multiple QPM structures, shown in Figure 6.5, have been introduced and theoretically investigated by Clausen and Torner [7]. The multiple QPM region strategy in fact offers different configurations, as discussed in [7] and illustrated in Figure 6.5.
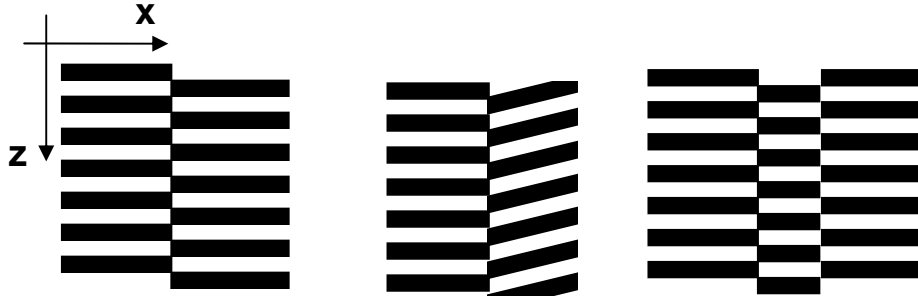
Figure 6.5: Schematics of multiple QPM structures. The structure on the left (dislocation configuration) corresponds to the sample used in this work.

Considering the dislocation case only, the two QPM gratings (the QPM basics were introduced in section 2.6.3), which are periodic along the z direction, modulate the nonlinearity as

$$d(z,x) = d[z - z_0(x)] = \sum d_n \exp(inq[z + z_0(x)])$$
$$\approx d_1 \exp(iq[z + z_0(x)])$$

(6.1)

where d(z,x) is the modulated material nonlinearity and q=π/Λ (Λ is the grating period). The

soliton sample structure, shown in Figure 6.2, uses the d_1 Fourier component, which equals

$2d_{33}/\pi$. Notice that the x direction dependence in (6.1) reflects the double QPM structure effect.

The SVEA equations (2.9) for the dislocation structure are given with

$$\frac{\partial}{\partial z} E_{FW}(z) - iD\nabla_T^2 E_{FW}(z) = i\Gamma E_{SH}(z)E_{FW}^*(z)\exp(-i\Delta kz)\exp[i\theta(x)]$$
$$\frac{\partial}{\partial z} E_{SH}(z) - \frac{i}{2}D\nabla_T^2 E_{SH}(z) = i\Gamma E_{FW}^2(z)\exp(i\Delta kz)\exp[-i\theta(x)].$$

(6.2)

Here $\theta = z_0\pi/\Lambda$ models the transverse direction effects, and for the actual sample, the

dislocation (z_0) is given by

$$z_0 = \begin{cases} 0 & \text{for } x \leq 0 \text{ (left QPM)} \\ \Lambda/2 & \text{for } x > 0 \text{ (right QPM)}. \end{cases}$$

(6.3)

Effectively introducing the dislocation results in an additional $\exp(\pm i\pi)$ phase in the coupled

equations (6.2) for $x > 0$. Naturally the beam propagating through only one QPM, the left or the

right one, does not see any additional effects since the additional phase can be "absorbed" by the

SH electric field, by substituting $E_{SH} \rightarrow E_{SH}\exp(-i\theta)$.

The numerical simulations, similar to [7], performed for a (1+1)D CW case by using a

BPM tool, show a very dramatic intensity dependence of the reflectivity. The reflection occurs at

the interface between the QPM structures. The simulation parameters corresponded to the

experimental conditions.
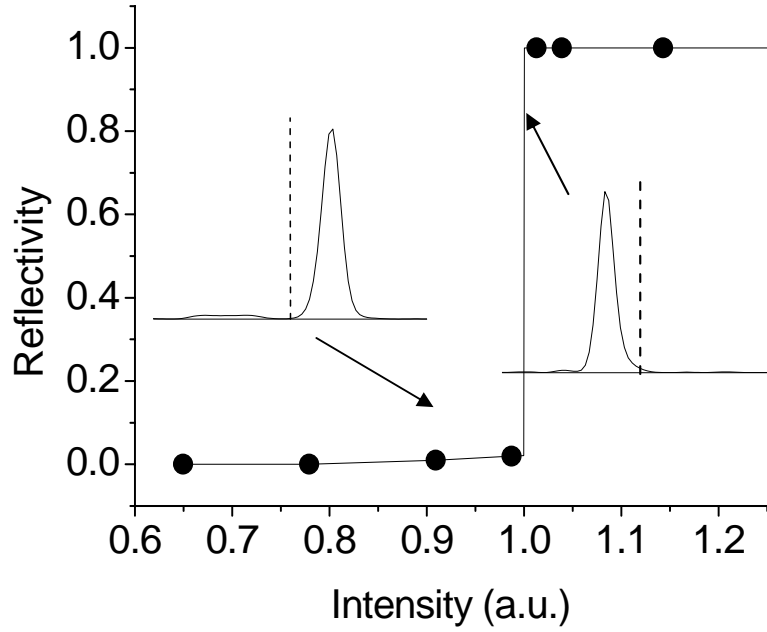
Figure 6.6: The (1+1)D CW numerical simulation results of the reflectivity versus the input intensity for the double QPM structure (dislocation) shown in Figure 6.2. The insets show the output beam profiles for the two limiting intensities. The dashed line indicates the position of the interface.

Figure 6.6 shows the numerical results. Here the reflectivity was calculated as a ratio of the reflected power to the total input power. The beam hits the boundary from its left side, according to the inset of Figure 6.6. Therefore on the left/right side of the boundary is the reflected/transmitted component of the beam. As seen on the graph the reflectivity is close to zero if the beam intensity is below a threshold and abruptly switches to one at the intensities over the threshold. Solitons behave as "particles" and always attempt to remain complete. From this point, the sharp change in the reflectivity is a direct consequence of the spatial soliton behavior and thus solitons are ideal candidates for all-optical switching applications.

77

This intriguing numerically predicted intensity-dependent reflectivity behavior is based on the already mentioned additional phase factor effect in the conversion equations, which affects the soliton passing through the interface. A well formed soliton has its SH and the FW components locked in phase and it has a certain intensity distribution, which is defined by the input conditions. By passing through the boundary, the soliton features (SH and FW phase, intensity distributions, etc.) get perturbed. The interface effect can be described mathematically as an effective repulsive potential well effect (for more details see ref. [7]).

The numerical simulations for the pulsed beam case are shown in Figure 6.7. The beam propagates from left to right and the interface is positioned as indicated in Figure 6.7a by the dashed line. A Gaussian intensity distribution is assumed for the pulses and the spatial beam profile corresponds to the experimental conditions. The peak intensity units correspond to the units used in Figure 6.6 for CW numerical simulations. The incidence angle to the interface is equal to the angle used in the experiment. At the 0.7 a.u. peak intensity (Figure 6.7a), the soliton, which is formed after propagation through the medium and before interacting with the interface, is completely transmitted and there is no deflection of the beam propagation direction. The beam starts to be influenced by the interface at 0.9 a.u. peak intensity, resulting in the beam profile changes at the output and a slight bending of the propagation direction toward the interface. However the beam is still efficiently transmitted.
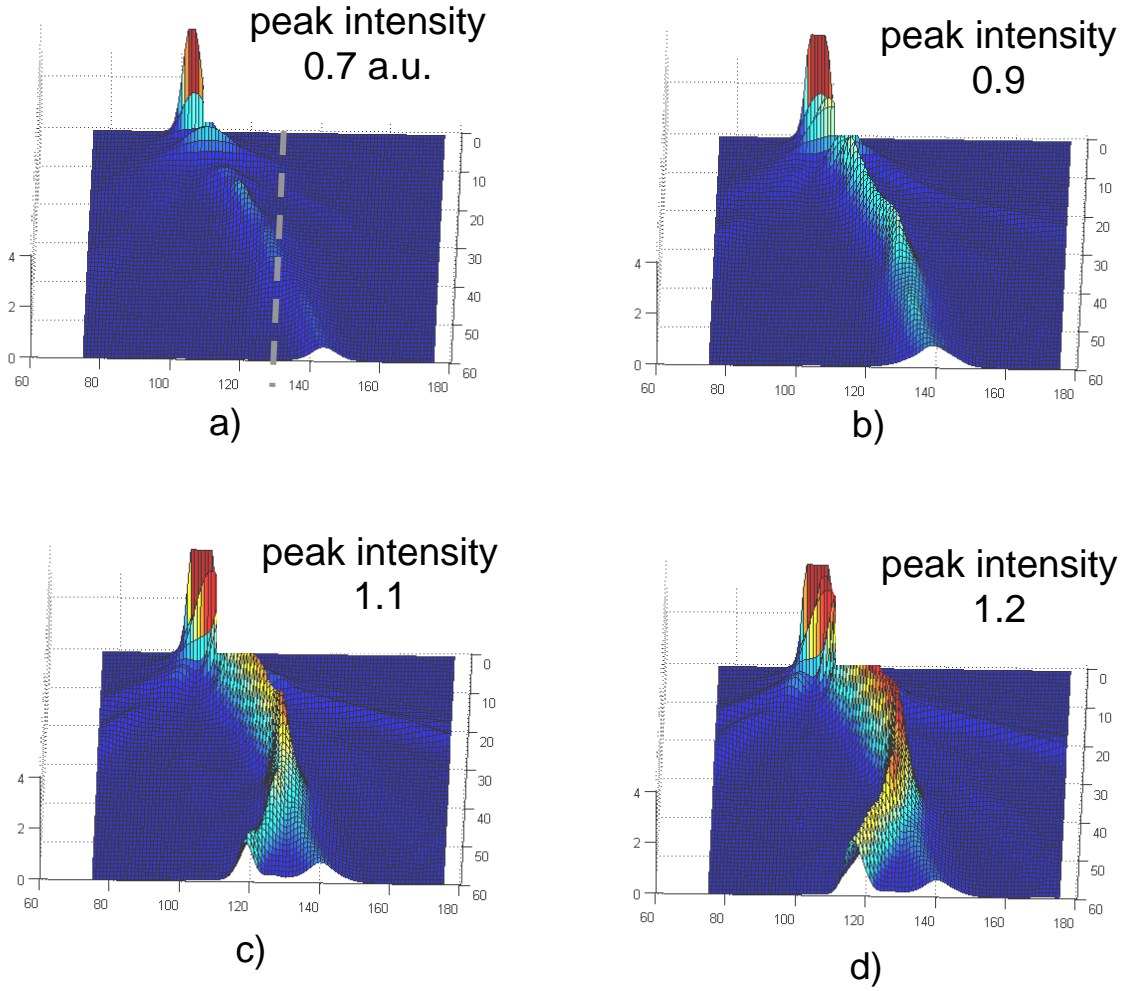
Figure 6.7: A (1+1)D numerical simulation of the FW beam component propagation through the dislocation configuration is shown. a,b,c & d correspond to increasing input intensities. Gaussian shaped pulses were assumed. The dashed line illustrates the interface position.

If the input intensity exceeds the CW reflection threshold, the beam breaks into a reflected and a transmitted part. With further intensity increase, the reflected portion of the beam increases. As can be seen from the above simulations, in its interaction with the interface the beam propagates along the interface for some time which indicates that the reflection occurs after

a certain beam-interface interaction length and not instantly. The partial reflections occur due to the pulsed nature of the beam, where the time profile undergoes a reflection process which depends on the position in the temporal profile, as illustrated in Figure 6.8.
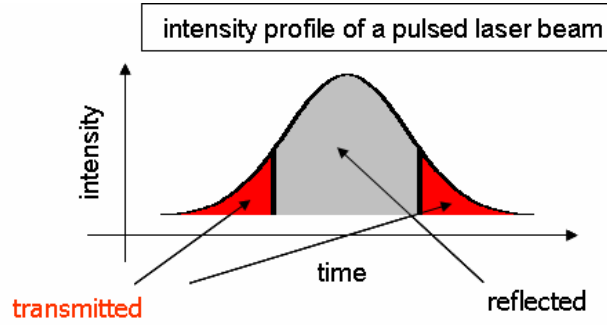
Figure 6.8: Illustration of an intensity profile of a light pulse in which the transmitted (low intensity) and reflected (high intensity) portions of the pulse are identified. The reflections occur in the beam-dislocation interface interaction process under appropriate conditions.

As a result of the pulsed nature and the partial reflections, the transition from complete transmission to an efficient reflection is a smooth function of intensity while in the CW case the change is very steep, as already discussed.

6.3   Experimental setup and measurement conditions

The 1064nm output from the EKSPLA laser was used as the light source in the experiment. The 1064 laser beam is the non-SHG-converted portion of the amplified laser output passed through a BBO SHG crystal. In order to decrease the M^2 laser beam quality factor from 1.8 to 1-1.1, where 1 means a perfectly Gaussian beam, it was necessary to use spatial filtering. The Si

detectors (1cm^2 area diodes) were used for the FW and the SH energy measurements. Due to the low repetition rate of the laser a BoxCar system, LabView driven, was implemented for the data acquisition purposes. The BoxCar has a variety of options allowing sophisticated detector signal gating, integrating and averaging procedures. However, the "floating" offset of the integrated signals and the poor long term stability of the BoxCar synchronization with the laser trigger signal are two major drawbacks. However, it is the best and the only commercially available tool for multi-detector data collection using low repetition laser systems.
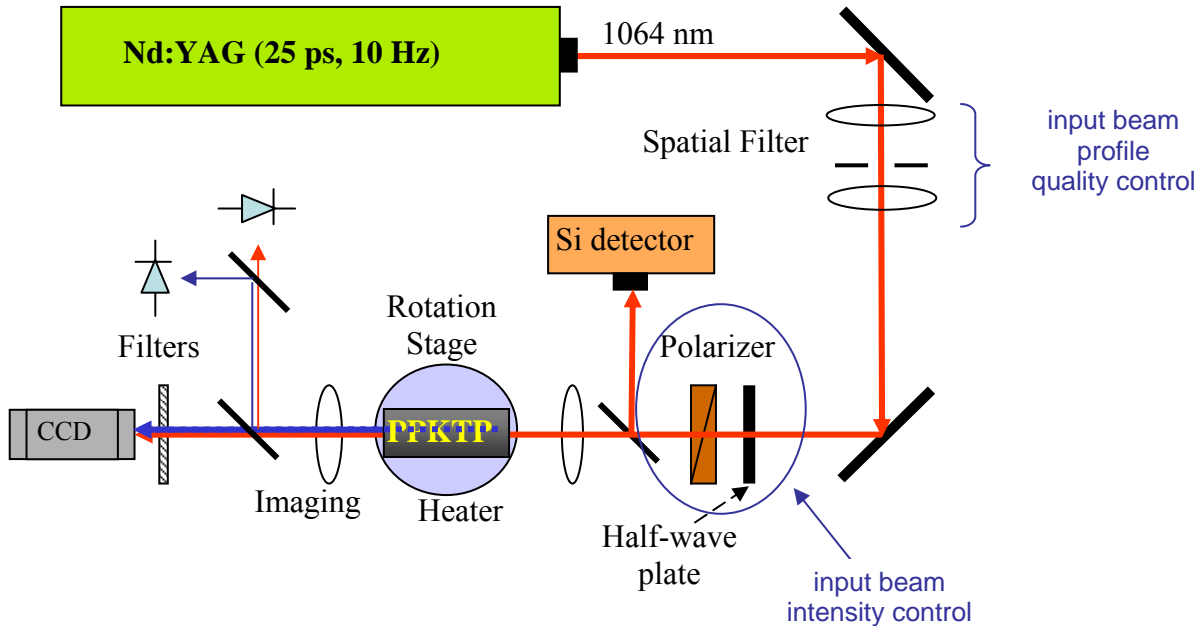
Figure 6.9: Schematic of the experimental setup.

After some beam shaping optics the 1064nm, 25 ps laser beam pulses were focused into the 7.5mm long PPKTP sample. The spot size was around 16μm and therefore the sample was

effectively more than five diffraction lengths long. Only the FW was launched and the SH was generated in the usual up-conversion process from the propagating FW beam component. By changing the sample temperature, which was controlled by a home made oven, it was possible to tune the phase matching conditions over approximately $\Delta kL = \pm 5\pi$ around the NCPM condition. The transverse sample position and the crystal orientation (angle) were controlled by the LabView driven 1μm precision translation and 0.01^0 precision rotation stages, allowing a precise control of the relative position between the beam and the interface. The beam was adjusted to hit the interface at around a 0.5^0 angle. By operating at a decreased sample temperature resulting in a 2.4π phase mismatch, the input beam was able to achieve the soliton state within a shorter propagation distance. Additionally, the phase mismatch suppressed the multi soliton generation effectively and made the soliton generation less sensitive to imperfections and irregularities in the QPM structures. The output from the sample was imaged on a Si CCD camera, which was computer-controlled and synchronized with the energy detectors.

6.4   Experimental results

In order to demonstrate experimentally the intensity-dependent reflections, the experimental setup from Figure 6.9 was used. The sample, precisely positioned with the motorized mico-positioners, was tilted at ~0.5^0, in this way determining the incidence beam angle onto the QPM interface plane. Initially, the successful generation of solitons in the two QPMs was verified by launching the laser beam separately into each single QPM region, far from the interface. The observed solitons were well formed at the output of the sample. The 2.4π phase mismatch was

used to generate solitons within a short propagation distance, to minimize the influence of the QPM imperfections and to decrease the probability of multi-soliton generation.
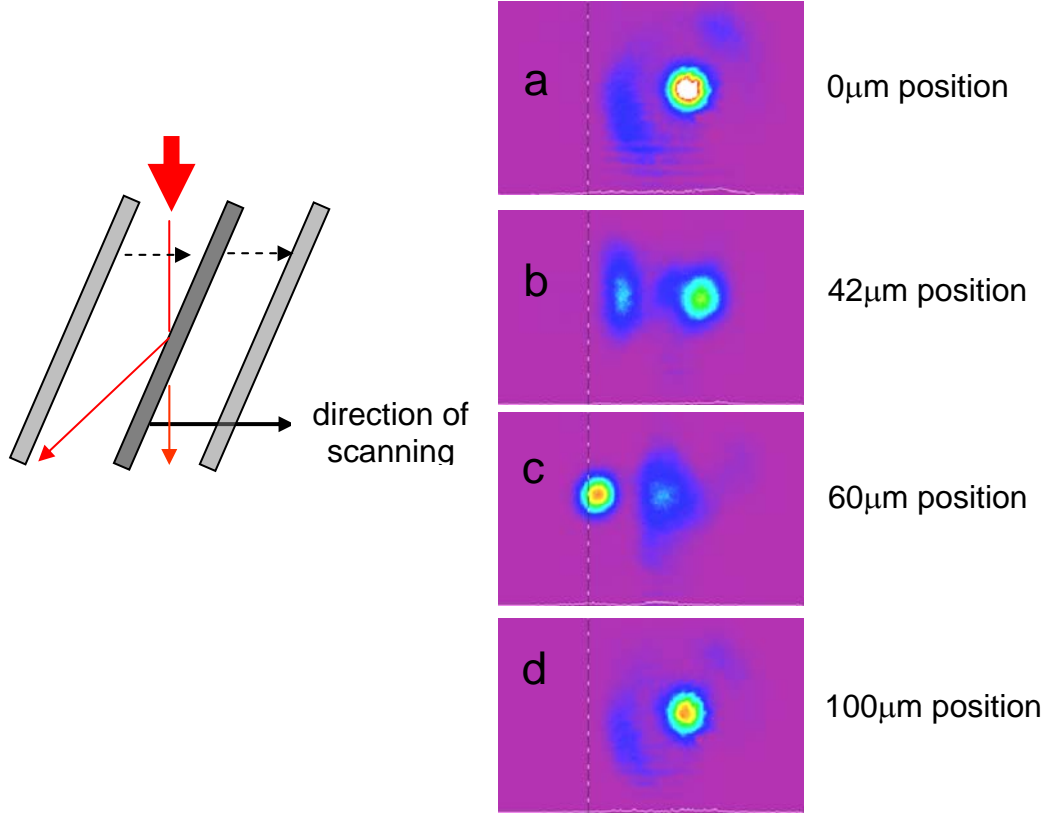
Figure 6.10: (right) Set of output patterns for an ~6GW/cm^2 input beam intensity for several different sample positions relative to the propagation beam. (left) The beam direction was fixed. The sample scanning direction from left to right is illustrated. Only the interface is shown.

The nonlinear reflections were found to occur at a 0.5^0 incidence angle at around 6GW/cm^2 input beam intensity. Figure 6.10 shows the output solitons for several different sample positions relative to the propagation beam. The beam's incident direction was kept fixed and the sample was moved perpendicularly to it by a motorized, LabView controlled micropositioner.

For the sample's initial position the beam propagated from the right of the interface and passed through one QPM region only. A soliton was formed (Figure 6.10a) and was observed at the output. As the sample was moved further for 42μm measurement, the beam started to interact with the interface. The observed output soliton was slightly deflected to the right. This could be understood as the beam's tendency to escape from the vicinity of the interface in order to keep its integrity and eventually form a soliton. At the 60μm sample position, the beam hits the interface after around 4mm of propagation through the 7.5mm long sample. The soliton is well formed after this propagation and it is efficiently reflected from the interface back to the same QPM region. The reflected beam output is separated by 80μm from the initial non-deflected output point. However on the transmitted side, a wide, weak beam is observed as well, indicating that the beam is also partially transmitted. This is in agreement with the theoretical simulations (Figure 6.7) for a pulsed beam. For intermediate sample positions, not shown here, the beam pattern is irregular and mainly diffracted. The deflection of the reflected beam decreases when the sample is moved further and at the 100μm position the beam goes entirely through the sample without interacting with the interface.

The measurements clearly show that the input beam has to propagate for several millimeters through the sample in order for the reflection to occur and obviously only solitons can reflect from the interface.
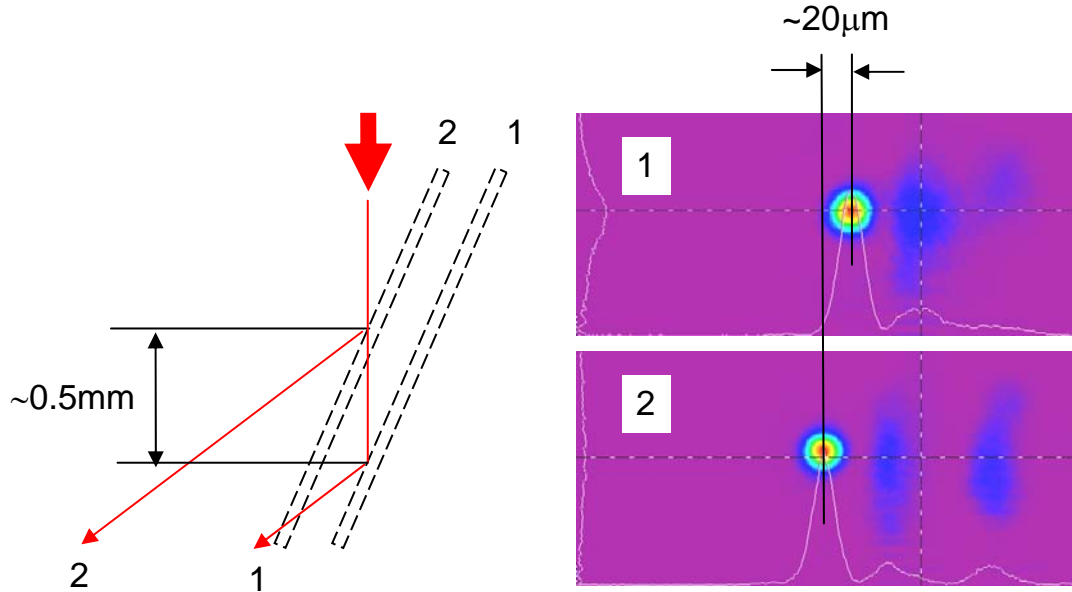
Figure 6.11: Soliton reflection for two sample positions separated by ~10μm. The beam direction was fixed.

In the experimental result shown in Figure 6.11, the sample was transversely shifted by around 10μm while the input beam direction was kept the same. Therefore the high intensity, well formed solitons (~6GW/cm^2) hit the interface at the different positions. In case 1 / case 2 the soliton hits the interface after 4.5 / 5mm of propagation. The solitons are formed and reflected in both cases. However the soliton in case 2 is reflected around 20μm further from its transmission point than the soliton in case 1 as a result of the earlier reflection from the interface.

In the intensity-dependent measurements the input beam incident angle was kept 0.5^0, corresponding to Figure 6.10 and Figure 6.11 conditions and the sample was positioned so that the beam propagates around 5mm before hitting the interface. In that way the solitons are well formed before they hit the interface.
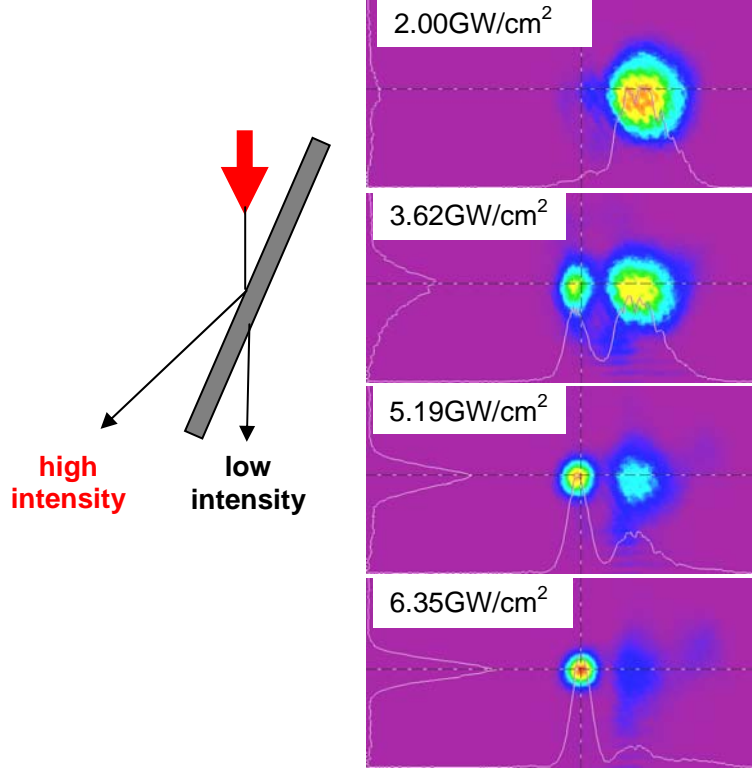
Figure 6.12: Intensity-dependent output beam patterns are shown. The beam incidence angle was fixed at 0.5^0.

At low intensities, around $2GW/cm^2$, the beam was completely transmitted. The transmitted beam is wide, has diffracted considerably and is far from a soliton solution. The output beam shape results from the low input intensity and the transfer through the 6μm thick interface. At around $3.5GW/cm^2$ a fraction of the input beam is reflected, defining the intensity threshold for the reflections. With a further intensity increase a larger fraction of the beam gets reflected, resulting for intensities higher than $6GW/cm^2$ an almost 90% reflectivity. There is no change in the reflected beam position with further intensity increase, in agreement with the simulations from Figure 6.7.
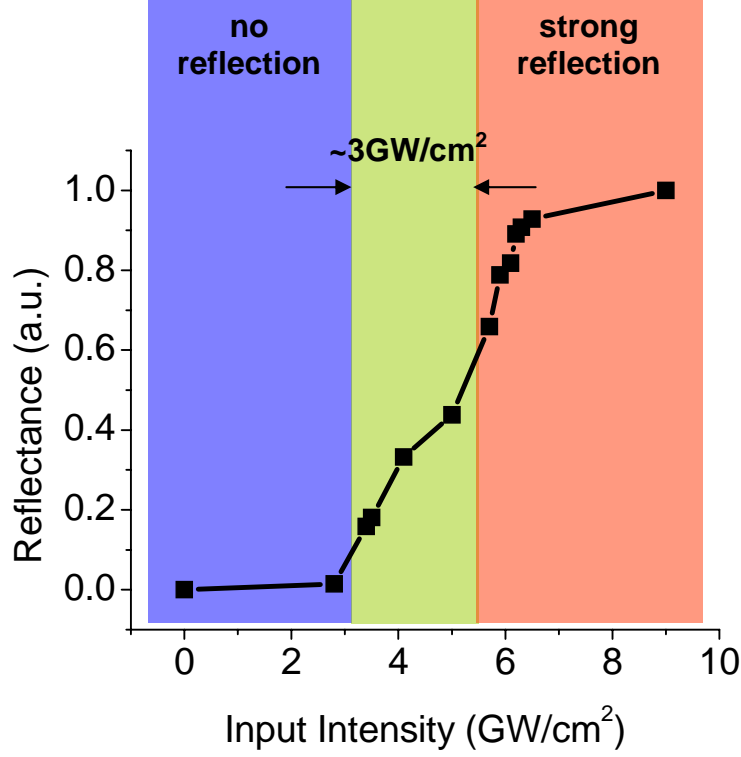
Figure 6.13: Reflectance versus the input beam intensity is shown, corresponding to the output pictures in Figure 6.12.

The intensity-dependent transition from total transmission to maximum reflection is shown in Figure 6.13 as a reflectance versus peak input intensity curve. The data represent the reflected/transmitted power ratio and correspond to the measured output patterns shown in Figure 6.12. From the graph shown in Figure 6.13 an intermediate intensity region, where both the transmission and the reflection occur, spreads over a range of $3GW/cm^2$. This feature is considered to be directly related to the pulsed nature of the input beam, as seen in the simulations as well. In order to get a steeper change of the reflectance, one has to perform an initial pulse shaping, making the pulse to be square-like.

In conclusion, the intensity-dependent reflections were experimentally verified by using a specially engineered multi-region QPM sample. The reflections result from the perturbation of the soliton upon its interaction with the engineered interface. There is a good qualitative agreement between the experiments and the theoretical simulations. The feature could have potential applications for intensity dependent beam steering, all-optical switching and soliton guiding (due to multiple reflections). The experiments have opened new horizons for manipulating nonlinear properties and using the effects which they make possible.

CHAPTER SEVEN: POTASSIUM NIOBATE QUADRATIC SOLITON COLLISIONS

This chapter is devoted to the most intriguing branch of all of spatial soliton science, namely soliton collisions and interactions. However, the discussion is concentrated on two dimensional, (2+1)D, quadratic spatial soliton collisions only. Two special cases, a "nearly collinear" configuration and a non-planar collision, were experimentally realized in a KN sample. These KN configurations are discussed both experimentally and theoretically. However the emphasis is on the experimental side since these were the first experiments to demonstrate in depth the features of two dimensional quadratic soliton collisions.

7.1   Theoretical background

Spatial soliton collisions have been extensively investigated as they are one of the most intriguing of soliton features. For a review on the recent achievements in this field see ref. [1, 2, 9, 11]. Considering a Kerr system, when solitons collide they either repel or attract, depending on their relative phase. However the soliton number is always conserved since Kerr systems are integrable [3, 4]. Another extensively explored category is the saturable-Kerr system, in particular photorefractive material systems which exhibit repulsion for a π phase difference

between the input solitons in a fashion similar to Kerr, and fusion for in phase soliton interactions, a feature not observed in Kerr systems [5, 6].

Quadratic nonlinear systems, based on their collision properties, exhibit similar features to the saturable-Kerr systems. However, quadratic soliton collisions rely on conversion processes, a property which is inherently different from the index change based processes in Kerr and saturable-Kerr systems. For interactions between two quadratic solitons the nonlinear terms are given by:

$$
\begin{aligned}
E_{SH}E_{FW}^* &= a_{SH}a_{FW}^* + b_{SH}b_{FW}^* + a_{SH}b_{FW}^* + b_{SH}a_{FW}^* \\
E_{FF}E_{FF} &= a_{FW}^2 + b_{FW}^2 + 2a_{FW}b_{FW}
\end{aligned}
\tag{7.1}
$$

where a and b are the field amplitude components (FW and SH) for two interacting solitons. In the above equations the cross terms (ab type of field products) are responsible for the interactions. According to ref. [7] the following set of the coupled equations describes the individual soliton FW and SH processes:

$$
\begin{aligned}
\frac{\partial}{\partial z}a_{FW}(z) - iD\nabla_T^2 a_{FW}(z) &= i\Gamma\left(a_{SH}(z)a_{FW}^*(z) + \Phi_a^{FW}\right) \\
\frac{\partial}{\partial z}b_{FW}(z) - iD\nabla_T^2 b_{FW}(z) &= i\Gamma\left(b_{SH}(z)b_{FW}^*(z) + \Phi_b^{FW}\right) \\
\frac{\partial}{\partial z}a_{SH}(z) - \frac{i}{2}D\nabla_T^2 a_{SH}(z) &= i\Gamma\left(a_{FW}^2(z) + \Phi_a^{SH}\right) \\
\frac{\partial}{\partial z}b_{SH}(z) - \frac{i}{2}D\nabla_T^2 b_{SH}(z) &= i\Gamma\left(b_{FW}^2(z) + \Phi_b^{SH}\right)
\end{aligned}
\tag{7.2}
$$

Here the interaction cross terms are contained in the Φs.

The results of the interaction can be understood in very simple terms by considering only 0 and π relative phase between the interacting solitons. The cross terms, contained in Φ, are

given by

$$\Phi_a^{FW} = \pm a_{SH} b_{FW}^* \pm b_{SH} a_{FW}^* + b_{SH} b_{FW}^*$$
$$\Phi_b^{FW} = \pm a_{SH} b_{FW}^* \pm b_{SH} a_{FW}^* + a_{SH} a_{FW}^*$$
$$\Phi_a^{SH} = b_{FW}^2 \pm 2 a_{FW} b_{FW}$$
$$\Phi_b^{SH} = a_{FW}^2 \pm 2 a_{FW} b_{FW}$$

$$(7.3)$$

where the upper (plus) and lower (minus) sign correspond to the 0 and π relative phase cases, respectively. All terms add together at the 0 relative phase and contribute to an increase in the nonlinear conversion processes in the overlap region and therefore to an increase in the soliton component's amplitudes. Thus the solitons are attracted to each other, eventually collapsing into one. In the case of a π relative phase, the destructive interference due to Φ results in the separation of the soliton centroids. Therefore the solitons repel. More details and discussions on the physical background for the phase dependent collision effects are given in ref. [7].

7.2   KN experimental setup

In order to perform the experimental investigations on quadratic spatial soliton collisions an 11mm KN sample was used. Despite the complications related to using the OPG-OPA as a tunable laser source, it was desirable to operate at 983nm, in the vicinity of a potassium niobate NCPM condition. In this case the colliding solitons can be generated under identical conditions due to the ultrawide acceptance bandwidth. Also at NCPM the tolerance on the initial conditions is an order of magnitude better than for the critically phase matched configurations giving much better control over the experimental conditions.

91
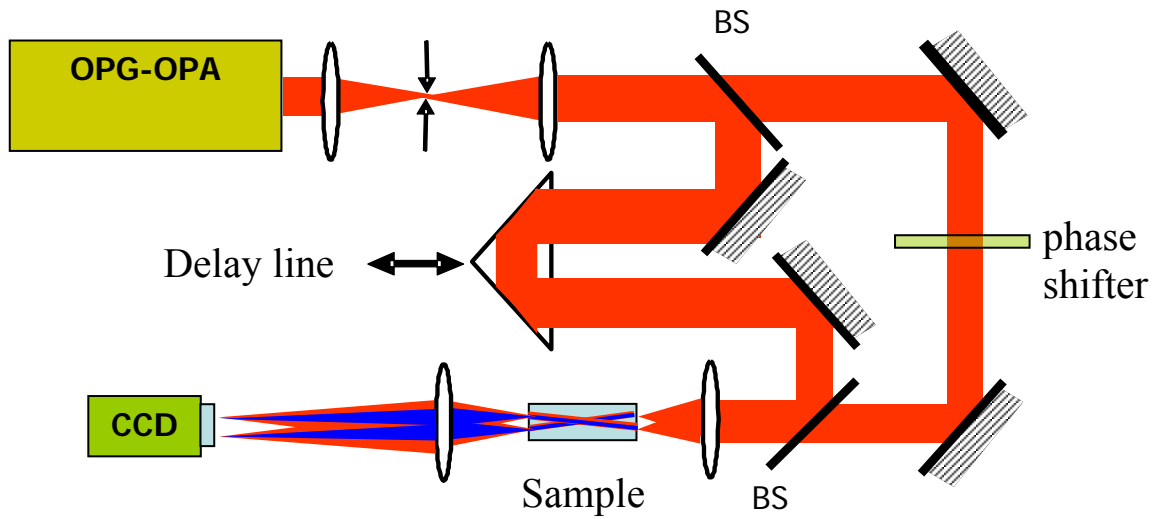
Figure 7.1: KN soliton collisions experimental setup.

The experimental setup for performing the soliton collisions in KN is shown in Figure 7.1. The spatially filtered output from the OPG-OPA is divided into two beams, each meant to generate a soliton. The beams are focused down to the 18μm spots after being combined at a beamsplitter (BS). The solitons are formed upon propagation through the KN sample. The output was imaged onto a Si CCD camera. The delay line, in Figure 7.1, provided temporal overlap between the 25ps pulses. The relative phase between the solitons was controlled by tilting a ~50μm thick glass plate. The glass plate tilt was calibrated by measuring fringes at the output CCD camera in order to relate the tilt to the phase change introduced. If the plate was tilted at 45^0 relative to the beam propagation direction, around 2.5 degrees additional tilt provided a 2π phase change. In order to determine a collision angle, the separations and positions of the non-interacting beams were recorded at both the input and the output from the sample. The phase

shifter, the CCD camera and the energy detectors were synchronized on a shot-to-shot basis by using a computer with LabView software for control and data acquisition. In fact, a full 2π relative phase scan of a collision process, generating several hundred CCD pictures and energy data charts, takes only several tens of seconds. In this way the phase jitter influence, caused by the air flow for instance, was minimized to a negligible level.

7.3   Nearly collinear configuration

This section gives details of experimental observations of soliton interactions for a nearly collinear configuration. The sample was kept at "room" temperature and the wavelength was set around 983nm in order to achieve NCPM. The initial separation between the beams was around 50μm and they were launched at a small relative angle of 0.17^0 resulting in a 30μm separation at the output from the crystal. It was favorable to launch the beams at a small given angle in order to provide enough propagation length for the beams to form the solitons before they start to interact with each other and also to bring them closer together in the second half of the crystal so that they can perform the interactions efficiently.
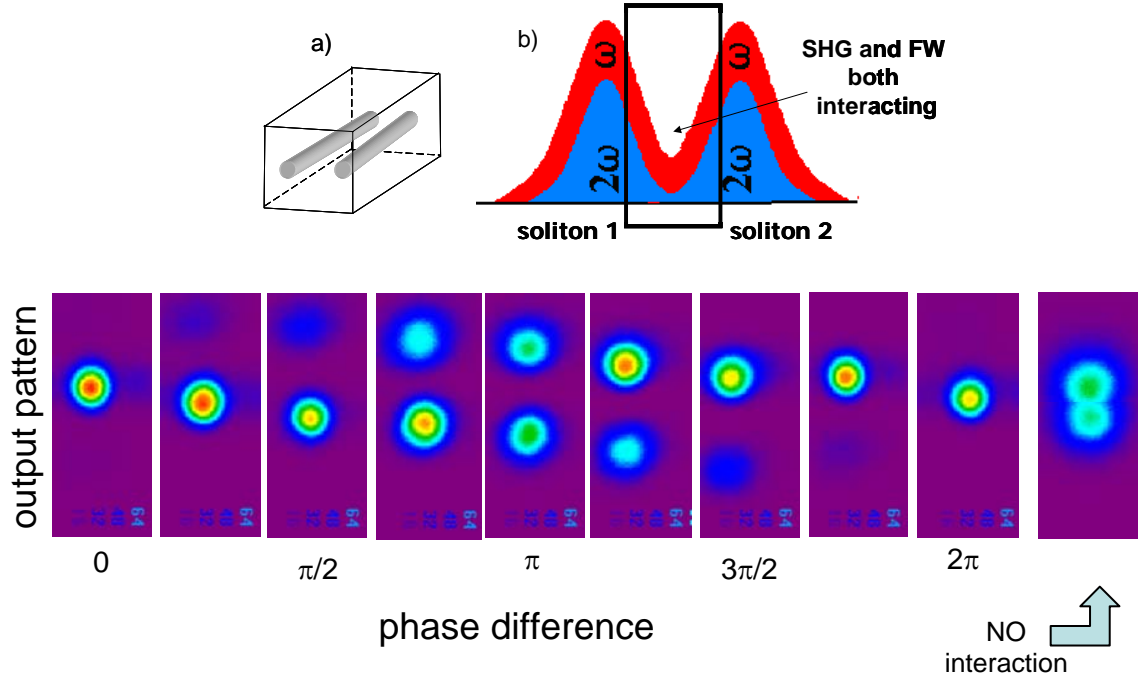
Figure 7.2: a) The schematic of the nearly parallel configuration used in the experiment b) illustration of the solitons in interaction and c) the experimentally observed output patterns as a function of the relative input phase between the solitons for the nearly co-parallel case. The output with no interaction is also given in order to show the soliton separation at the output in the absence of an interaction.

Figure 7.2 shows a set of the output patterns, realized at the KN sample output, and their dependence on the relative phase between the solitons. As shown there, the pattern changes dramatically with the phase. Single soliton output is realized at the 0 phase, as expected from the theoretical analysis and the above discussion. The solitons attract and with the propagation collapse and finally form a single soliton. The single soliton is well formed in this configuration, as seen in Figure 7.2 (0 phase). However, generally the fusion process requires some propagation distance in order to realize and it is configuration dependent which determines whether at the sample output a complete or a partial fusion occurs.

Another limiting case occurs at π phase difference which results in well separated solitons (Figure 7.2). Compared with the non-interacting case shown on the right-hand-side in Figure 7.2, the soliton's separation increased by almost three times due to the repulsion interaction effects. In the intermediate regime between 0 and π, two unequal intensity beams are observed at the output. The beams are separated by nearly the same distance as for the π phase difference case. Initially carrying equal intensities the solitons undergo energy exchange processes during the interactions. The energy flow direction is phase dependent and, according to the output pictures, it is anti-symmetric around zero phase. The observed features are in agreement with the theoretically known behavior.
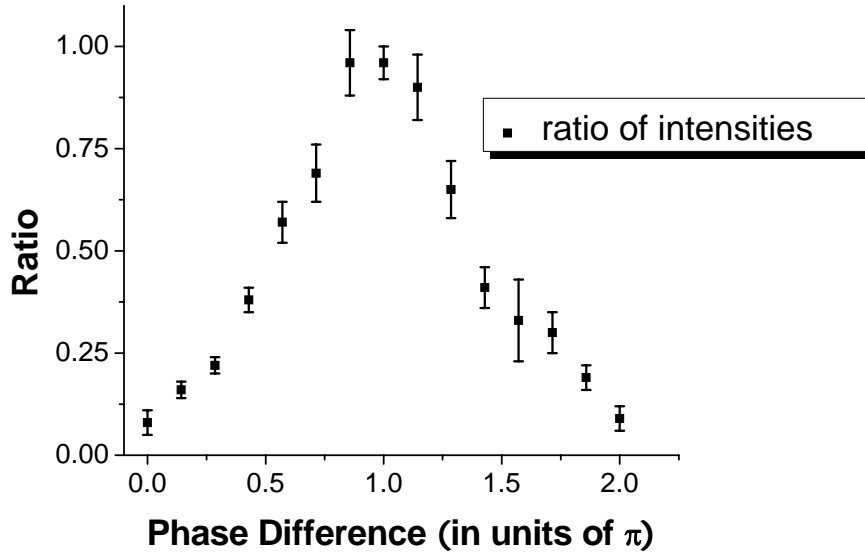
Figure 7.3: Intensity ratio (weaker soliton/stronger soliton) versus relative phase difference for the nearly co-parallel soliton configuration.

In order to explore the energy transfer between the solitons for the measurements given in Figure 7.2, it is convenient to define the ratio between the weaker and the stronger soliton intensities. Figure 7.3 shows this ratio as a function of the relative phase difference between the solitons. The zero value in the graph at 0 phase difference indicates a single soliton output (fusion) and the ratio equal to unity around the π phase, indicates the existence of two equally strong solitons.

The very good control of the experimental conditions because of both the Labview control and the insensitivity of the experimental conditions to perturbations in the vicinity of NCPM, resulted in a precisely performed characterization of the phase effects associated with the soliton interaction processes.

7.4   Birth of a soliton

The soliton interactions discussed in the previous section all took place with soliton trajectories in a common plane. The configuration of interest investigated next is shown in Figure 7.4. This interaction geometry is unique because of its non-planar character with a center to center separation of around 10μm in the vertical direction. The inputted beams were "collided" (i.e. underwent strong interaction) after about 5mm of propagation at a 0.9^0 collision angle between the beams. Usually angles smaller than 0.6^0 are considered to be "small" collision angles and they typically result in behavior similar to the "nearly parallel" case discussed previously. For angles which are larger than 1.4^0, large collision angles, only energy exchange processes are expected from simulations. The current configuration corresponds to the

intermediate regime of the collisions. The individual solitons were generated at ~4.5GW/cm^2, while the soliton threshold for the given conditions was ~3GW/cm^2.
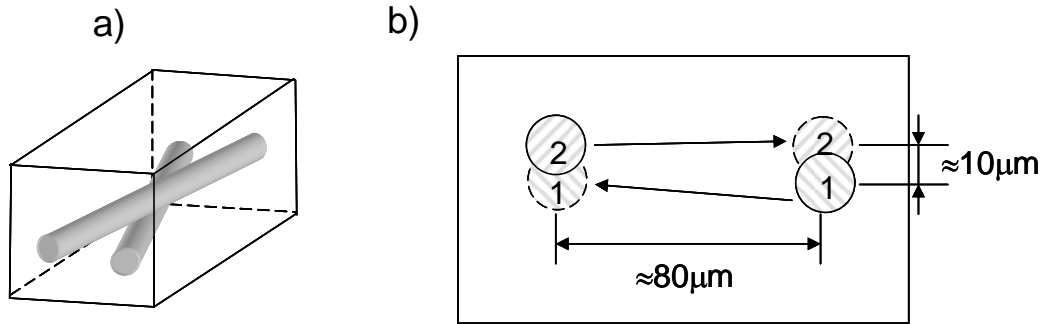
Figure 7.4: The schematic of a two soliton collision process in a non-planar configuration. The solitons are collided in the middle of the sample.
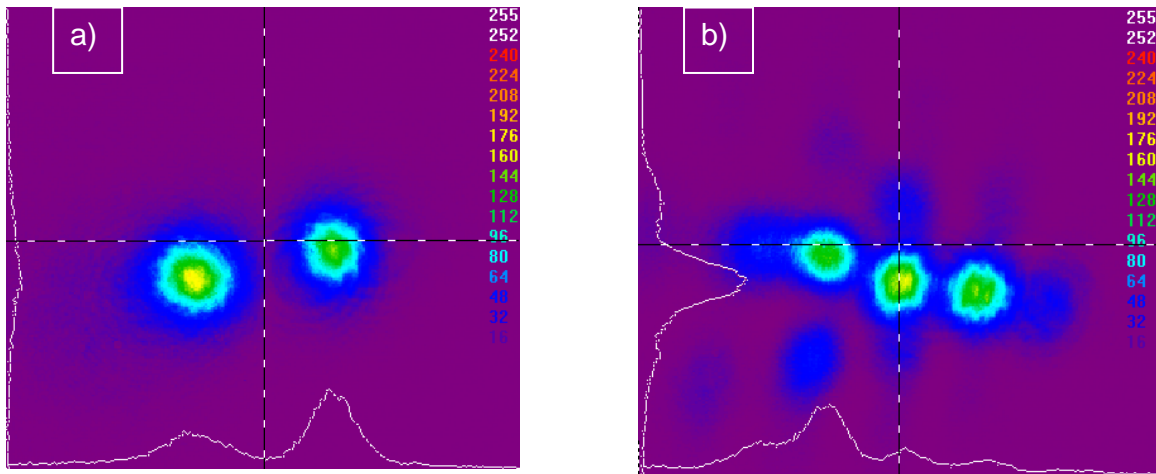
Figure 7.5: a) The output distribution if there is no interaction between the solitons and b) An output pattern if the solitons interact.

The output distribution when there is no interaction between the propagating solitons is given in Figure 7.5a. This result is achieved by displacing the delay line so that the 25ps long

pulses no longer overlap in time. For the configuration given in Figure 7.4b, a three soliton output pattern was observed when the two propagating solitons interacted with each other. The output solitons were tilted at the sample output relative to the solitons in the non-interacting output pattern. This is considered to be a direct consequence of the initial non-planar configuration. In fact, the solitons perform a small rotation due to the initial angular momentum associated with the input geometry. Similar spiraling effects were observed previously in a Type II configuration [8, 9]. As can be seen from the figure above, an additional soliton is generated in the collision process. This was observed for the first time in quadratic nonlinear systems. The effect of generating an additional soliton from a two soliton interaction was previously observed only in photorefractive systems [10] and that was conducted under similar collision angle conditions. Therefore the birth of a soliton seems to be a generic soliton collision effect occurring around 0.9^0 collision angles in a non-planar geometry. According to the observed output solitons (Figure 7.5b) the intensity is distributed uniformly over the three output solitons. This three soliton feature was found experimentally to be sensitive to the configuration details, favoring a higher intensity middle soliton at higher input beam intensities. The multi-soliton output is also sensitive to the choice of collision angle as well. For smaller angles the middle soliton was more prominent while at larger angles the middle soliton intensity decreased along with a loss of the net rotation. In fact even for the coplanar case a third soliton was observed when the other parameters (the angle and the intensity) were kept the same. Numerical simulations of the collisions produced results in good agreement with the measurements.

In order to perform a full relative phase scan, the collision angle and the input beam intensities which led to the stable three soliton features were optimized. Figure 7.6shows a set of

the output pictures when the relative phase between the input solitons was varied. The pictures correspond to the configuration shown in Figure 7.4and are rotated for 90^0 relative to the pictures in Figure 7.5. As can be seen from the scan, the additional soliton which is generated at 0 relative phase and is centered between two side solitons, shifts towards one side and finally merges with a side soliton as the relative phase difference increases. At π phase difference a two soliton output is observed although the limited sample length hindered the soliton regeneration after the collision process.
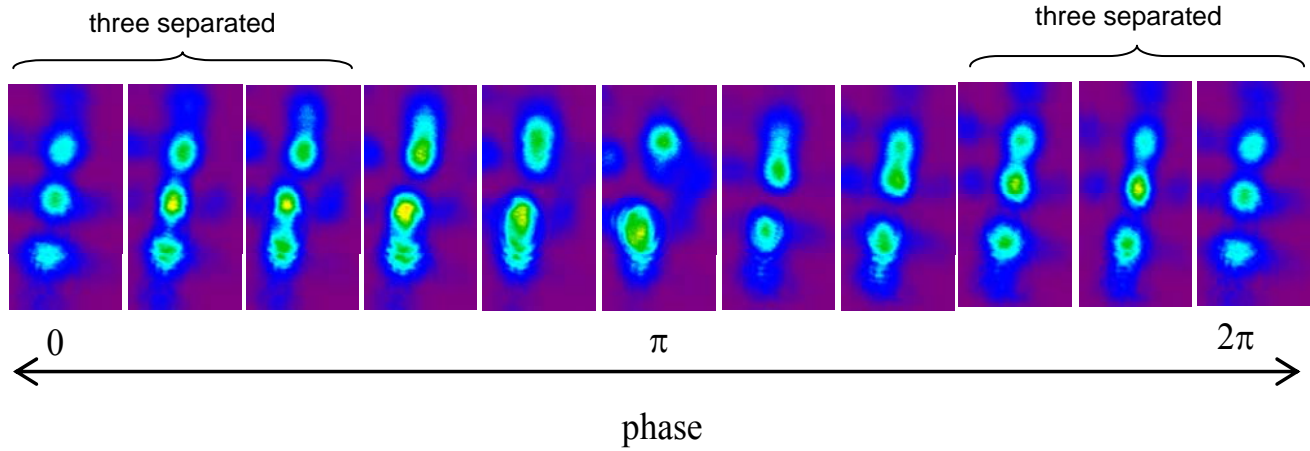
Figure 7.6: Set of output pictures as a function of the relative phase between the colliding solitons. The regions around 0 and 2π relative phase show the three soliton output patterns, as indicated.

CW numerical simulations were performed by using a BPM code developed for quadratic soliton problems. The simulation conditions were set to correspond to the experimental parameters. As shown in Figure 7.7, at 0 relative phase three solitons are observed and only two

solitons at π relative phase. This is in good qualitative agreement with the experimental measurements. The simulations showed the same type of sensitivity to the initial conditions such as collision angle, intensity etc. as observed experimentally. Even for the optimum configuration the simulations still favored the central soliton, as can be seen for the 0 phase case in Figure 7.7. The simulations also indicated the possibility of five coplanar solitons to be generated within a single collision process. However the range of conditions needed to observe those were very restricted, even more limited than those for the current configuration.
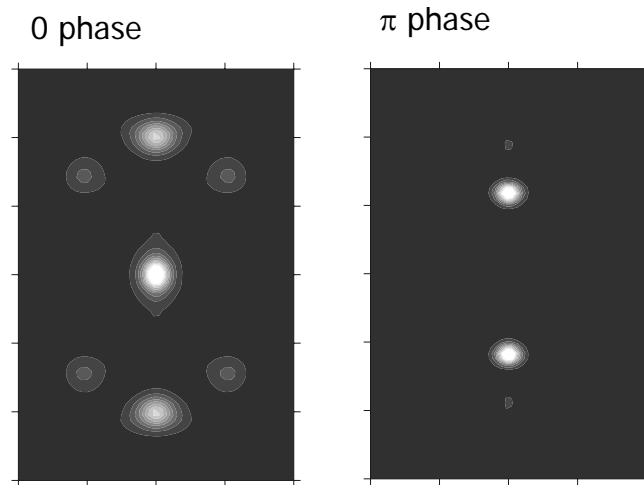
Figure 7.7: BPM CW numerical simulations.
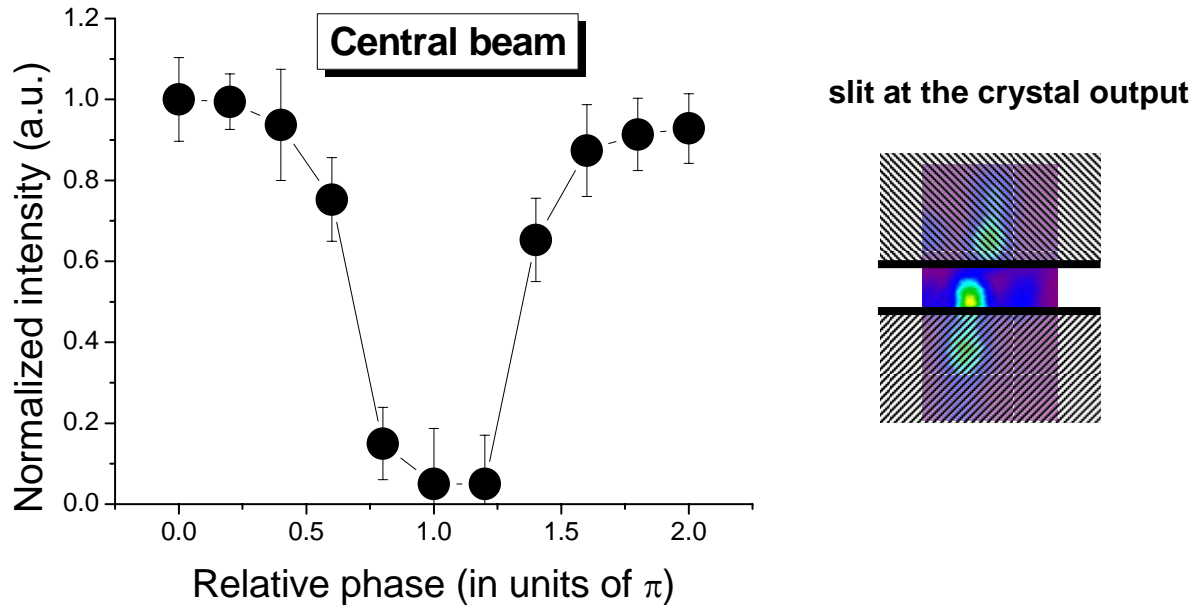
Figure 7.8: The graph shows the dependence on the relative phase difference between the solitons of the intensity of the beam passing through the slit placed at the crystal output, as shown on the right side picture..

Using the fact that there is a well defined phase range around 0 relative phase where three solitons are formed at the output from the sample, one can realize all optical switching. By placing a slit at the output of the crystal, as shown in Figure 7.8(right), only the central soliton is transmitted to the detector. The graph in Figure 7.8(left) shows the intensity of the beam passing the slit versus the relative phase difference between the colliding solitons. Clearly, the intensity is high within a range of almost π around zero phase. Since it is usually possible to control the phase within such tolerances, the properties of this collision configuration could be used as an AND gate if one can keep the relative phase around zero. On the other hand there is a relatively

101

fast change in the intensity as the phase increases beyond around 0.7π, opening the switching possibilities in this direction as well.

In conclusion, quadratic soliton interactions and collisions were investigated in potassium niobate. The experiments performed showed that the relative phase between the solitons can dramatically influence the output patterns. In the parallel configuration fusion, energy transfer and repulsion were observed, as expected from theory. The relative phase was scanned with an impressive $\pi/20$ precision. Collisions at 0.9^0 relative angle resulted in partial fission for the in-phase solitons (three solitons output) and two solitons for the π relative phase. The additional soliton generation effect could find applications in all-optical switching.

CHAPTER EIGHT: PPKTP QUADRATIC SOLITON COLLISIONS

The previous chapter has discussed some aspects of quadratic soliton collision processes. Because of the relatively large two photon absorption (TPA) at the SH wavelength,[3] KN has a tendency to form solitons composed mainly of the FW. In addition, using the OPG-OPA as a light source introduced a significant amount of experimental noise due to the shot-to-shot pulse energy variations and the jitter in the beam's directionality. On the other hand, PPKTP does not suffer from these problems and still has a large effective nonlinear coefficient (9.5pm/V). Therefore PPKTP is attractive for performing a detailed experimental analysis of collision processes.

8.1 Experimental conditions

The experimental setup was organized in a similar way to the KN setup. However, the Nd:YAG laser was used as a light source rather than OPG-OPA as in the KN experiment. The 1064nm laser beam was spatially filtered, divided into two beams by a 50:50 beamsplitter, passed through a delay line, a relative phase control stage and energy control elements. The two beams were then combined by another 50:50 beamsplitter and focused down by a 10cm focal

length lens L1 (Figure 8.1). Each arm generated a single soliton in the 10mm long PPKTP sample. The PPKTP sample used in this experiment has the same properties as the one introduced in section 6.1 except that the current sample used only one QPM region. After the two beams interacted in the sample and exited through the output facet, the resulting pattern was imaged onto a CCD camera by another lens L2 (4cm focal length).
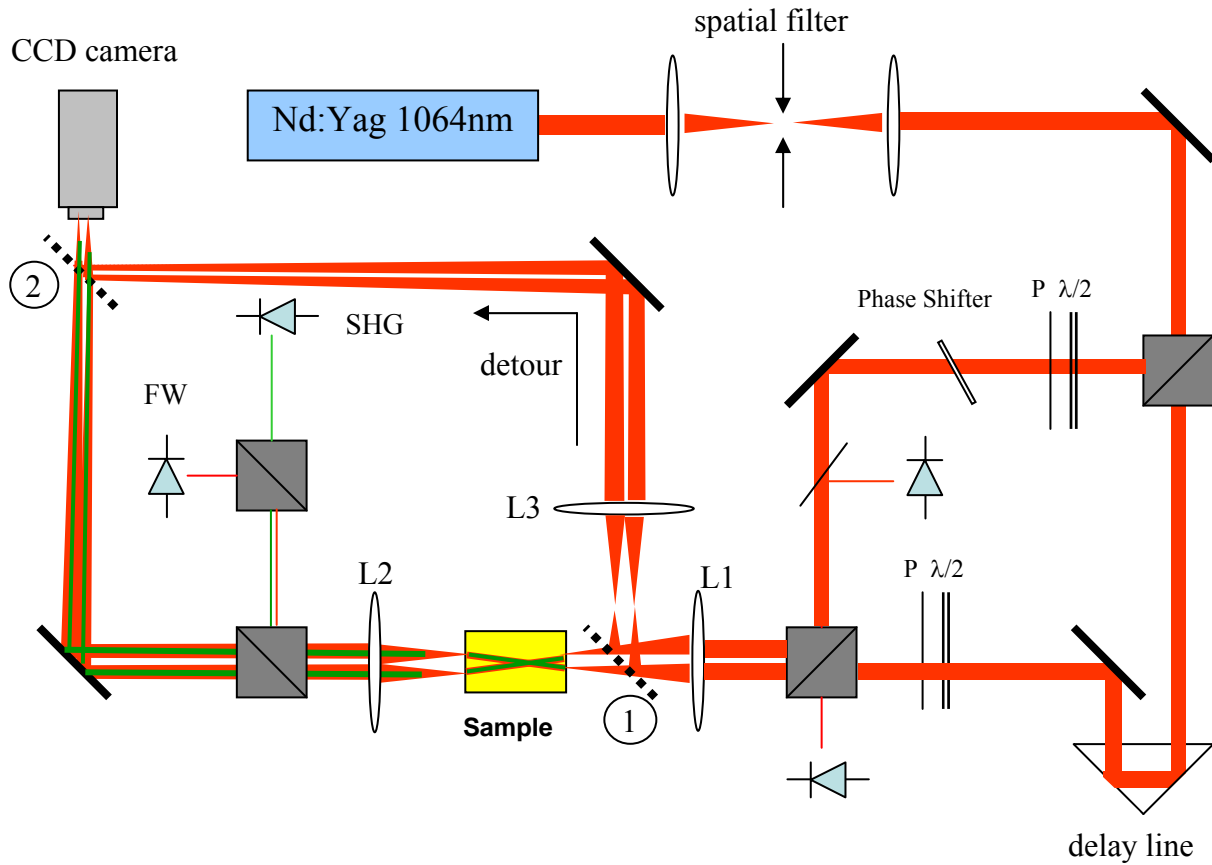
Figure 8.1: PPKTP soliton collisions experimental setup.

A new section introduced into the current setup, compared to the KN soliton collision experimental setup, is the branch used to image the beam's spatial intensity distribution via lens L1 onto the camera. The two "flip" mirrors, 1 and 2, are used to detour the beam. Mirror 1 reflects the beam away from the sample so that the focal plane can be imaged onto the CCD camera. However, the images of the beam profiles in the focal plane, when imaged through lens L2 and through the "detoured" beam path (via lens L3) are different in size as a consequence of the different imaging magnifications in the two paths. Therefore, the beam profiles obtained through the lens L3 required calibration. Also, the configuration, as shown in Figure 8.1, was limited by the camera size ("output window size") to collision angles below 0.7^0. In order to observe large angle collisions (up to $\sim 3^0$) the camera was moved closer.

8.2   Collision processes and soliton formation

In any experiment with a fundamental beam only as the input, the required SH and hence the solitons are generated after some propagation distance. Therefore an experimental realization of a soliton collision process can be dependent on the physical collision point inside the sample.

The beam geometry for investigating beam collisions at the different stages of soliton formation is shown in Figure 8.2. The angle was kept around 0.4^0, which is a relatively small angle and for which efficient fission was expected for the in-phase case. The sample temperature was set to correspond to NCPM and the input beam intensities, around $3.3 GW/cm^2$, were kept slightly above the soliton threshold ($\sim 3 GW/cm^2$). The higher the input intensity, the shorter the distance usually required for soliton formation. Thus by operating just above threshold, it was

105

expected that phenomena connected with incomplete soliton formation would be exaggerated and amenable to investigation. In order to vary the collision point and still maintain the desired collision angle, it was necessary to go through a time consuming input beam alignment procedure for each particular configuration. In addition, even if the collision angle is kept the same, a small misalignment (of ~5µm out of the propagation plane) can cause the beams to propagate in the slightly different planes (non-planar configuration) resulting in spiraling effects.
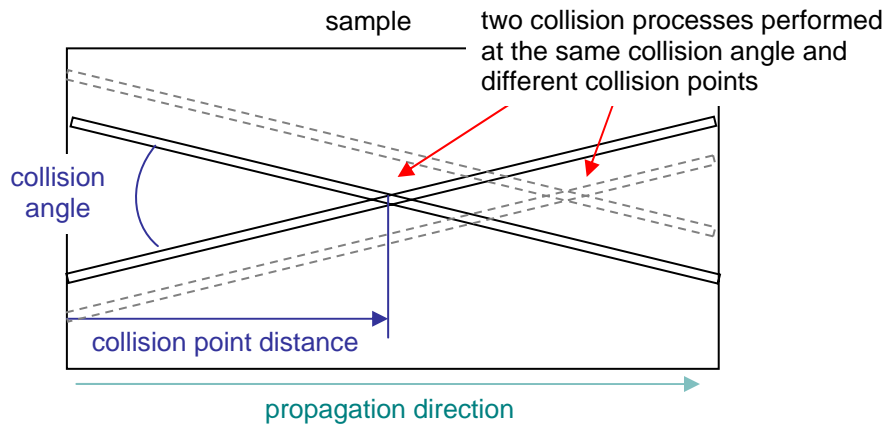
Figure 8.2: Beam geometries for observing the dependence of the collision process on distance into the sample.

The output patterns from the camera shown in Figure 8.3 illustrate the effects of the soliton formation process on the collision results. In the text the "collision point" phrase designates the distance from the front facet of the sample to the position where the collision virtually occurs (Figure 8.2).

106
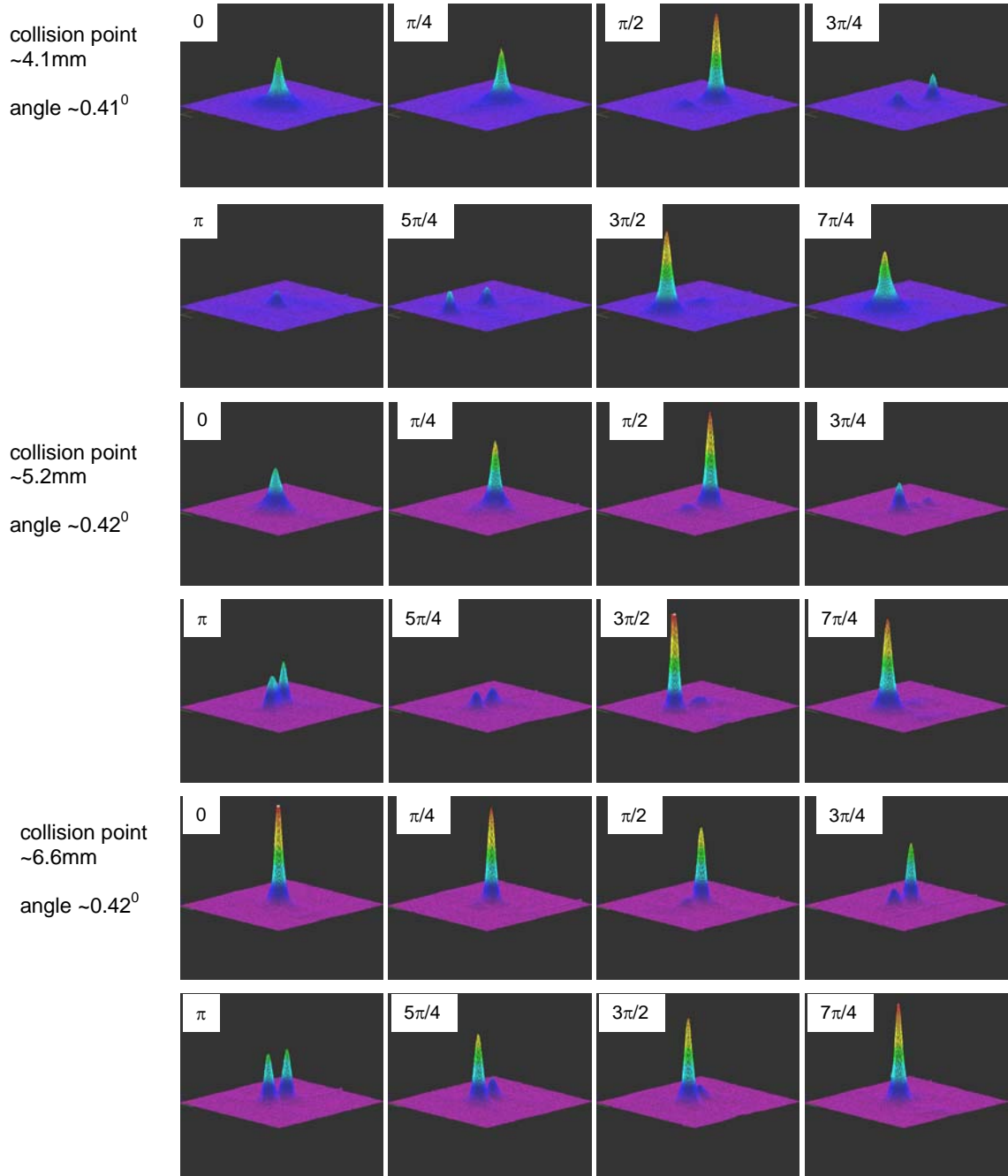
Figure 8.3: Phase dependent output from the collision processes, performed under the different collision conditions, is shown.

The results for three collision points, 4.1, 5.2 and 6.6mm, are shown. Clearly there are dramatic changes in the output associated with changes in the relative phase, similar to that observed in the KN collision experiments discussed in Chapter 7. The 0^0 relative phase case usually shows a collapse into a single, high intensity beam and around π usually two, largely separated beams result from the collisions. One clear difference between the three configurations investigated is the beam shapes. The output beams are much smaller in size in the 6.6mm case. In fact, the output beams generated in the 4.1 and 5.2mm configurations are not well formed solitons. For example, in the 4.1 and 5.2mm cases with 0^0 phase difference, a beam leaves the collision with sufficient intensity to eventually evolve into a soliton. However, at π relative phase, the output beams are barely visible for the 4.1mm case. Notice also the variations in the output beam separation at $3\pi/4$, $\pi/2$, $5\pi/4$ and $3\pi/2$ relative phases. This effect, revealed also in the simulations, is believed to be a consequence of premature interactions. In fact the input beams interfere with each other soon after entering the crystal, resulting in quasi-linear effects. The evolving beams, not yet having formed solitons, are strongly influenced by the interference fringes. For the 6.6mm configuration, over the whole relative phase range the output solitons are well formed, leading to clean collision results. Clearly, there is a required propagation distance before the beams collide in order to perform "soliton" collisions and, under for current input intensity and beam size conditions, this distance is around 6mm.
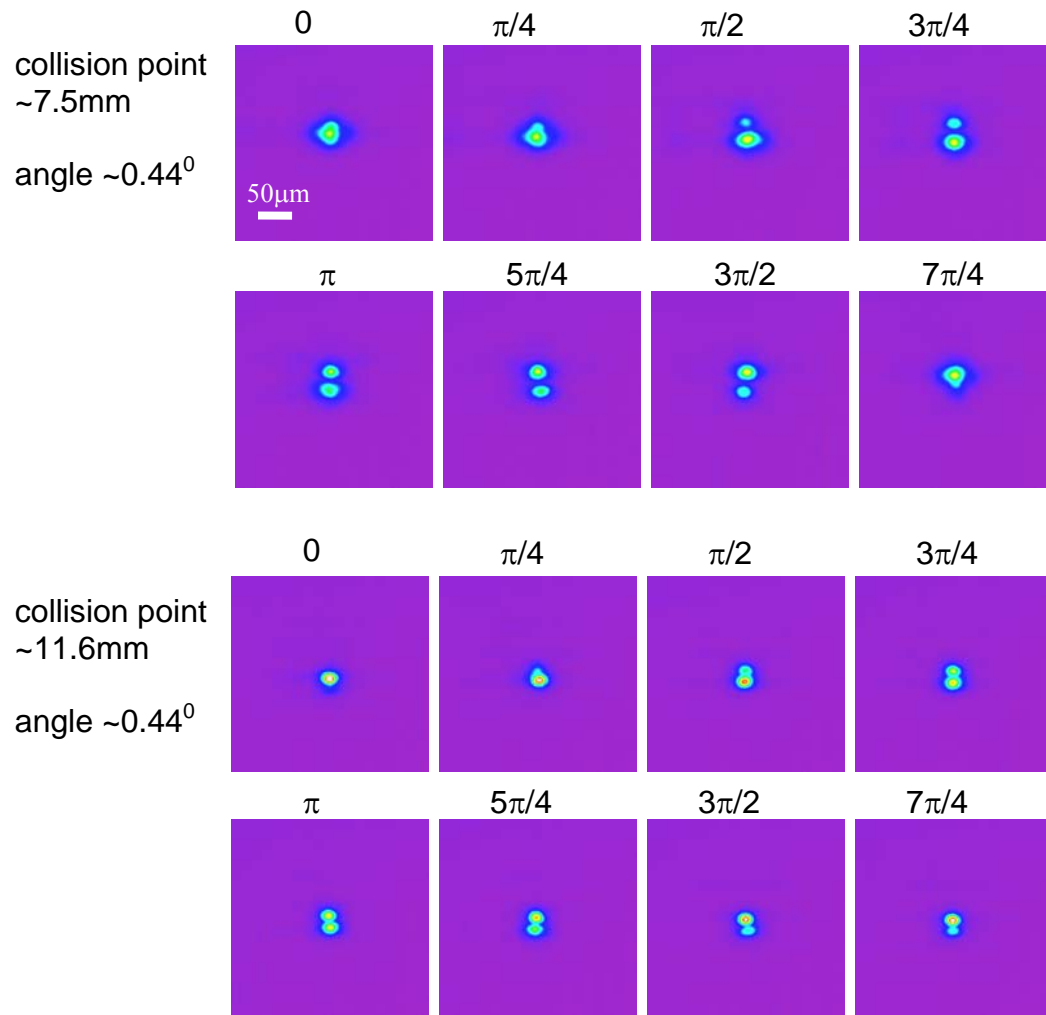
Figure 8.4: Relative phase dependent output from the collision processes performed for the collisions centered at distances of 7.5 and 11mm from the input facet, respectively. The sample length is 10mm.

Figure 8.4 shows the phase dependence of the "output" from collision processes that occurred at the 7.5mm and 11.6mm collision point. Note that in the 11.6 case the solitons

"collide" after passing through the crystal. The angle was kept around 0.4^0. The collisions show fusion around the 0^0 phase, as expected, especially for the 11.6 mm case in which the beams are "pointed" so that they will approximately cross at the output facet. Two equally intense beams (solitons) are observed at π relative phase indicating that the interaction "turns on" through the soliton's evanescent tails even before the individual solitons centroids "collide". Also, in the range from $\pi/2$ to $3\pi/2$ where two soliton outputs were observed, the soliton's output positions do not change significantly with phase but the energy they carry reflects the phase changes more or less as expected from theory. This is a very different behavior from the large beam repulsion observed in the quasi-linear 4.1mm case.

From the numerical simulations performed (the 11.6mm case is shown in Figure 8.5) it is clear that the solitons interact over a large propagation distance. In fact for the simulation outputs shown, the interactions take place over almost 5mm of the soliton's propagation path. Therefore in experiments performed on the 10mm long sample the soliton interactions are still in progress, even at the output of the sample, slightly influencing the output solitons. The observed simulation output pictures are qualitatively in agreement with the experiments.
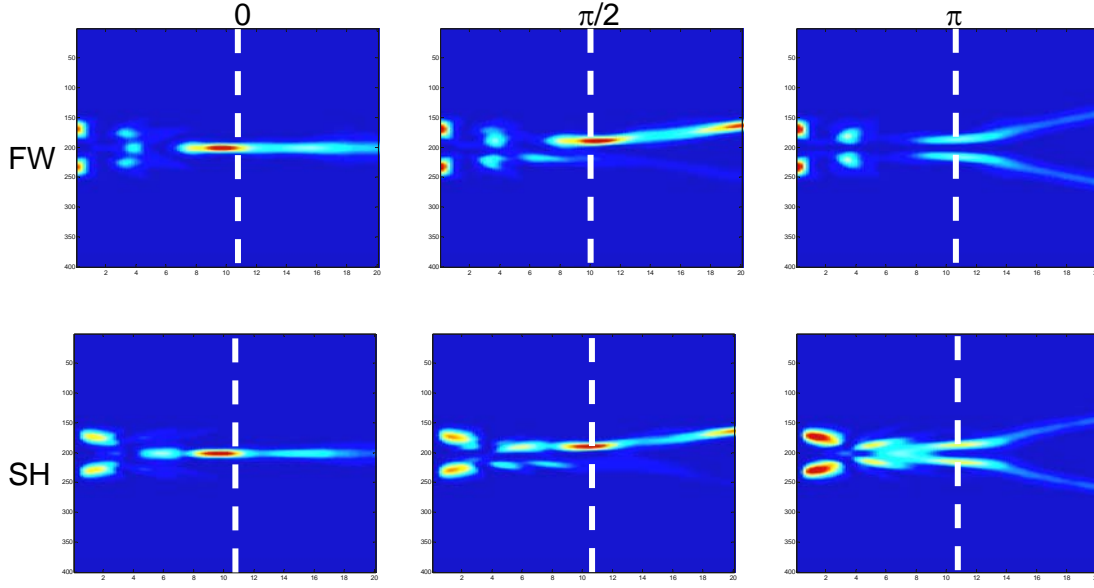
Figure 8.5: CW BPM 2D numerical simulations of the collision processes. The solitons are generated slightly above their threshold and collide at a 0.4^0 angle. The collision point is at 11.6mm, corresponding to the experimental results in Figure 8.4. The pictures show the propagation along a 20mm long sample, which is twice the length of the actual sample. The white vertical dashed line indicates the rear surface of the actual sample.

8.3   Collisions and phase mismatch

From the meticulously performed soliton collision experiments discussed in the above section it is clear that the "collision" point, and therefore the initial and final solitons formed, can strongly influence the output of a collision process. On the other side the phase mismatch influences both the conversion and soliton generation processes. In fact the longest propagation distance for a soliton to fully form is required at phase matching. In order to form a soliton within a shorter propagation distance one has to go to a phase mismatched configuration.

111

However, the threshold intensity required for the soliton generation increases and the generated solitons do not have necessarily the same FW/SH ratio as the ones generated at PM. Therefore the soliton interactions change as the phase mismatch changes. In order to investigate the effects of phase mismatch on the collision processes the soliton collisions were performed under nominally the same conditions except for the different sample temperatures. The collision angle was set at 0.4^0, the input beam intensities were kept around 1.7 times the soliton threshold for a given phase mismatch (the threshold is phase-mismatch dependent) and the collision point was chosen to be 5.2mm. The intensities used in these measurements were set to be higher than the ones previously used (section 8.2) in order to reduce the distance required for soliton formation.

Figure 8.6 shows the output soliton patterns achieved at both PM and phase mismatch, respectively. At PM the output pictures correspond well to the previous results shown in Figure 8.4. However the output is different for the phase mismatch case. At 0^0 relative phase, fusion occurs and the generated soliton is surrounded by an enhanced radiation pattern (bath) relative to the PM case. As the phase changes to $\pi/3$ the second soliton appears, which is different from the PM case where at $\pi/3$ the second beam was barely visible. Around the π relative phase condition both cases again show similar behavior. Between $\pi/2$ and π phase the energy exchange processes still occur. However the intensity ratio between the output solitons is smaller for the mismatched case suggesting that weaker soliton interactions occur in this configuration.
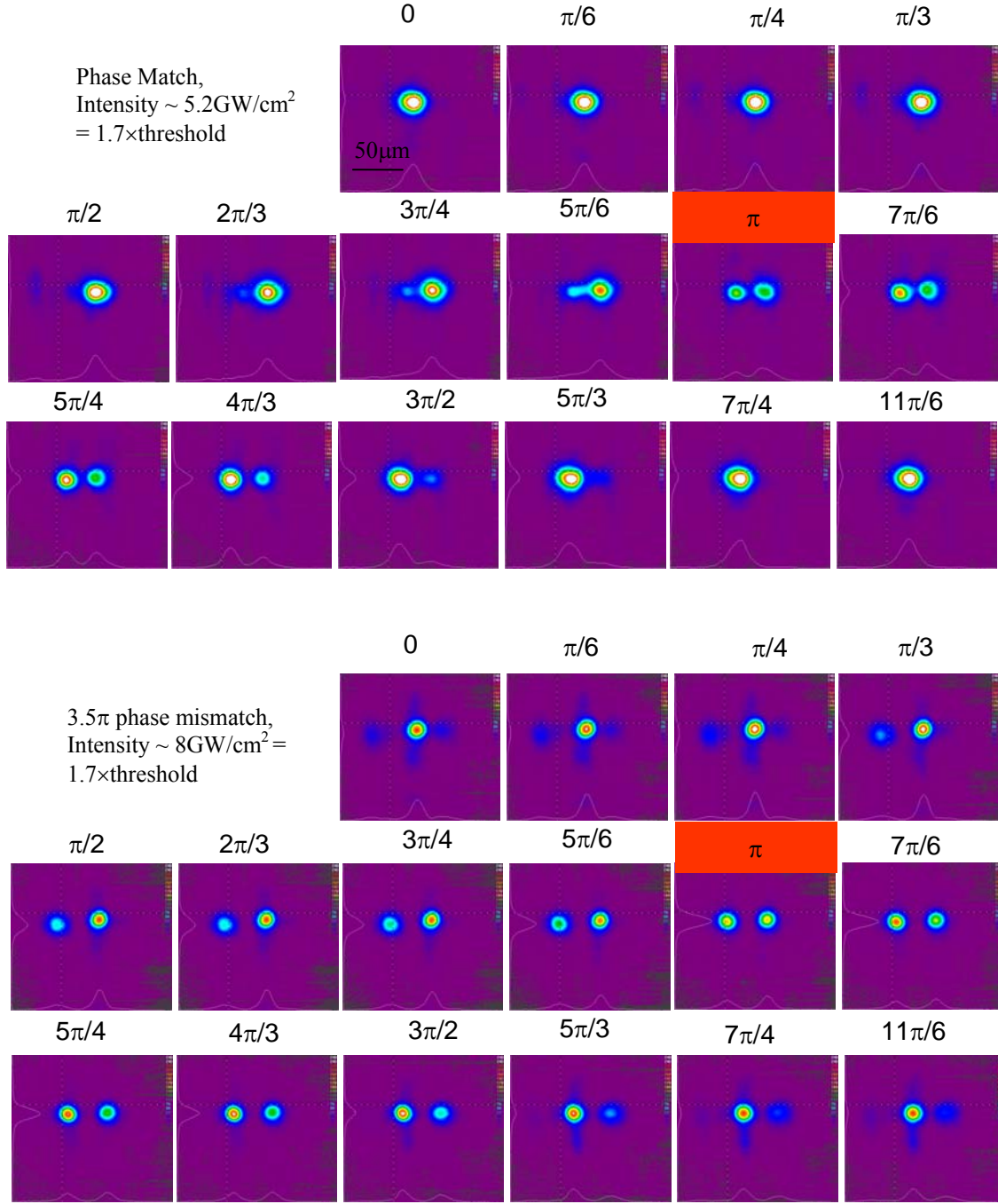
Figure 8.6: Output intensity distributions at different relative phases for the PM and the 3.5π mismatched configurations. The collision point was 5.2mm, the collision angle 0.4⁰, ΔkL ~ 0 (top) and 3.5π (bottom).

113
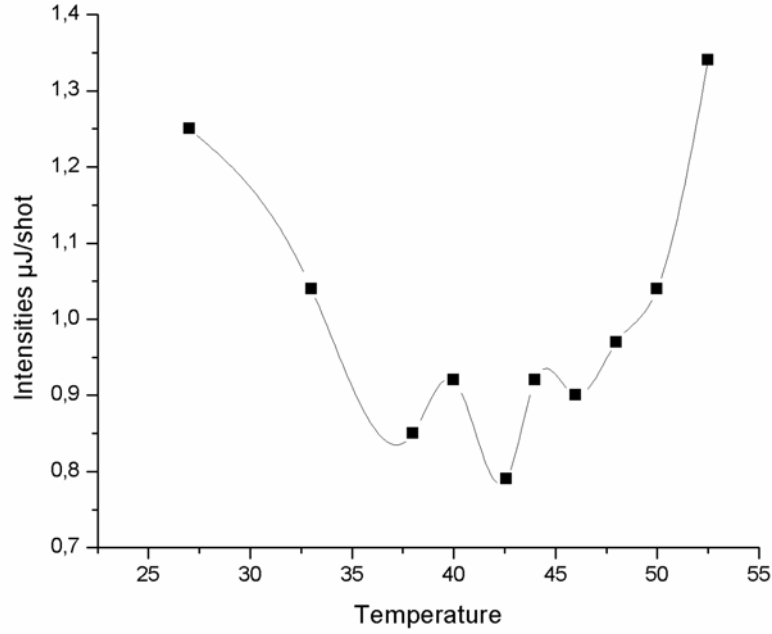
Figure 8.7: Input beam energy, ~1.7 × soliton threshold, as a function of the phase mismatch (sample temperature). The phase matching temperature is at 43.6^0 C.

Figure 8.7 shows the input beam pulse energies, corresponding approximately to 1.7 times the solitons threshold, that were used in characterizing the soliton collision features at the different phase mismatch temperatures, described below. The steeper slope at the higher temperatures is a consequence of a negative phase mismatch and therefore the well-known higher threshold intensity requirement in order to generate the solitons [4].
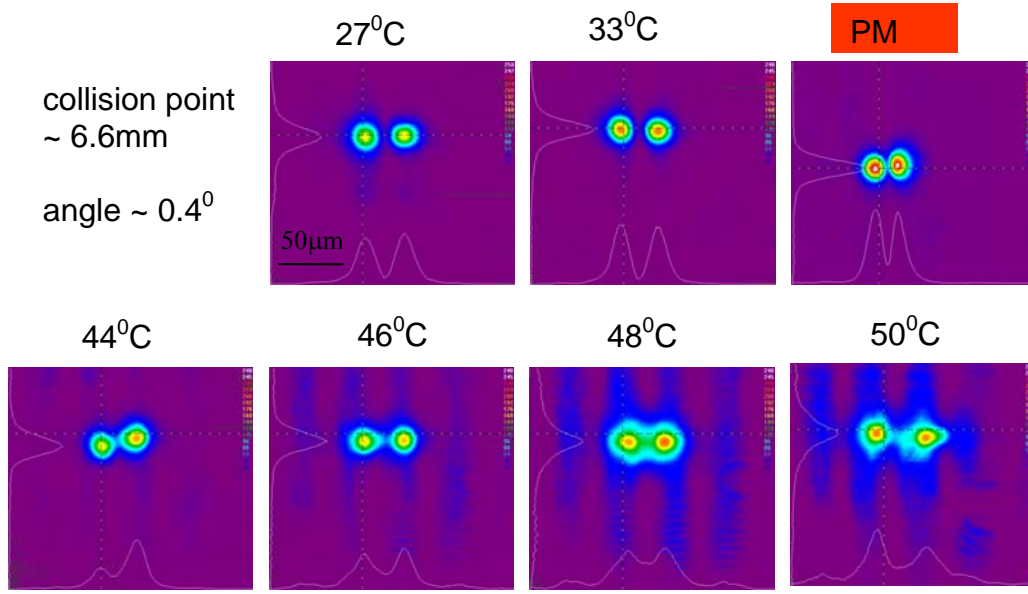
Figure 8.8: The output soliton distributions at different sample temperatures (phase mismatch) for a π phase difference between the solitons. The intensities correspond to the values from Figure 8.7.

An output pattern data set for the collision processes performed under similar conditions but at different phase mismatch is shown in Figure 8.8. Only the π relative phase outputs are shown, since they best represent the trends in the soliton interaction outputs. The solitons are well formed prior to collision in all of the configurations except for the significant radiation (the vertical fringes on the pictures) that occurs at the larger negative phase mismatch ($T > T_{PM}$). The output pictures show significant differences in the soliton separation with temperature. Clearly the separation is the smallest for the phase matched configuration.

Table 8.1: Data on the dependence of the sample temperature on output soliton separation. The data corresponds to the measurements in Figure 8.8.

Sample Temperature (^{0}C)	Input pulse energy (μJ)	Soliton separation (μm)
27	1.25	30
33	1.00	27.8
43.6 (PM)	0.85	22.9
44	0.92	26.4
46	0.9	30
48	0.97	30.8
50	1.00	39.5

The data on the soliton separation along with the pulsed beam energies used in the measurements is summarized in Table 8.1. The separation ranges from ~23μm at the phase matching to ~39μm at T=50^{0}C. In fact, both the input intensity and the separation increase with increasing phase mismatch. However, the measured soliton separation of ~40μm at the sample temperature of 50^{0}C deviates significantly from the trends in the table. Moreover at T=48^{0}C which corresponds to a relatively small change in phase-mismatch the measured distance is almost 10μm smaller. There are at least two possible explanations for this deviation at large negative phase-mismatch, the soliton formation process and the increased background radiation. As the magnitude of the large negative phase mismatches increases, progressively more SH is needed to form a stable soliton. Thus it is possible that the solitons are not well formed at the given intensities for such a large negative phase mismatch, thus leading to a different behavior

relative to collisions that take place at the lower sample temperatures. However, according to the output picture in Figure 8.8 (for T=50^{0}C) the solitons seem to be relatively well-formed. But there is clearly a high intensity background consisting of vertical fringes. Because of this background the transverse soliton mobility is increased, which can strongly influence the final distribution of the solitons. Note that in the 50^{0}C result, the fringe separations are larger and that the solitons appear to be "pulled apart" by the fringes on which they "sit". This is believed to be more dominant effect than the soliton formation itself.
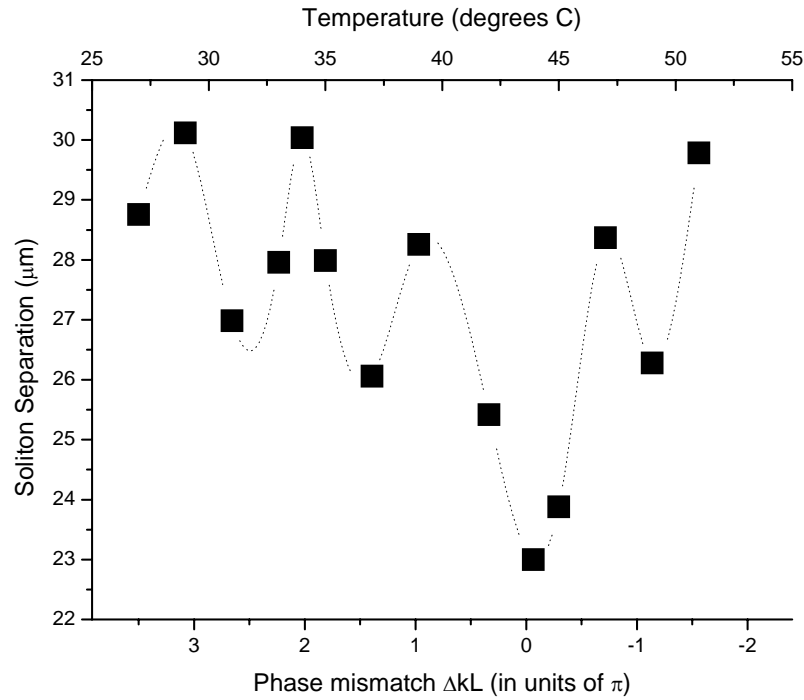
Figure 8.9: Soliton separation as a function of phase mismatch ΔkL. The separation was measured at a π relative phase difference between the input solitons. The dotted line is only a guide for the eyes, not a fit.

The graph given in Figure 8.9 shows in more detail the behavior of soliton separation versus the absolute value of phase mismatch. The graph is based on both the positive and the negative ΔkL measurements, combined together. The measurements were taken at 0.4^0 collision angle with the collision point around 6.5mm. The conditions are similar to those used in Table 8.1 and Figure 8.8. The separations are measured at π phase. As seen from the graph, and given in Table 8.1 as well, the solitons have the smallest separation for the phase matching case. At 2π phase mismatch the separation distance reaches an apparent "saturation" value and with further increase in $|\Delta kL|$ it only oscillates around this stable value (in this particular case $\sim30\mu m$). The oscillations seem to exhibit a regular periodicity (π) reminiscent of the usual SHG sinc^2 behavior found in non-solitonic SHG generation efficiency curves. However, the SHG sinc^2 dependence reaches its minimum when the curve from Figure 8.9 reaches its maximum.

In Figure 8.10 the soliton's output separation as a function of the relative phase between the fundamental beams at the input is shown for a number of phase mismatch configurations. The collision angle was $\sim0.4^0$ and the collisions occurred after $\sim6mm$ of the propagation through the PPKTP sample. The intensities used in the experiment correspond to the values given in Figure 8.7. The solitons are well-separated around the π phase case and the soliton fusion occurs around 0^0 phase difference, as seen from the curves in the graphs below. They are in good agreement with the output patterns observed in Figure 8.6. The small variations of the nearly flat response around π phase (typically 3-5μm variations) occur quite consistently in the data shown in Figure 8.10. However, the measured patterns vary slightly over the range phase mismatch studied, showing even smaller magnitude oscillations for some of the measurements performed

118

under slightly different conditions. In order to deduce the soliton separation values the intensity distribution patterns had to be retrieved from the pictures. The separations were estimated based on the peak-to-peak separations extracted from the intensity distributions allowing around 5-10% error in the values. Also, if there is some radiation pattern at the sample output in the vicinity of the output solitons, the estimated values are less accurate especially for the 0^0 relative phase region because it becomes difficult to judge if the pattern surrounding the strong central soliton is only a radiation field or a remnant of the input soliton. In addition, in spite of the fact that the solitons collide at the same angle and equal propagation distances, the output patterns (including the background radiation) change slightly with the phase mismatch and from shot-to-shot. In some cases solitons were observed to perform small spiraling (the 44^0C case in Figure 8.8). When the spiraling occurs, the interactions are not exactly coplanar. Therefore the estimated distances can deviate slightly from the expected ones.

Considering the shapes of the curves in Figure 8.10, the T=27^0C and 33^0C show a relatively flat top behavior followed by a sharp drop around 0 phase. On the other side of the phase match (negative ΔkL), i.e. at T=46^0C, a "bell shaped" top with a small dip at π relative phase is obtained. However, even on PM where fusion occurs, the decrease in the separation at 0^0 relative phase is quite abrupt. The solitons with a relative phase close to 0^0 undergo strong energy transfer along their propagation. If the energy transfer is strong enough the solitons eventually collapse into one and the remaining energy is either captured by the existing soliton or it appears as radiation. If the solitons do not fuse they propagate along approximately the same paths as those for the π phase case.

119
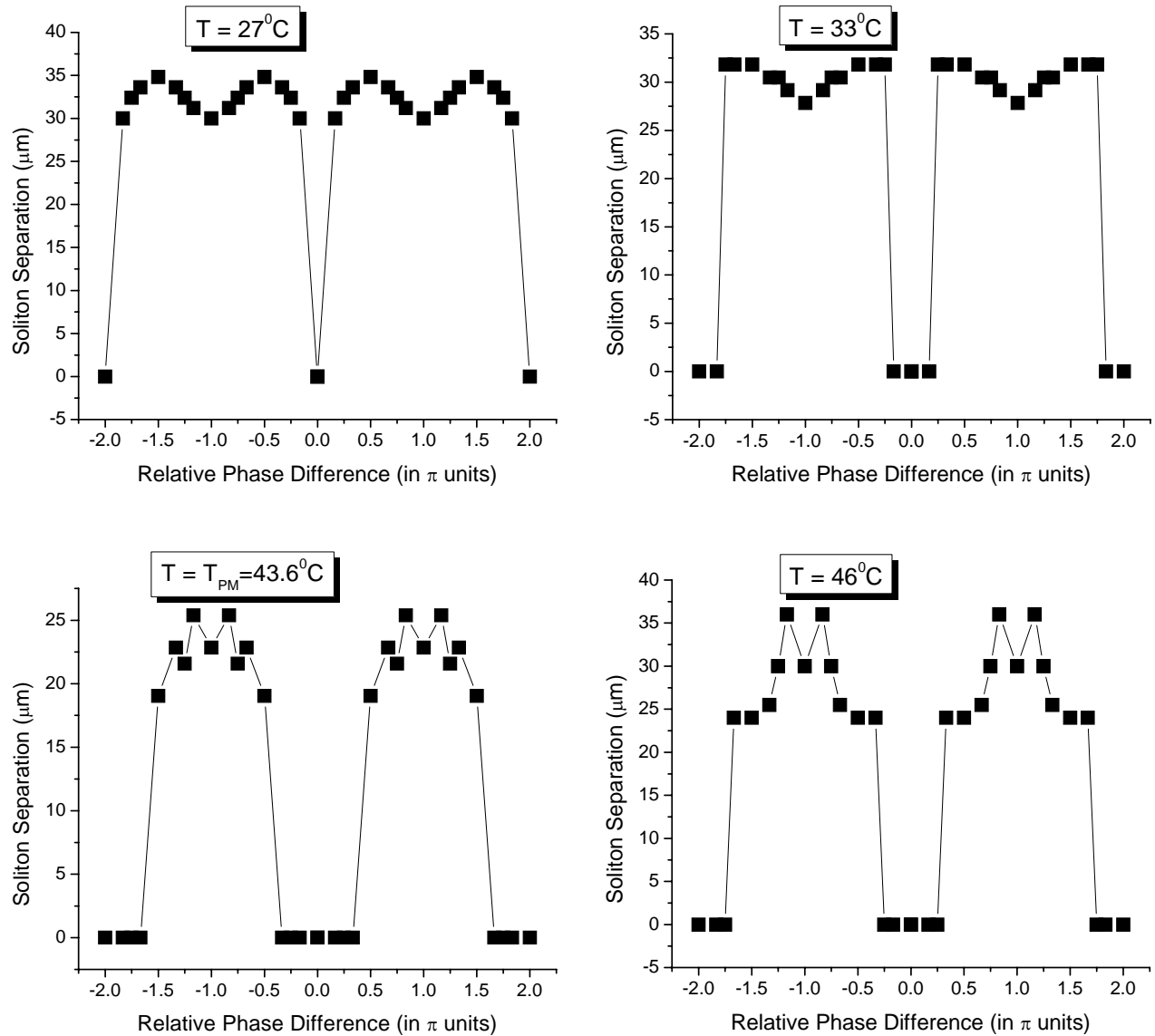
Figure 8.10: Soliton separation versus relative phase difference for various sample temperatures (and hence phase mismatch). The measured data were deduced from output distributions of the type given in Figure 8.8. The data set range was extended to -2π to 2π from its original range from 0 to 2π.

As indicated in the plots above, the range of relative input fundamental phases for which fusion (0^0 separation) occurs decreases as the phase mismatch increases, which is believed to be an indication of weaker interaction processes. This is in agreement with the increase observed in the absolute separation between the output solitons as the phase mismatch is increased when the relative phase between the input beams is kept at π. Both sets of measurements suggest weakening of the soliton interaction strength with increasing absolute phase mismatch. Unfortunately the difficulties in clean soliton generation at large negative phase mismatch (T > 46^0C) limited investigation of these features in that region. However, the behavior at T=46^0C is similar to that for ΔkL>0, indicating suppression of the fusion effect at negative phase mismatch. Altogether, the phase difference region in which efficient fusion occurs decreases by about a factor of two from phase-match (43.6^0C) to phase mismatch at T=33^0C and it occurs only in the close proximity of 0^0 relative phase at T=27^0C, as shown in Figure 8.10.

In order to compare the soliton separation measurements performed for the four ΔkL cases, the data from Figure 8.10 were combined into a single graph, shown in Figure 8.11. Clearly, the separation between the solitons increases with increasing phase mismatch. Comparing the curves, the T=46^0C case not only shows clearly some of the phase matching features (similar shape) but also some of the large phase mismatch features (significantly larger soliton separation around the π phase than for the PM).

The region where fusion occurs and the change associated with ΔkL are clearly delineated in Figure 8.11. However the details of the features depend on a number of parameters such as the collision point and/or the collision angle, especially for the range over which fusion

occurs. In addition, if the input beams are not equal in intensity, the measured curves become asymmetric, showing monotonic drop/rise in the soliton separation when going from smaller to higher phase difference. However the abrupt changes at 0 separation (fusion) still occur. All of the discussed features are valid for angles below the collision angle where three solitons appear (around 0.9^0 according to the observed features in the KN case).
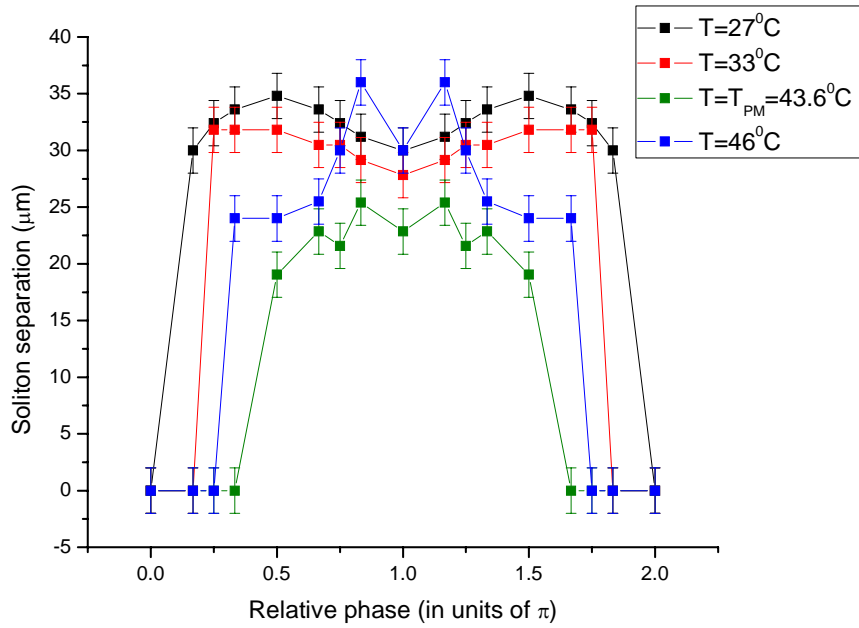
Figure 8.11: Soliton separation as a function of the relative phase between the input fundamental beams at various phase matching conditions. The separation 0µm indicates fusion and a single soliton output. The phase mismatch ΔkL of 3.5π, 2.2π, 0 and 0.5π corresponds to the temperature 27^0, 33^0, 43.6^0 and 46^0C, respectively.

8.4   Soliton collisions at wide angles

It is known from the theoretical considerations that at large collision angles solitons only exchange energy and they cannot perform fusion. Very limited experimental investigations for the large collision angles have been previously reported (section 7.4 on the KN birth of a soliton). When the collision angle increases, even the energy transfer is expected to decrease, eventually resulting in the negligible interaction effects except for small lateral shifts..
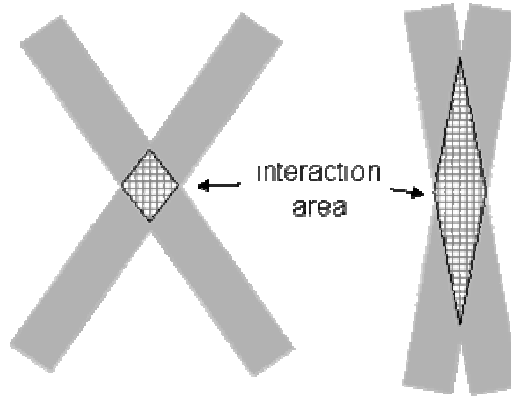
Figure 8.12: Illustration of the dependence of the effective interaction length on the collision angles.

The decrease in the interactions at large collision angles is simply due the very limited propagation distance over which interactions occur before the soliton pulses pass through each other (see Figure 8.12). The phenomena is somewhat more complicated than just interaction length effects because of the reduction in the generation efficiency of the SH components of the soliton with increasing relative angles (and hence phase mismatch). However it is known from

experiments in KN and PPKTP [1, 2] that the soliton generation acceptance bandwidth can be several degrees wide in vicinity of a NCPM. Therefore the collision effects are expected to be mainly dependent on the effective interaction time between the solitons, as already mentioned.

Detailed discussions on the small collision angle case and changes in phase match have already been discussed in the preceding section. The discussion in this section concentrates on an experimental investigation of the dependence of the collision processes on changes in the collision angle. The initial experimental setup used to perform the small collision angle measurements in sections 8.2 and 8.3, as given in Figure 8.1, was limited by the acceptance angle of the imaging system. In fact the imaging system magnification was very useful for providing excellent resolution and the ability to observe details of the PPKTP sample output patterns. However, for that configuration the full camera window size corresponded to only around 80μm at the sample output. It limited the collision angles to smaller than ~0.7^0. To perform the experiments with larger collision angles the camera-imaging lens distance was shortened more than two times. In order for the image to fit into the camera window, an additional lens in the "detour" section was used to image the lens L1 focal plane,. Another lens, ~15cm focal length, was placed close to the camera, making the final image 13 times smaller.

The variation in collision angle experiments had similar alignment issues to those performed on the dependence of collision point on the output patterns that was discussed in section 8.2. In addition, large collision angles required widely separated beams (up to 5mm) on the focusing lens (lens diameter ~12mm). This required an additional translation stage for the focusing lens to provide equal alignment for both beams.

124
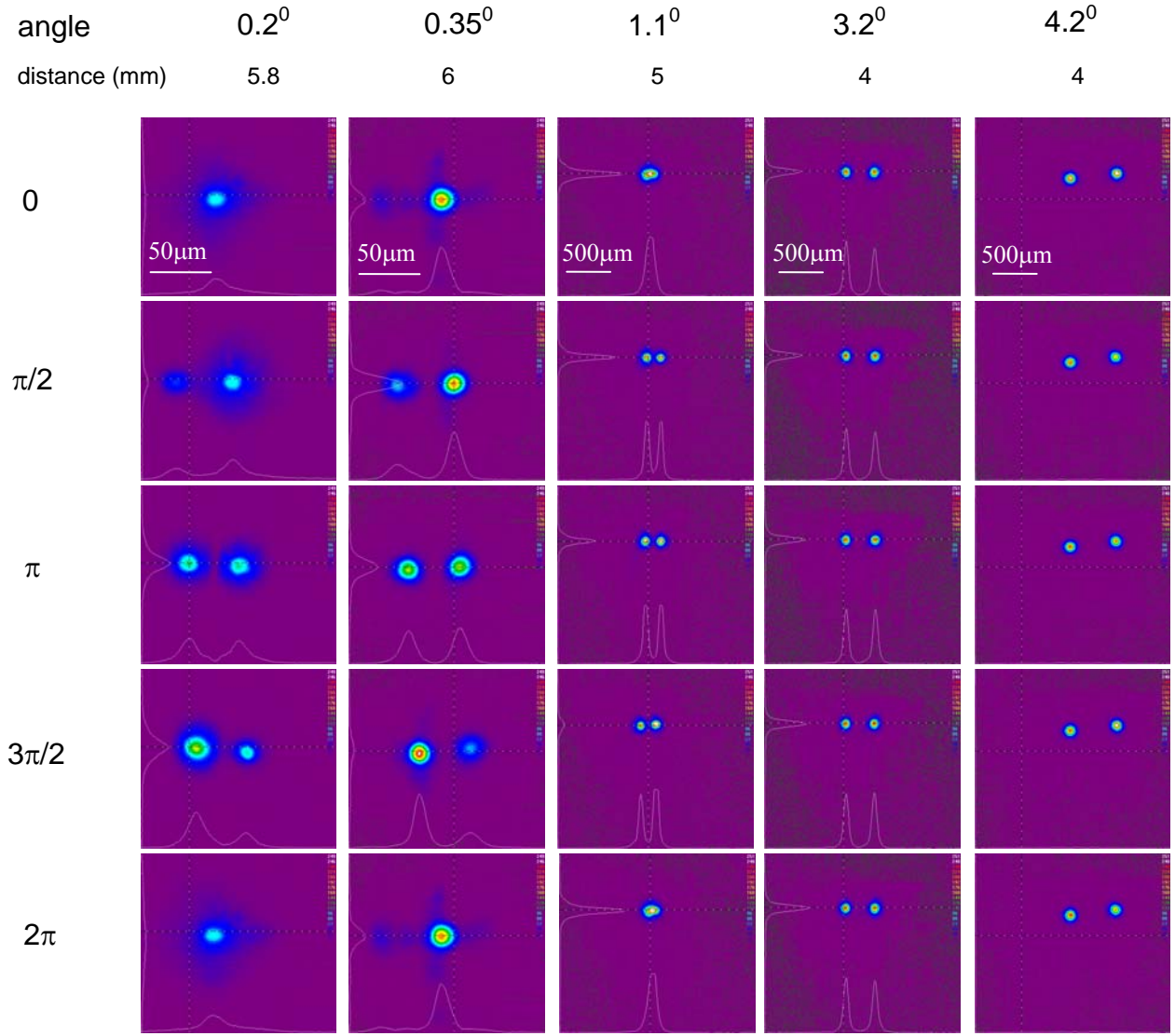
Figure 8.13: Collage of output patterns showing the differences between the collision processes that occur at different collision angles. The phase difference is indicated with the numbers on the left side. The term angle is used for the collision angle and it is given in degrees. The collision point is designated as distance and given in mm.

A set of collision experiments at several different collision angles was performed in the 1 cm long PPKTP sample under similar conditions to those in sections 8.2 and 8.3 experiments. The

sample temperature was kept at 27^0C (~3.5π), and in order to operate with positive phase mismatch and to generate solitons within short propagation distance in the crystal, the input beam energies were kept around 1.4μJ which is slightly lower than two times the single soliton threshold at the given phase mismatch. The angle was varied from ~0.2-5^0. As mentioned above, in order to perform the measurements for the different configurations, the imaging system was modified and therefore the experimentally measured soliton patterns were observed with different magnifications (~13 times smaller) at the output.

The measurements corresponding to five different collision angles (0.2, 0.35 1.1, 3.2 and 4.2 degrees) are shown in Figure 8.13. The numbers on the left side indicate the relative phase difference between the initially launched beams. In the figure the results for only a few selected phase differences are depicted. Full size scans for the 0.2^0 and 0.35^0 angles show similar features to Figure 8.6. As seen from the above figure the output pattern changes dramatically from small to large collision angles. The fusion and the inter-soliton energy transfer processes are clearly visible at small angles. As the angle increases to 1.1^0, the phase dependence decreases significantly. At 0^0 and 2π relative phase the two beams tend to attract, and as seen from the figure they collapse towards each other. The resulting beam is elongated and due to the "poor" picture resolution (imaging system) it is not clear if the beams only attract or they already fused. Typically at small relative angles the solitons colliding around 4-6mm of propagation at the 0^0 phase difference fuse very efficiently, generating a well shaped final soliton. However the process at an angle of 1.1^0 and at 0^0 phase appears to be different, indicating that perhaps the solitons do not fuse and the pattern observed is influenced by the resolution of the imaging

system. At other phase differences the solitons go through the energy exchange processes but their efficiency is significantly smaller than for the small collision angle case. While the weaker soliton carries around 25% of the total energy for the 0.35^0 case at the $\pi/2$ relative phase, it contains almost 45% of the total energy for the 1.1^0 case.
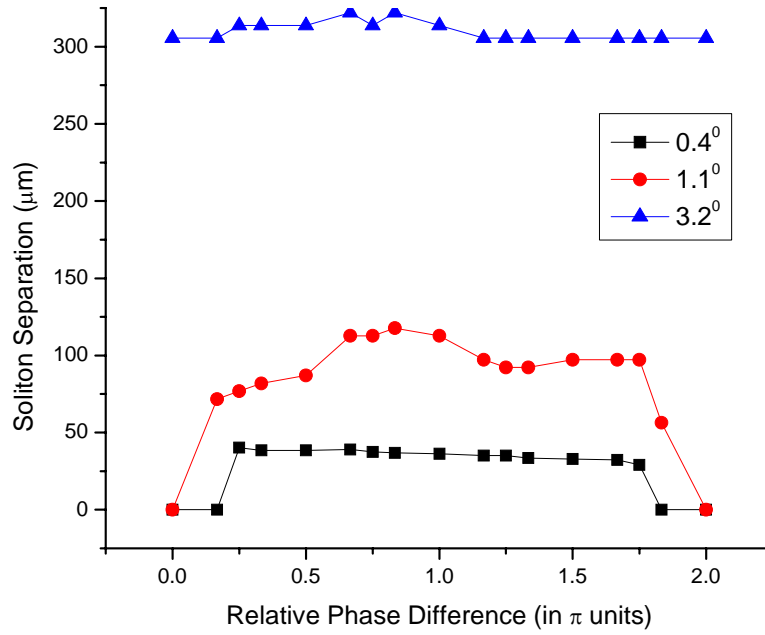
Figure 8.14: Dependence of the output soliton separation on relative phase difference between the propagating solitons measured at various collision angles. $\Delta kL = 3.5\pi$.

At the 3.2^0 and 4.2^0 collision angles, the propagating solitons essentially pass through each other, independent of the relative phase. The small changes in the relative solitons' intensities (fluctuations below 7%) observed in the output pattern are rather stochastic and do not reflect any significant interactions.

A summary of dependence of the output soliton separation on the collision angle is shown in Figure 8.14. Three characteristic curves are shown. For the 0.35^0 collision angle curve, essentially small collision angle behavior, as expected, is observed. Fusion occurs in the region around 0^0 relative phase and repulsion in a wide range around π phase difference. The soliton collisions at large angles 1.1^0 and 3.2^0 show very different behavior. For the 1.1^0 case there is still a significant drop in the soliton separation at 0^0 relative phase, indicating that the interaction processes still influence the output solitons. The soliton separation achieves approximately a constant value ($\sim100\mu m$) in the very large region of the relative phase. The asymmetric shape is believed to be associated with the data processing procedure that is limited by the imaging system magnification and resolution. For the 3.2^0 configuration the interaction processes have negligible influence on the colliding solitons due to the short interaction distance. The curve is featureless with only small stochastic oscillations around approximately constant $320\mu m$ soliton separation.

In conclusion to this chapter, a very extensive experimental investigation on quadratic soliton collisions was performed in a PPKTP crystal. The collision processes were investigated for various phase mismatches, collision angles and collision points. In addition, the relationship between the collision processes and the relative phase between the solitons was investigated. The carefully designed soliton collision experimental setup provided detailed information on the influence of the relative phase. In order to characterize the collision processes the output beam distributions at the sample's exit surface were monitored. The recorded patterns and the data extracted from them indicated a weakening of the interaction processes with increase in the

phase mismatch. In addition, at larger collision angles, the interaction efficiency decreased due to reduced interaction length and finally vanished at around 3^0 angles, as expected.

CHAPTER NINE: SUMMARY AND CONCLUSION

This Dissertation dealt with detailed investigations of quadratic soliton interactions. In the world of spatial solitons the interaction processes are one of the most intriguing effects, revealing in their full spectrum of effects the special nature of spatial solitons. The work was concentrated around the experimental observations of the quadratic soliton effects and phenomena in KN and periodically poled KTP (PPKTP). The corresponding numerical simulations supported well the experimental observations and measurements performed. Four different topics were covered within the manifold of quadratic soliton interactions: multi-soliton generation and related processes, soliton self-reflection and interactions with a specially engineered quadratically nonlinear interface, two soliton beam interactions and collisions in a birefringent medium and soliton collisions in PPKTP. In fact, prior to this research work, observations of quadratic soliton interactions and collisions were reported for only a few special geometries.

The experimental observation of multi-soliton generation, discussed in Chapter 5 of this Dissertation, was reported for the first time in quadratic nonlinear systems. It followed and utilized single soliton threshold measurements performed on a 1cm long KN sample in vicinity of NCPM. The multiple solitons were generated from a nearly cylindrically symmetric input beam at high intensities, exceeding several times the single soliton threshold. Up to five soliton-

like beams were observed at the sample's output facet. This experimental observation inspired a detail theoretical investigation of the parametric soliton processes. In the explored case of the KN multi-solitons, the laser beam noise played an important role in generating the output soliton distributions which changed on a shot-to-shot basis. The numerical simulations showed good qualitative agreement with the experimentally observed multi-soliton features.

In the chapter 6 on soliton self-reflection, intensity dependent interactions with a specially engineered nonlinear interface were reported. Launched at almost grazing angles of 0.5^0, a low intensity diffracting beam passed through a dislocated QPM interface while a high intensity (soliton) beam ($\sim 6 GW/cm^2$) was efficiently reflected from the interface achieving around a 60μm lateral shift relative to its transmission position. The interface influences parametric processes and thus disturbs an incident propagating soliton and eventually leads to the soliton reflection. Incomplete reflection efficiencies occurred as a consequence of the pulsed nature of the incident laser beams. In fact, there is a $3 GW/cm^2$ intensity window where both transmitted and reflected beams were observed simultaneously. This feature is in very good agreement with the numerically generated output patterns. An abrupt transmission-reflection change could be accessible with a CW input or of if the pulses were initially square shaped in time. Additional measurements in which the incident beam intercepted the boundary at various propagation distances after entering the sample were performed. They proved that self-reflection only occurs after the beam has evolved into a soliton for the standard conditions in which only the fundamental component of the soliton is launched into the sample. In fact, if a beam hits the interface in its early stages of propagation, the soliton is not yet formed and for all input beam intensities only transmission occurs. The experiments performed demonstrated the basic concept

131

and identified the potential of QPM engineered structures for soliton routing and manipulation.

Experimental measurements on two beam interaction processes in NCPM potassium niobate were reported for two configurations in Chapter 7. The impact of the phase difference between the solitons on the collisions was investigated with a precision far superior to that in previously reported measurements. For nearly co-propagating solitons colliding in a plane, fusion at 0^0 relative phase and repulsion at π phase difference occurred, in excellent agreement with theory. For other relative phases, energy transfer processes were observed. For a non-planar configuration with the solitons colliding at 0.9^0 angle, spiraling about a common axis of up to 30 degrees was measured. This effect resulted from the non-planar character of the collision geometry and indicated conservation of angular momentum associated with the common axis. Furthermore, an additional soliton was generated in the two soliton collision process. In fact, the additional soliton was centered between the outer solitons at 0^0 relative phase and shifted with increasing phase difference towards one of the outer solitons, finally merging with it in vicinity of π relative phase. At π a two soliton output was observed and the solitons showed an increased spiraling rate. The phase scan indicated the existence of a large range of relative input phases where three solitons occur. This feature could be useful for ultrafast all-optical switching. The ratio of the second harmonic to the fundamental components of the output solitons underwent only small energy changes (around 10%) with relative phase.

Another set of soliton collision experiments was performed in NCPM PPKTP and was discussed in Chapter 8. Because of the stability of the laser source which was used in the experiment, it proved possible to investigate the details of the collision processes for the first

132

time. The output intensity patterns were explored for solitons colliding at different distances from the input crystal facet, showing that the collisions require a certain stage of soliton formation (propagation distance) before the collisions exhibited soliton characteristics. If collided in early stages of beam propagation, the solitons are not well formed and the resultant parametric processes are strongly affected by the effects of linear interference which eventually completely disabled soliton formation. Influence of the phase mismatch on the collisions was investigated at a 0.4^0 collision angle. As expected, the soliton interaction strength decreased with increasing phase mismatch. This was most evident in the measurements of output soliton separation at π phase difference. Observed was a minimum in the soliton separation at the phase matching. The range of relative input phases for which fusion occurs decreased with increasing phase mismatch as well. In addition, the dependence on collision angle was investigated. Found experimentally was that the fusion phenomena occurred only for angles smaller than 1.2^0. The energy transfer processes, clearly present at a 1.1^0 collision angle, gradually diminish with increasing collision angle and almost completely vanish at 3.2^0.

The research performed on quadratic spatial solitons and their interactions was an extensive investigation that covered the basic concepts and yielded an important set of information on quadratic nonlinear systems. Most of the cases reported discussed first time observations of phenomena and, while some of the results have already influenced the fields of soliton science and nonlinear optics, others are believed to have potential to do so in the future. The collision experiments performed gave a deep insight into soliton collision phenomena in quadratically nonlinear materials and should prove invaluable in future experiments in quadratic array systems. Further improvements and innovations in QPM fabrication technology are expected to provide

133

new capabilities for engineering of some more exotic schemes that could eventually lead to new soliton guiding and routing processes in specially engineered structures.

Overall, the author believes that the work reported in this Dissertation extends the horizons of the spatial soliton field and is an extensive and important contribution to the soliton community.

LIST OF REFERENCES

Chapter 1:

1. Barthelemy, S. Maneuf and C. Froehly, Opt. Comm. **55**, 210 (1985).

2. S. Maneuf and F. Reynaud, Opt. Comm. **66**, 325 (1988).

3. J. U. Kang, G. I. Stegeman, J. S. Aitchison and N. Akhmediev, Phys. Rev. Lett. **76**, 3699 (1996).

4. J. S. Aitchison, A. M. Weiner, Y. Silberberg, M. K. Oliver, J. L. Jackel, D. E. Leaird, E. M. Vogel and P. W. Smith, Opt. Lett. **15**, 471 (1990).

5. J. S. Aitchison, D. C. Hutchings, J. U. Kang, G. I. Stegeman, E. Ostrovskaya and N. Akhmediev, J. Opt. Soc. Am. B **14**, 3032 (1997).

6. W. Torruellas, B. Lawrence and G. I. Stegeman, Electr. Lett. **32**, 2092 (1996).

7. V. Tikhonenko, J. Christou, B. Luther-Davis, Phys, Rev. Lett. **76**, 2698 (1996).

8. G. Duree, J. L. Shultz, G. Salamo, M. Segev, A. Yariv, B. Crosignani, P. DiPorto, E. Sharp and R. R. Neurganaonkar, Phys. Rev. Lett. **76**, 2698 (1996).

9. M. Taya, M. Bashaw, M. M. Fejer, M. Segev and G. C. Valley, Phys. Rev. A **52**, 3095 (1995).

10. M. D. Iturbe-Castillo, P. A. Marquez-Aguilar, J. J. Sanchez-Mondragon, S. Stepanov and V.

Vysloukh, Appl. Phys. Lett. **64**, 408 (1994).

11. W.E. Torruellas, Z. Wang, D.J. Hagan, E.W. van Stryland, G.I. Stegeman, L. Torner and C.R. Menyuk, "Observation of Two-Dimensional Spatial Solitary Waves in a Quadratic Medium", Phys. Rev. Lett. **74**, 5036 (1995).

12. R. Schiek, Y. Baek and G. I. Stegeman, "One-dimensional spatial solitary waves due to cascaded second-order nonlinearities in planar waveguides", Phys. Rev. E, **53**, 1138 (1996)

13. E. S. Barrekette, G. W. Stroke, Y, E, Nesterikihin and W. E. Kock, "Optical information processing", vol. 2, Plenum Press, New York, London, p. 452 (1978).

14. P.A. Franken, A.E. Hill, C.W. Peters and G. Weinreich, "Generation of Optical Harmonics", Phys. Rev. Lett. **7**, 118 (1961).

15. J.A. Armstrong, N. Bloembergen, J. Ducuing and P.S. Pershan, "Interaction between light waves in a dielectric ", Phys. Rev. **127**, 1918 (1962)

16. R. Y. Chiao, E. Garmire and C. H. Townes, Phys. Rev. Lett. **13**, 479 (1964).

17. V. E. Zakharov, Sov. Phys. JETP **26**, 994 (1968).

18. A. Hasegawa and F. Tappert, Appl. Phys. Lett. **23**, 142 (1973).

19. J. E. Bjorkholm and A. Ashkin, Phys Rev. Lett. **32**, 129 (1974).

20. Sergey Polyakov, Roman Malendevich, Ladislav Jankovic, George Stegeman, Christian Bosshard and Peter Gunter, "Effects of Anisotropic Diffraction on Quadratic Multi Soliton Excitation in Non-critically Phase-matched Crystals", Opt. Lett., **27,** 1049 (2002).

21. Silvia Carrasco, Sergey Polyakov, Hongki Kim, Ladislav Jankovic, George I. Stegeman, Juan P. Torres, Lluis Torner, Mordechai Katz, "Observation of multiple soliton generation mediated by amplification of asymmetries", Phys. Rev. E, **67**, 046616 (2003).

22. Sergey Polyakov, Ladislav Jankovic, Hongki Kim, George Stegeman, Silvia Carrasco, Lluis Torner and Mordechai Katz, "Properties of Quadratic Multi-Soliton Generation Near Phase-Match in Periodically Poled Potassium Titanyl Phosphate", Optics Express, **11**, 1328 (2003).

23. Sergey Polyakov, Hongki Kim, Ladislav Jankovic, George Stegeman and Mordechai Katz, "Weak Beam Control of Multi-Quadratic-Soliton-Generation", Opt. Lett., **28**, 1451 (2003).

24. P. W. Smith and W. J. Tomlinson, "Experimental studies at a nonlinear interface", IEEE J. Quant. Electron., **QE-20**, 30 (1984)

25. A. E. Kaplan, "Hysteresis reflection and refraction by a nonlinear boundary – a new class of effects in nonlinear optics", JETP Lett., **24**, 114 (1977) [Pis'ma Zh. Eksp. Tero. Fiz., **24**, 132 (1976)]

26. Y. Baek, R. Schiek and G.I. Stegeman, G. Baumann and W. Sohler, "Interactions between one-dimensional quadratic solitons", Opt.Lett., **22**, 1550 (1997).

27. B. Constantini, C. De Angelis, A. Barthelemy, B. Bourliaguet and V. Kermene, "Collisions between type II two-dimensional quadratic solitons", Opt. Lett., **23**, 424 (1998).

28. C. Simos, V. Couderc and A. Barthelemy, "Experimental observation of phase-controlled three-dimensional interactions between two quadratic spatial solitons: scattering, fusion and spiraling", Techn. Digest of 2002 Nonlinear Guided Waves and Their Applications, (Opt. Soc. Am., Washington, 2002), NLWB2.

29. W. Krolikowski and S. A. Holstrom, "Fusion and birth of spatial solitons upon collision", Opt. Lett., **22**, 369 (1997).

Chapter 2:

1. P.A. Franken, A.E. Hill, C.W. Peters and G. Weinreich, "Generation of Optical Harmonics", Phys. Rev. Lett. **7**, 118 (1961).

2. J.A. Armstrong, N. Bloembergen, J. Ducuing and P.S. Pershan, "Interaction between light waves in a dielectric ", Phys. Rev. **127**, 1918 (1962)

3. R. Boyd, *Nonlinear Optics*, New York, Academic Press, 1992.

4. Y.R. Shen, *The Principles of Nonlinear Optics*, New York, Wiley, 1984.

5. M.M. Fejer, G.A. Magel, D.H. Jundt and R.L. Byer, J. Quantum Electron. vol 28, 2631 (1992)

6. W.E. Torruellas, Z. Wang, D.J. Hagan, E.W. van Stryland, G.I. Stegeman, L. Torner and C.R. Menyuk, "Observation of Two-Dimensional Spatial Solitary Waves in a Quadratic Medium", Phys. Rev. Lett. **74**, 5036 (1995).

7. Roman Malendevich, Ladislav Jankovic, Sergey Polyakov, Russell Fuerst, George Stegeman, Christian Bosshard and Peter Gunter, "Two-dimensional type I quadratic spatial solitons in KNbO 3 near noncritical phase matching", Opt. Lett. **27**, 631 (2002).

Chapter 3:

1. William T. Silfvast, "Laser Fundamentals", Cambridge University Press (1996).

2. R. Boyd, *Nonlinear Optics*, New York, Academic Press, 1992.

3. Y.R. Shen, *The Principles of Nonlinear Optics*, New York, Wiley, 1984.

Chapter 4:

1. H. Fang, R. Malendevich, R. Schiek and G.I. Stegeman, "Spatial modulational instability in one-dimensional lithium niobate slab waveguides", Opt. Lett. **25**, 1786 (2000).

2. R. Schiek, H. Fang, R. Malendevich and G.I. Stegeman, "Measurement of Modulational Instability Gain of Second-Order Nonlinear Optical Eigenmodes in a One-Dimensional System", Phys. Rev. Lett., **86**, 4528 (2001).

3. Roman Malendevich, Ladislav Jankovic, George Stegeman and J. Stewart Aitchison, "Spatial modulation instability in a Kerr slab waveguide", Opt. Lett. **26**, 1879 (2001).

4. Y. Karamzin and A. Sukhorukov, Sov. Phys. JETP **41**, 414 (1976); Zh. Eksp. Teor Fiz. **68**, 834 (1975).

5. W.E. Torruellas, Z. Wang, D.J. Hagan, E.W. van Stryland, G.I. Stegeman, L. Torner and C.R. Menyuk, "Observation of Two-Dimensional Spatial Solitary Waves in a Quadratic Medium", Phys. Rev. Lett. **74**, 5036 (1995).

6. K. Hayata and M. Koshiba, Phys. Rev. Lett. **71**, 3275 (1993).

7. William H. Press, Brian P. Flannery, Saul A. Teukolsky and William T. Vetterling, *Numerical recopies in C*, Cambridge University Press, page 710 (2001).

8. Kenji Kawano and Tsutomu Kitoh, *Introduction to optical waveguide analysis*, New York, Wiley-Interscience Publication, page 165 and 233, 2001.

9. Gaetano Assanto and George I. Stegeman, "Simple physics of quadratic solitons", Opt. Express, **10**, 388 (2002).

10. P. Di Trapani, G. Valiulis W. Chinaglia and A. Andreoni, " Two-Dimensional Spatial Solitary Waves from Traveling-Wave Parametric Amplification of the Quantum Noise",

Phys. Rev. Lett. **80**, 265 (1998).

Chapter 5:

1. Biaggio et al., "Refractive indices orthorhombic $KNbO_3$. II. Phase-matching configuration for nonlinear-optical interactions", JOSA B **9**, 507 (1992)

2. V.G. Dmitriev, G.G. Gourzadayan and D.N. Nikogosyan, *Handbook of Nonlinear Optical Crystals*, Springer-Verlag, Berlin, 1997.

3. A.D. Ludlow, H.M. Nelson and S.D. Bergeson, "Two-photon absorption in potassium niobate", JOSA B, **18**, 1813 (2001)

4. B. Zysset et al., "Refractive indices of orthorhombic $KNbO_3$. I. Dispersion and temperature dependence", JOSA B, **9**, 380 (1992)

5. R. Schiek, Y. Baek and G. I. Stegeman, "One-dimensional spatial solitary waves due to cascaded second-order nonlinearities in planar waveguides", Phys. Rev. E, **53**, 1138 (1996)

6. Roman Malendevich, Ladislav Jankovic, Sergey Polyakov, Russell Fuerst, George Stegeman, Christian Bosshard and Peter Gunter, "Two-dimensional type I quadratic spatial solitons in KNbO 3 near noncritical phase matching", Opt. Lett. **27**, 631 (2002).

7. Sergey Polyakov, Roman Malendevich, Ladislav Jankovic, George Stegeman, Christian Bosshard and Peter Gunter, "Effects of Anisotropic Diffraction on Quadratic Multi Soliton Excitation in Non-critically Phase-matched Crystals", Opt. Lett., **27,** 1049 (2002).

8. Silvia Carrasco, Sergey Polyakov, Hongki Kim, Ladislav Jankovic, George I. Stegeman, Juan P. Torres, Lluis Torner, Mordechai Katz, "Observation of multiple soliton generation mediated by amplification of asymmetries", Phys. Rev. E, **67**, 046616 (2003).

9. Sergey Polyakov, Ladislav Jankovic, Hongki Kim, George Stegeman, Silvia Carrasco, Lluis Torner and Mordechai Katz, "Properties of Quadratic Multi-Soliton Generation Near Phase-Match in Periodically Poled Potassium Titanyl Phosphate", Optics Express, **11**, 1328 (2003).

10. Sergey Polyakov, Hongki Kim, Ladislav Jankovic, George Stegeman and Mordechai Katz, "Weak Beam Control of Multi-Quadratic-Soliton-Generation", Opt. Lett., **28**, 1451 (2003).

11. L. Jankovic, H. Kim, S. Polyakov, G.I. Stegeman, C. Bosshard and P. Gunter, "Interactions of Quadratic Spatial Solitons in Noncritically Phase-Matched $KNbO_3$", Laser Physics, **14**, 264 (2004).

12. W.E. Torruellas, Z. Wang, D.J. Hagan, E.W. van Stryland, G.I. Stegeman, L. Torner and C.R. Menyuk, "Observation of Two-Dimensional Spatial Solitary Waves in a Quadratic Medium", Phys. Rev. Lett. **74**, 5036 (1995).

13. S. Minardi, J. Yu, G. Blasi, A. Varanavicius, G. Valiulis, A. Berzanskis, A. Piskarskas, P. Di Trapani, "Red solitons: Evidence of spatiotemporal instability in chi((2)) spatial soliton dynamics", Phys. Rev. Lett., **91**, No. 123901 (2003).

Chapter 6:

1. H. Fang, R. Malendevich, R. Schiek and G.I. Stegeman, "Spatial modulational instability in one-dimensional lithium niobate slab waveguides", Opt. Lett. **25**, 1786 (2000).

2. R. Schiek, H. Fang, R. Malendevich and G.I. Stegeman, "Measurement of Modulational Instability Gain of Second-Order Nonlinear Optical Eigenmodes in a One-Dimensional System", Phys. Rev. Lett., **86**, 4528 (2001).

3. Roman Malendevich, Ladislav Jankovic, George Stegeman and J. Stewart Aitchison,

"Spatial modulation instability in a Kerr slab waveguide", Opt. Lett. **26**, 1879 (2001).

4. Hongki Kim, Ladislav Jankovic, George Stegeman, Silvia Carrasco, Lluis Torner, David Eger, Mordechai Katz, "Quadratic spatial solitons in periodically poled KTiOPO$_4$", Opt. Lett., **28**, 640 (2003).

5. P. W. Smith and W. J. Tomlinson, "Experimental studies at a nonlinear interface", IEEE J. Quant. Electron., **QE-20**, 30 (1984)

6. A. E. Kaplan, "Hysteresis reflection and refraction by a nonlinear boundary – a new class of effects in nonlinear optics", JETP Lett., **24**, 114 (1977) [Pis'ma Zh. Eksp. Tero. Fiz., **24**, 132 (1976)].

7. C. B. Clausen and L. Torner, "Spatial switching of quadratic solitons in engineered quasi-phase-matched structures", Opt. Lett., **24**, 7 (1999)

Chapter 7:

1. G. I. Stegeman and M. Segev, "Optical spatial solitons and their interactions: Universality and diversity" Science, **286**,1518 (1999).

2. M. Segev and G. Stegeman, "Self-trapping of optical beams: Spatial solitons", Phys. Today **51**, 42 (1998).

3. J. S. Aitchison, A. M. Weiner, Y. Silberberg, D. E. Leaird, M. K. Oliver, J. L. Jackel and P. W. E. Smith, "Experimental observation of spatial soliton interactions"Opt. Lett., **16**, 15 (1991).

4. M. Shalaby, F. Reynaud and A. Barthelemy, "Experimental observation of spatial soliton interactions with a Pi/2 relative phase difference"Opt. Lett., **17**, 778 (1992).

5. M.F. Shih and M. Segev, "Incoherent collisions between two-dimensional bright steady-state photorefractive spatial screening solitons"Opt. Lett., **21**, 1538 (1996).

6. M. Shih, Z. Chen, T. H. Coskun and D. N. Christodoulides, "Incoherent collisions between one-dimensional steady-state photorefractive screening solitons", Appl. Phys. Lett., **69**, 4151 (1996).

7. Gaetano Assanto and George I. Stegeman, "Simple physics of quadratic solitons", Opt. Express, **10**, 388 (2002).

8. C. Simos, V. Couderc and A. Barthelemy, "Experimental observation of phase-controlled three-dimensional interactions between two quadratic spatial solitons: scattering, fusion and spiraling", Techn. Digest of 2002 Nonlinear Guided Waves and Their Applications, (Opt. Soc. Am., Washington, 2002), NLWB2.

9. Christos Simos, Vincent Couderc, Alain Barthelemy and Alexander V. Buryak, J. Opt. Soc. Am. B **20**, 2133 (2003).

10. W. Krolikowski and S. A. Holstrom, "Fusion and birth of spatial solitons upon collision", Opt. Lett., **22**, 369 (1997).

11. G. I. Stegeman, L. Jankovic, H. Kim, S. Polyakov, S. Carrasco, L. Torner, C. Bosshard, P. Gunter, M. Katz, D. Eger, "Generation of, and interactions between, quadratic spatial solitons in non-critically-phase-matched crystals ", J. Nonlinear Opt. Phys. **12**, 447 (2003).

Chapter 8:

1. Roman Malendevich, Ladislav Jankovic, Sergey Polyakov, Russell Fuerst, George Stegeman, Christian Bosshard and Peter Gunter, Opt. Lett. **27**, 631 (2002).

2. Hongki Kim, Ladislav Jankovic, George Stegeman, Silvia Carrasco, Lluis Torner, David Eger, Mordechai Katz, "Quadratic spatial solitons in periodically poled KTiOPO$_4$", Opt. Lett., **28**, 640 (2003).

3. A.D. Ludlow, H.M. Nelson and S.D. Bergeson, "Two-photon absorption in potassium niobate", JOSA B, **18**, 1813 (2001)

4. G. I. Stegeman, D. J. Hagan and L. Torner, Opt. Quantum Electron. **28**, 1691 (1996).